

**Viscosity and Droplet Dissolution Quantification using Microfluidic Devices**

A Dissertation

Presented to

Graduate School of Sciences and Engineering in  
Partial Fulfillment of the Requirements for the Degree of

Doctor of Philosophy

In

Biomedical Sciences and Engineering

By

Adil Mustafa

Koç University

December, 2018



**COPYRIGHT © 2018 BY ADIL MUSTAFA**  
**Viscosity and Droplet Dissolution Quantification using Microfluidic Devices**

This is to certify that I have examined this copy of a doctoral dissertation by

**Adil Mustafa**

and have found that it is complete and satisfactory in all respects,

and that any and all revisions required by the final

examining committee have been made.

Approved by:

Dr. Alper Kiraz, Advisor  
Department of Physics  
*Koç University*

Dr. Ahmet Can Erten  
Department of Electronics Engineering  
*Istanbul technical University*

Dr. Özlem Yalçın  
Department of Biomedical Engineering  
*Koç University*

Dr. Serap Aksu  
Department of Physics  
*Koç University*

Dr. Kenan Çiçek  
Department of Electronics Engineering  
*Iğdir University*

Date Approved: December 26th, 2018

Koç University

Graduate School of Sciences and Engineering

This is to certify that I have examined this copy of a PhD thesis by

Adil Mustafa

and have found that it is complete and satisfactory in all respects, and that any and all  
revisions required by the final examining committee have been made.

Committee Members:



Dr. Alper Kiraz, (Advisor) Department of Physics, Koç University



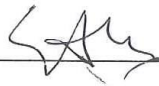
Dr. Özlem Yalçın Department of Biomedical Engineering, Koç University



Dr. Kenan Çiçek Department of Electronics Engineering, Iğdır University



Dr. Ahmet Can Erten Department of Electronics Engineering, Istanbul technical  
University



Dr. Serap Aksu Department of Physics, Koç University

*To my parents*



## ACKNOWLEDGEMENTS

I would like to express my deepest gratitude to my advisor Professor Alper Kiraz for giving me the opportunity to work with him, his guidance, and the experiences I earned throughout my studies during the past four and a half years. I admire him for being always enthusiastic, and for his result-oriented approach towards solving problems.

I would also like to express my gratitude to my co-supervisor Professor Özlem Yalcin for her continuous support and guidance during my PhD. I would like to thank Professors Ahmet Can Erten, Serap Aksu and Kenan Çiçek for being part of thesis committee. I thank Professor Erten for sharing his expertise in microfluidic device design and his guidance regarding CFD simulations.

I would like to thank Soheila Kharratiankhameneh for her support throughout my PhD studies and her encouraging attitude that instated in me enthusiasm to work hard.

Last but not least all the former and current members of Kiraz lab whose professionalism led to an efficient and productive research environment.

## **TABLE OF CONTENTS**

<b>ACKNOWLEDGEMENTS</b>	<b>iv</b>
<b>LIST OF TABLES</b>	<b>ix</b>
<b>LIST OF FIGURES</b>	<b>x</b>
<b>LIST OF SYMBOLS AND ABBREVIATIONS</b>	<b>xvii</b>
<b>ABSTRACT</b>	<b>1.</b>
<b>Chapter 1</b>	<b>1</b>
<b>Introduction</b>	<b>1</b>
<b>1.1 Microfluidics a general concept</b>	<b>1</b>
<b>1.2 Micro Scale Fluid Flow</b>	<b>1</b>
<b>1.3 Literature Review Microfluidic Viscometers</b>	<b>3</b>
<b>1.4 Literature Review Hydrodynamic Trapping and Dissolution</b>	<b>4</b>
<b>1.5 Organization of Thesis</b>	<b>5</b>
<b>Chapter 2.</b>	<b>7</b>
<b>Viscometer Design and Fabrication</b>	<b>7</b>
<b>2.1 Introduction</b>	<b>7</b>
<b>2.2 Microfluidic Design and Fabrication Al Mold</b>	<b>7</b>
<b>2.3 Microfluidic Design and Fabrication Si Mold</b>	<b>10</b>

<b>Chapter 3.</b>	<b>14</b>
<b>Micropillar based viscometer</b>	<b>14</b>
<b>3.1 Introduction</b>	<b>14</b>
<b>3.2 Sample fluid preparation</b>	<b>16</b>
<b>3.3 Experimental setup</b>	<b>16</b>
<b>3.4 Experimental methods</b>	<b>17</b>
<b>3.5 Image Analysis</b>	<b>18</b>
<b>3.6 Viscosity Measurements Newtonian Fluids</b>	<b>19</b>
<b>3.7 Viscosity Measurements non-Newtonian Fluids</b>	<b>31</b>
<b>3.8 Precision of Microfluidic Viscometer</b>	<b>36</b>
 <b>Chapter 4.</b>	 <b>38</b>
<b>4.1 Introduction</b>	<b>38</b>
<b>4.2 Calibrating Microfabricated devices</b>	<b>39</b>
<b>4.3 Blood coagulation studies</b>	<b>42</b>
 <b>Chapter 5.</b>	 <b>48</b>
<b>Computational Fluid dynamic studies</b>	<b>48</b>

<b>5.1 Introduction</b>	<b>48</b>
<b>5.2 Simulation design parameters</b>	<b>48</b>
<b>5.3 Viscometer device with straight micropillar array</b>	<b>49</b>
<b>5.4 Viscometer device with alternating micropillar array</b>	<b>52</b>
<b>5.5 Comparison simulation studies vs experimental data</b>	<b>56</b>
<b>Chapter 6.</b>	<b>58</b>
<b>Dissolution of microdroplets</b>	<b>58</b>
<b>6.1 Introduction</b>	<b>58</b>
<b>6.2 Mathematical Modelling</b>	<b>61</b>
<b>6.3 Epstein-Plesset (EP) Model</b>	<b>61</b>
<b>6.4 Zhang-Yang-Mao (ZYM) Model</b>	<b>62</b>
<b>Chapter 7.</b>	<b>65</b>
<b>Hydrodynamic Chip Fabrication and Experimental Setup</b>	<b>65</b>
<b>7.1 Introduction</b>	<b>65</b>
<b>7.2 Device Fabrication</b>	<b>66</b>
<b>7.3 Soft Lithography</b>	<b>69</b>
<b>7.4 Microdroplet Generation</b>	<b>70</b>



<b>7.5 Experimental Setup</b>	<b>71</b>
<b>Chapter 8.</b>	<b>74</b>
<b>Enhanced Dissolution of Liquid Micro Droplets</b>	<b>74</b>
<b>8.1 Introduction</b>	<b>74</b>
<b>8.2 Benzyl Benzoate 10mM Experiments</b>	<b>75</b>
<b>8.3 Benzyl Benzoate 10<math>\mu</math>M Experiments</b>	<b>79</b>
<b>8.4 Decanol 10 mM Experiments</b>	<b>82</b>
<b>APPENDIX A.</b>	<b>87</b>
<b>Matlab Code for micropillar tracking</b>	<b>87</b>
<b>REFERENCES</b>	<b>92</b>

## LIST OF TABLES

Table T1. Calculated Viscosity using 2 <sup>nd</sup> order polynomial equation	31
Table T2. Calculated Blood Viscosity using linear fitting equation	32

## LIST OF FIGURES

Fig 2.1 (a) Micromachined Aluminium Mold ( $D = 300\mu\text{m}$ , $H = 1500\mu\text{m}$ ). (b) PDMS microfluidic chip bonded on glass slide (1"×3").	<b>08</b>
Fig 2.2. Microfluidic Channel with $\mu$ pillar diameter of $300\mu\text{m}$ using Al mold.	<b>09</b>
Fig 2.3. Process flow Si wafer microfabrication.	<b>11</b>
Fig 2.4a. Microfluidic Channel with circular $\mu$ pillar diameter of $25\mu\text{m}$ using Si mold.	<b>12</b>
Fig 2.4b. Microfluidic Channel with square $\mu$ pillar diameter of $25\mu\text{m}$ using Si mold.	<b>12</b>
Fig 2.5. (a), (b), (c) and (d) SEM image circular of micropillar array.	<b>13</b>
Fig 3. Sketch of experimental setup. A microscope (Nikon Eclipse TS100 series) for imaging, a syringe pump (Harvard Apparatus) for infusing liquid, a computer and a CMOS camera (Point Grey Grasshopper3) for imaging and recording.	<b>17</b>
Fig. 3.2 (a), (b), (c) and (d) Pillar displacement with decreasing viscosity. It can be seen that cantilever displacement decreases from (a) – (d) as the viscosity of the fluid decreases with diameter of the black spots represent viscosity of fluid.	<b>18</b>
Fig. 3.3 Displacement Vs Time for a single $\mu$ Pillar depicting. Displacement increases with time and saturation region represents the maximum micropillar displacement.	<b>19</b>
Fig.3.4. Flow Rate Vs Displacement (2cP - 3cP) sensitivity experiments. A sensitivity of 0.5 cP is observed for our device.	<b>22</b>

Fig.3.5 Calibration using 1cP (DI water) Chip A, Chip B, Chip C and Chip D. chip D represents a non-functional chip. **23**

Fig.3.6. Flow Rate Vs Displacement (dynamic range) Chip A, B, C and D Flow rate (15ml/hr – 105ml/hr). Displacement increases linearly as the flow rate is increased. (No of Experiments N=3) for each chip at each flow rate. **24**

Fig.3.7 Viscosity Vs Displacement fixed flow rate (15ml/hr – 60ml/hr) Chip A, B, C and D with 2<sup>nd</sup> order polynomial fitting. Displacement increases linearly from (2cP – 25cP). A non-linear behavior is observed above 25cP. (No of Experiments N=3) for each chip at each flow rate. **25**

Fig.3.8 Viscosity Vs Displacement fixed flow rates (15ml/hr – 60ml/hr) for Chip A. A 2<sup>nd</sup> order polynomial equation ( $Y = \text{Intercept} + b_1x + b_2x^2$ ) is used to fit the data. **27**

Fig.3.9 Flow Rate Vs Displacement Decanol (11.91 cP). Flow rate range (15ml/hr – 60ml/hr). **28**

Fig.3.10 Viscosity Vs Displacement fixed flow rates (15ml/hr – 60ml/hr) for Chip B. A 2<sup>nd</sup> order polynomial equation ( $Y = \text{Intercept} + b_1x + b_2x^2$ ) is used to fit the data. **29**

Fig.3.11 Viscosity Vs Displacement fixed flow rates (15ml/hr – 60ml/hr) for Chip C. A 2<sup>nd</sup> order polynomial equation ( $Y = \text{Intercept} + b_1x + b_2x^2$ ) is used to fit the data. **30**

Fig.3.12 Flow Rate vs Displacement plots for whole blood sample Chip A, B and C in comparison with Viscosity vs Shear Rate using “Brookfield Programmable DV-II + viscometer”. The displacement is increasing as the flow rate is increased. **32**

Fig.3.13. Viscosity vs Displacement Glycerol/water (non-Newtonian) fluid plots between (5cP – 25cP) with linear fit for (30ml/hr - 90ml/hr). The slope equation  $y = a + bx$  is used to calculate the viscosity of blood by inserting the displacement  $y = 5.28 \mu\text{m}$  in the slope equation. **33**

Fig.3.14 Viscosity Vs Shear rate. Red scatter plot represents Brookfield commercial viscometer result with a minimum shear rate of  $187 \text{ s}^{-1}$  and Black scatter plot shows the microfluidic viscometer measured viscosity with a minimum shear rate of  $77 \text{ s}^{-1}$ . **36**

Fig.3.15 Viscosity Vs Shear rate. The average standard deviation (SD) is calculated for 3 experiments at each viscosity at four different flow rates (15ml/hr, 30ml/hr, 45ml/hr and 60ml/hr). **37**

Fig.4.1. flow rate vs Displacement Glycerol/water (Newtonian) fluid plots for (1cP – 5cP) for square shaped micropillars. **39**

Fig.4.2. flow rate vs Displacement Glycerol/water (Newtonian) fluid plots for (1cP – 5cP) for circular shaped micropillars. **40**

Fig.4.3. Circular micropillars total shear rate in channel  $350 \text{ S}^{-1}$  at 15ml/hr. **40**

Fig.4.4. Square micropillars total shear rate in channel  $350 \text{ S}^{-1}$  at 15ml/hr. **41**

Fig.4.5. Flow rate Vs Displacement 1cP circular chip vs square chip. **42**

Fig.4.6. Flow rate Vs Displacement 1cP circular chip vs square chip.	<b>42</b>
Fig. 4.7 (a) Infusion of blood into device (b) coagulation initiating (c) clots forming around micropillars (d) fully formed clot around micropillars.	<b>43</b>
Fig.4.8. Displacement vs Time plot for coagulation experiment depicting different stages of blood coagulation process.	<b>44</b>
Figures 4.9 (a) Blood infusion/withdraw in channel at 15ml/hr	<b>45</b>
Figures 4.9 (b) Coagulation/clot formation starts and is visible right side of the channel as blood is infused and withdraw.	<b>46</b>
Figures 4.9 (c) Homogeneous coagulation/clot formation throughout the channel.	<b>46</b>
Figures.4.9 (d) Clots fully formed around the micropillars and it was observed visually during the experiments.	<b>47</b>
Figures.4.10 Extem, Intem and Fibtem tests using microfabricated micropillar device.	<b>47</b>
Fig 5.1 Micropillars with fixed constraint boundary condition.	<b>49</b>
Fig 5.2 Microfluidic viscometer straight micropillar array with channel height ( $H = 1600 \mu\text{m}$ ) and width ( $W = 900 \mu\text{m}$ ).	<b>50</b>
Fig 5.3 Microfluidic viscometer with straight micropillar array pressure contour plot (flow rate = 15ml/hr).	<b>51</b>
Fig 5.4 Microfluidic viscometer straight micropillar array streamlines. The stream lines are denser near the side walls depicting that most of the fluid passes along the sidewalls.	<b>51</b>

Fig.5.5 Flow rate vs Displacement plot for microchannel with straight micropillar array. Viscosity range (5cP – 50cP and flow rate range (15ml/hr – 105ml/hr).	<b>52</b>
Fig 5.6. Alternating micropillar array viscometer device with channel height ( $H = 1600 \mu\text{m}$ ) and width ( $W = 900 \mu\text{m}$ ).	<b>53</b>
Fig.5.7. Microfluidic viscometer alternating micropillar array streamlines. The stream lines are evenly distributed along the side walls and through the center of the array depicting increased fluid interaction with micropillar structures.	<b>54</b>
Fig.5.8. Microfluidic viscometer with alternate channel micropillar array pressure contour plot (flow rate = 15ml/hr).	<b>55</b>
Fig.5.9. Microfluidic viscometer alternating micropillar array vs straight micropillar array. Flow rate range (15ml/hr – 105 ml/hr).	<b>56</b>
Fig 5.10 Microfluidic viscometer alternating micropillar array simulation vs experimental data. Flow rate range (15ml/hr – 105 ml/hr).	<b>57</b>
Fig. 6.1 Dissolution of oil microdroplet at different flow rates $T=210 \text{ s}$ and $T=1410 \text{ s}$ .	<b>61</b>
Fig.7.1 Graphical representation of creating condition ( $R1 = R2$ ) for efficient trapping of micro particles.	<b>65</b>
Fig.7.2 Graphical representation of stagnation point and particle trapped at stagnation point.	<b>66</b>
Fig.7.3 Fluidic channel height measured using a profiler ( $H = 35\mu\text{m}$ ).Fig.	<b>67</b>

7.4 (a) Microfluidic chip layout where inlets, outlets, pneumatic membrane valve and trapping region are indicated. (b) Image of a single microdroplet trapped at the junction of two intersecting microchannels using the hydrodynamic trap. Flow directions in the trapping region are indicated by arrows. **68**

Figure.7.5 Sketch of the experimental setup used for microdroplet hydrodynamic trapping experiments. **72**

Figure 8.1. Scatter plots showing dissolution of multiple BB microdroplets in DI water containing 10 mM AOT surfactant at flow rates (a)  $Q = 10 \mu\text{L/h}$ , (b)  $Q = 20 \mu\text{L/h}$ , and (c)  $Q = 50 \mu\text{L/h}$  along with EP and ZYM model predictions. Measurements from 4, 5, and 5 microdroplets are time-shifted to obtain the scatter plots in panels a, b, and c, respectively. (d) Dissolution curves showing the combined scatter plots at three different flow rates along with EP and ZYM model predictions. In panels a–d, solid red lines show the EP model predictions and dashed red lines show the ZYM model predictions assuming  $c_s = 45 \times 10^{-3} \text{ kg/m}^3$ . (e) Snapshot images recorded from an exemplary BB microdroplet while dissolving at a flow rate of  $Q = 50 \mu\text{L/h}$ . **76**

Figure 8.2: Péclet (a) and Sherwood (b) numbers calculated for data points shown in Figure 8.1, obtained with benzyl benzoate microdroplets in DI water containing 10 mM AOT surfactant. **77**

Figure 8.3. Scatter plots showing dissolution of multiple BB microdroplets in DI water containing 10  $\mu\text{M}$  AOT surfactant at flow rates (a)  $Q = 5 \mu\text{L/h}$ , (b)  $Q = 10 \mu\text{L/h}$ , and (c)  $Q = 15 \mu\text{L/h}$  along with EP and ZYM model predictions. Measurements from 5, 7, and 5



microdroplets are time-shifted to obtain the scatter plots in panels a, b, and c, respectively. (d) Dissolution curves showing the combined scatter plots at three different flow rates along with EP and ZYM model predictions. In panels a–d solid red lines show the EP model predictions and dashed red lines show the ZYM model predictions assuming  $c_s = 15 \times 10^{-3} \text{ kg/m}^3$ . Dashed black line in panel b shows the ZYM model prediction assuming  $c_s = 18 \times 10^{-3} \text{ kg/m}^3$ . (e) Snapshot images recorded from an exemplary BB microdroplet while at a flow rate of  $Q = 5 \text{ }\mu\text{L/h}$ . **80**

Figure 8.4: Péclet (a) and Sherwood (b) numbers calculated for data points shown in Figure 8.3, obtained with benzyl benzoate microdroplets in DI water containing  $10 \text{ }\mu\text{M}$  AOT surfactant. **81**

Figure 8.5. Scatter plots showing dissolution of multiple n-decanol microdroplets in DI water containing  $10 \text{ mM}$  AOT surfactant at flow rates (a)  $Q = 5 \text{ }\mu\text{L/h}$ , (b)  $Q = 10 \text{ }\mu\text{L/h}$ , and (c)  $Q = 15 \text{ }\mu\text{L/h}$  along with EP and ZYM model predictions. Measurements from 5, 9, and 4 microdroplets are times shifted to obtain the scatter plots in panels a, b, and c, respectively. (d) Dissolution curve showing the combined scatter plots at three different flow rates along with EP and ZYM model predictions. In panels a–d solid red lines show the EP model predictions and dashed red lines show the ZYM model predictions assuming  $c_s = 385 \times 10^{-3} \text{ kg/m}^3$ . (e) Snapshot images recorded from an exemplary n-decanol microdroplet while dissolving at a flow rate of  $Q = 10 \text{ }\mu\text{L/h}$ . **83**

Figure 8.6: Péclet (a) and Sherwood (b) numbers calculated for data points shown in Fig.8.5, obtained with n-decanol microdroplets in DI water containing  $10 \text{ mM}$  AOT surfactant. **84**

## LIST OF SYMBOLS AND ABBREVIATIONS

$\rho$	Fluid density
$\mu$	Fluid velocity vector
$\eta$	Dynamic viscosity
$f$	Body forces
Re	Reynolds number
$L_0$	Characteristic length of the micro channel
$U_0$	Flow velocity
Al	Aluminium
PDMS	Polydimethylsiloxane
cP	Centipoise
BB	Benzyl Benzoate
DEC	Decanol
CMC	Critical micelle concentration
Pé	Péclet number

Sh	Sherwood number
EP	Epstein-Plesset model
ZYM	Zhang-Yang-Mao model
$\beta$	Ratio of dynamic viscosity of droplet to the surrounding fluid
$A_{\text{drop}}$	Area of droplet
$C_s$	Saturation coefficient
$A_{\text{chan}}$	Area of channel
SEM	Scanning electron microscope
SD	Standard deviation

## ABSTRACT

In this dissertation we focused on two different liquid properties both of which have significant importance in number of industrial and medical processes. Two different experimental setups are discussed and employed. Viscometer device (soft cantilevers) fabricated out of polydimethylsiloxane are used. The measuring mechanism is based on recording and evaluating the response of these cantilevers under fluid at different flow rates. The micropillar (soft cantilevers) devices are made using a single step fabrication out of micromachined Aluminium mold. Viscosities with values up to 0.5cP are measured. A dynamic flow rate range of (15ml/hr – 105ml/hr) is also reported. The microfabricated viscometer devices are used to perform blood coagulation studies and it is reported that as the blood viscosity changes over time the response of the micropillars also varies.

In second part of thesis a novel noncontact technique based on hydrodynamic trapping is presented to study the dissolution of freely suspended liquid micro droplets into a second immiscible phase in a simple extensional creeping flow. Benzyl benzoate (BB) and n-decanol micro droplets are individually trapped at the stagnation point of a planar extensional flow, and dissolution of single micro droplets into an aqueous solution containing surfactant is characterized at different flow rates. The experimental dissolution curves are compared to two models: (i) the Epstein–Plesset (EP) model which considers only diffusive mass transfer, and (ii) the Zhang–Yang–Mao (ZYM) model which considers both diffusive and convective mass transfer in the presence of extensional creeping flow. The EP model significantly under predicts the experimentally determined dissolution rates for all experiments. In contrast, very good agreement is observed between the experimental

dissolution curves and the ZYM model when the saturation concentration of the micro droplet liquid ( $c_s$ ) is used as the only fitting parameter.



# **CHAPTER 1**

## **INTRODUCTION**

### **1.1 Microfluidics a general concept**

Microfluidic systems are used to manipulate and handle fluids at length scales of few microns to millimeter. The advancements in fabrication technology has enabled researchers from various fields of science and technology to use microfluidics devices for many different applications in life sciences, pharmaceutical industry, biochemical analysis and in the areas of chemical syntheses and environment testing respectively.<sup>1</sup> Microfluidic systems such as mixers, valves, pumps, reactors and actuators have been developed and are being used for applications such as biological sample trapping, microliter particle manipulation, fluid control, cytotoxicity analysis and rheological studies of fluids at microscale.<sup>2</sup> The micro total analysis systems [ $\mu$ Tas] also known as lab on a chip devices are such kind of microfluidic systems that incorporate sample handling, detection and high throughput analysis of micro particles such as cells and micro droplets. The integrative and parallel processing abilities of these lab on a chip devices with fast processing times and high throughput screening applications using micro scale quantities of test samples has had transforming impact on various chemical and biological analysis systems.

### **1.2 Micro Scale Fluid Flow**

Microsystems [ $\mu$ Tas] allow individual micro manipulation of biological molecules such as DNA and cells.<sup>3</sup> Micro fluidic devices have been used to trap, manipulate and sort biological samples. The physical properties of these  $\mu$ Tas systems are explained by using

scaling laws that express the variation of these physical properties while scaling in length  $L$ . In addition to these scaling laws dimensionless numbers such as Reynolds number and capillary number gave a greater insight into physical phenomenon occurring in microfluidic devices<sup>3</sup>. These dimensionless numbers are derived from fundamental equations governing fluid flow. The simplified Navier-Stokes equation is given as

$$\rho \frac{du}{dt} = -\nabla p + \eta \nabla^2 \mu + f \quad [1.1]$$

In this equation  $\rho$  is fluid density,  $\mu$  fluid velocity vector,  $\eta$  is viscosity and  $f$  represents the body forces. If the [Equation 1.1] is rendered dimensionless we can obtain the most common dimensionless parameter used to characterize fluid flow in micro fluidic devices. This parameter is known as “Reynolds number” [Re]. Re number is defined as

$$Re = \frac{\rho U_0 L_0}{\eta} \quad [1.2]$$

In [Equation 1.2]  $U_0$  is flow velocity and  $L_0$  is characteristic length of the micro channel.  $L_0$  is defined as length where the flow in the channel stabilizes. The Reynolds number is defined as the ratio of inertial effects to the viscous effects. Reynolds number is significantly low ( $Re \ll 2000$ ) at micro scale level employed in microfluidic devices. At these values of Reynolds number the viscous forces dominate and flow inside the microfluidic channels is termed as laminar flow. Low Reynolds number value ( $Re \ll 2000$ ) indicates that flow is laminar.<sup>4</sup> This thesis consists of two parts. The first focuses on development of microfluidic viscometer based on PDMS micropillars and the use of developed device for blood coagulation analysis. In second part of thesis hydrodynamic

trapping of immiscible oil microdroplets and their dissolution under creeping flow will be discussed.

### **1.3 Literature Review Microfluidic Viscometers**

The affluent assortment of industrially manufactured complex fluids and naturally occurring bio fluids has opened up new avenues to investigate the flow behavior and to characterize the rheological and viscoelastic properties of these fluids. Dynamic viscosity is indeed the most imperative reported material property of these fluids.<sup>5</sup> Many industrial processes require an accurate viscosity measurement of polymers<sup>5</sup>, oils<sup>6</sup>, paints, food, drugs and fermentation products during synthesis and production to achieve maximum efficiency and reduce cost. Evaluation of viscosity over a wide range of shear rates for both Newtonian and non-Newtonian fluids such as dilute polymer solutions,<sup>7</sup> bacterial fluids,<sup>8</sup> microalgae<sup>9</sup> and blood suspensions is difficult with large scale rheometry devices. The constraint emanates from the minimum force that can be accurately measured. This specifically affects the collection of shear viscosity data at very low shear rates. Presently, microfluidic devices reported in literature have not only the capability to handle low sample volumes but also provide a very precise control of flow and channel geometry, which renders a high degree of multiplexed and automated systems, allowing integration of flow imaging and optical methods. These distinct properties of microfluidic systems have made them especially suitable for the steady shear rheology/viscometry of complex fluids. In this part of dissertation, we briefly discuss the use of microfluidics for conducting shear viscometry of complex fluids and bio fluids with a focus on viscosity curves as a function of shear rate<sup>10,11</sup>. As discussed above lab on a chip devices provide a natural platform for fast, low-cost viscosity measurements using minute amounts of sample.<sup>1,12</sup>



## 1.4 Literature Review Hydrodynamic Trapping and Dissolution

Isolation and trapping of single micro particles be it be single cells, exosomes, proteins, DNA or droplets is at the core of point of care diagnostic systems and lab on chip device development. In this part of thesis we will discuss a novel non-contact based trapping technique for microliter droplets and their dissolution in creeping flow. Sauzade et al.<sup>13</sup> presented a hydrodynamic trapping technique based on sequential capture and encapsulation of single cells. Lieu et al.<sup>14</sup> reported another hydrodynamic tweezer device for Microparticle trapping with impact of geometrical design on flow inside the device. The trapping was confined to a cavity and a rectilinear oscillating flow was established. Kobel et al.<sup>15</sup> reported an efficiency of 97% with their cavity based trapping device. Kumano et al.<sup>16</sup> successfully trapped *tetrahymena thermophila* by designing a hydrodynamic circuit with multiple trapping sites. Banaeiyan et al.<sup>17</sup> used hydrodynamic forces to design a microfluidic trapping device with V-shaped trapping sites for particles as small as 4 $\mu$ m. Espulgar et al.<sup>18</sup> made use of centrifugal microfluidics to trap single cells of primary cultures. Zhou et al.<sup>19</sup> reported a multilayer device combining the effects of microfluidic valving techniques with trapping mechanisms. Khalili et al.<sup>20</sup> reported a T-shaped hydrodynamic trapping device. Optical tweezers<sup>21,22,23</sup> since the time of their conception have also been used to trap and manipulate droplets and cells for various applications.<sup>24,25,26,27</sup> . The trapping techniques discussed above required either an external trapping force or physical trapping site in order to trap particles. Tanyeri et al. <sup>28,29,30,31</sup> reported design of a non-contact hydrodynamic trapping device. The trapping mechanism is based upon creating an unstable equilibrium point at the junction of two laminar streams.

In this thesis we used this design to fabricate the microfluidic chips and show efficient trapping of microliter oil droplets as they dissolve in creeping flow. We will give a brief review about the eminence of the dissolution in chapters to come.

## **1.5 Organization of Thesis**

This dissertation will primarily discuss the design and testing of a micropillar based microfluidic viscometer and its apparent use to identify key parameters during blood coagulation pathway.

The overview in chapter 1 represents a general introduction to microfluidics and key scaling laws that govern them. It also presents a brief literature review of microfluidic viscometer devices reported in literature. A short literature review of microfluidic trapping techniques is also presented to have an insight into 2<sup>nd</sup> part of thesis.

In chapter 2 the focus would be on basic design parameters of microfluidic viscometer. The two fabrication methods used will be discussed along with different geometries that were conceptualized.

In chapter 3 the results of viscometry experiments for both Newtonian and Non-Newtonian fluids will be discussed. The experimental setup will be discussed in detail and a comparison of presented viscometer will be done with previously reported microfluidic viscometer devices.

In chapter 4 the use of microfluidic viscometer as a thrombus elastometer will be done and the results from coagulation experiments will be presented with an insight into advantages of using such a device instead of commercially available ROTEM device.

In chapter 5 CFD simulations for viscometer device will be presented and a comprehensive comparison of different geometries simulated will be discussed.

In chapter 06 a brief review on eminence of dissolution of liquid microdroplets will be discussed in reference to its use in pharmaceutical and food processing industry.

In chapter 7 the “Hydrodynamic trapping chip fabrication” along with experimental setup employed for trapping mechanism will be discussed.

In chapter 08 the results of dissolution experiments will be presented and conclusion would be drawn in comparison to Epstein-Plesset and ZYM model.

In chapter 09 holds the conclusion of dissertation and provides an insight to future directions of the work presented.

## **CHAPTER 2.**

### **VISCOMETER DESIGN AND FABRICATION**

#### **2.1 Introduction**

Polydimethylsiloxane (PDMS) belongs to a group of polymeric organo silicon compounds and is widely used for fabrication and prototyping of microfluidic chips.  $\mu$ pillars made out of PDMS have been used for various applications. Taparia et al.<sup>32</sup> reported a device with the ability to measure submicron deflections of micropillars to diagnose platelet dysfunction. Ting et al.<sup>33</sup> used an array of these so called micro posts to measure platelet aggregate force measurement. Sniadecki et al.<sup>34</sup> reported a similar device for measuring traction forces adherent cells. Beussman et al.<sup>35</sup> measured the stem cell derived cardiomyocyte contractility using an array micropillars. Judith et al.<sup>36</sup> reported that an array of micropillars can be used for analyzing whole blood clot contractility. Judith et al.<sup>37</sup> used magnetically actuated micropillars for measuring viscosity of fluids and this is only work reported in literature that uses an array of micropillars as a viscometer. The work reported by Judith et al.<sup>37</sup> requires an external actuation for the displacing micropillars and complex fabrication process. In this dissertation we report a simpler alternative.

#### **2.2 Microfluidic Design and Fabrication Al Mold**

Microfluidic viscometer device was fabricated using an aluminum (Al) mold Fig 1a. Micro-wells (Depth = 1500 $\mu$ m, Diameter = 300 $\mu$ m) were micromachined into Al mold using a 300 $\mu$ m diameter drill bit rendering an aspect ratio of 1:5 as shown Fig 2. The mold was polished and cleaned to remove any leftover residue following the micromachining process. The advantage of using such a mold is that no cleanroom is required but

micromachining is limited in achieving much higher resolution structures. PDMS (Sylgard 184) mixture was prepared using a 10:1 (base: crosslinker) ratio<sup>35</sup>. The mixture was degassed for 20 minutes before casting on to the Al mold, followed by a second degassing step to ensure that uncured PDMS completely fills the bottom of the micro wells. Subsequently, the Al mold with PDMS was baked in a vacuum oven at 75°C for 1 hour so that PDMS is fully cured. The PDMS slab was then peeled off from the Al mold by injecting ethanol so that the adhesion between the Al substrate and PDMS is reduced. This also ensures that  $\mu$ pillars remain intact during peeling off process. Two access holes were punched at the inlet and outlet for the fluid flow. The PDMS slab was then bonded to a glass slide (1"×3") by oxygen plasma to obtain a complete microfluidic viscometer device shown in Fig 2.1b.

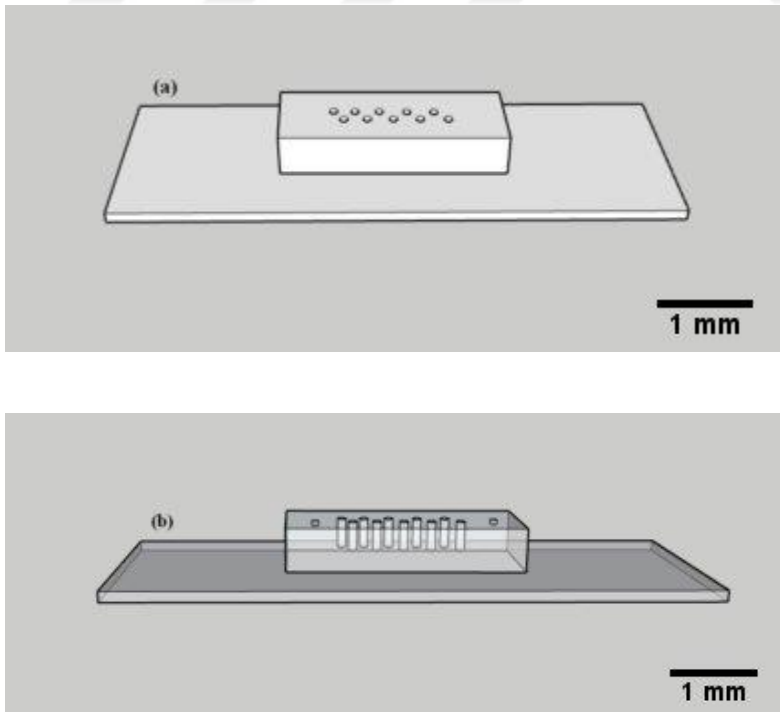


**Fig 2.1 (a) Micromachined Aluminium Mold ( $D = 300\mu\text{m}$ ,  $H = 1500\mu\text{m}$ ). (b) PDMS microfluidic chip bonded on glass slide (1"×3").**

The microfluidic viscometer design shown in Fig. 2.1 (a) and (b) is the final design that was used to fabricate micropillars. It has been established previous studies that aspect ratio plays an important role in  $\mu$ pillar bending/displacement.<sup>38,39,40</sup> . In addition to the eminence of aspect ratio it was found out that it is imperative to provide maximum resistance to the fluids under test to have maximum  $\mu$ pillar displacement. The initial design of viscometer contained a straight micropillar array with 300  $\mu$ m wall spacing on either side of the pillar. This allowed most of the liquid to pass through the sides with minimum interaction with the pillar.

In order to overcome this discrepancy the design was modified as shown in Fig. 2.1a and 2.1b. The micropillar distance from the channel distance was 450  $\mu$ m from one side and 150  $\mu$ m from the other side. The total width of the channel remained to be 900  $\mu$ m but due to alternate design of the array the fluidic resistance that built up on channel was much higher and so the total force acting on the pillars was much higher as well. It was observed that another factor that effects the micropillar displacement is the distance between the pillar tip and channel ceiling. In earlier designs the distance between the pillar tip and channel ceiling was 300  $\mu$ m which made the total channel height to be 1800  $\mu$ m. In the design shown in Fig 2.1 this distance was reduced to be 100  $\mu$ m rendering the total channel height to be 1600  $\mu$ m. The effects these design parameters will be discussed in detail in chapter 5 where CFD simulations of the viscometer will be presented.



**Fig 2.2. Microfluidic Channel with  $\mu$ pillar diameter of 300  $\mu$ m using Al mold.**

### 2.3 Microfluidic Design and Fabrication of Si Mold

In this section we will discuss the fabrication of an array of micropillars using a Si mold/substrate. The aspect ratio of pillars obtained in this process was 1:3. The pillar height achieved was 75  $\mu\text{m}$  and diameter 25  $\mu\text{m}$ .

A 4" (inch) Si wafer was used as substrate in this case. In order to have better adhesion wafer was cleaned for 10 minutes in acetone and then heated up to 35°C. The next step in wafer cleaning was 5-minutes in 2-propanol and eventually the wafer was rinsed in DI water. The wafer was pre-baked at 200°C for 05 minutes and was left to cool down. The next step was spin coating SU-8 2050 at 500 RPM for 10 sec at a ramp of 100 RPM and then 1850 RPM for 30 sec at a ramp of 100 RPM. A soft bake step was performed starting from 40 °C with a ramp 3°C/min up to 95 °C for 25 minutes. This gradual increase of temperature helps to prevent SU-8 from cracking. The wafer is then cooled down to 40 °C on hot plate. After this soft baking step the wafer is exposed to UV using a mask aligner for 16 sec to obtain holes with a diameter of 25  $\mu\text{m}$ . A post exposure bake step follows starting from 40 °C with a ramp 3°C/min up to 95 °C for 12 minutes and then cooled down to 40 °C on hot plate. In order to remove extra photoresist a developing step was performed by putting 03 petri dishes in a sonicator with SU-8 photoresist developer in them. The wafer was put in each petri dish for 10 minutes while the sonicator shakes of the unwanted photoresist. It might be necessary to add a sonication step if you still see some residual photoresist. The wafer is then dipped into 2-propanol for about 2 minutes and then finally rinsed with DI water. The wafer was hard baked to 150 °C for 30 minutes with a ramp of 180 °C/hr. The process flow of Si wafer fabrication is shown in Fig. 2.3.

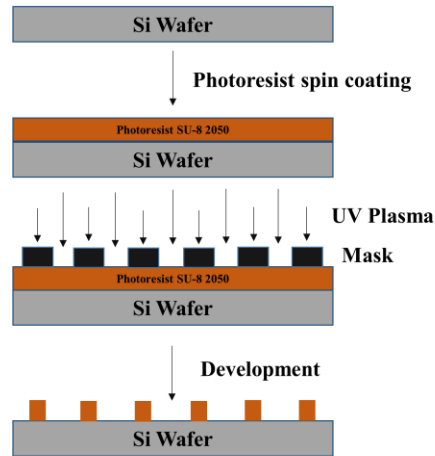


**Fig 2.3. Process flow for Si wafer microfabrication.**

PDMS (Sylgard 184) mixture was prepared using a 10:1 (base: crosslinker) ratio<sup>35</sup>. The mixture was degassed for 20 minutes before casting on to the Si mold, followed by a second degassing step to ensure that uncured PDMS completely fills the bottom of the micro wells. Subsequently, the Si mold with PDMS was baked in a vacuum oven at 75°C for 1 hour so that PDMS is fully cured. The PDMS slab was then peeled off from the Si mold by injecting ethanol so that the adhesion between the Si substrate and PDMS is reduced. This also ensures that circular  $\mu$ pillars as shown in Fig. 2.4a remain intact during peeling off process. Two access holes were punched at the inlet and outlet for the fluid flow. The PDMS slab was then bonded to a glass slide (1"×3") by using oxygen plasma to obtain a complete microfluidic viscometer device. In order to verify the  $\mu$ pillar height and diameter SEM measurement was performed the results are shown Fig.2.5 a, b, c and d. In addition to circular  $\mu$ pillars square shaped  $\mu$ pillars were also fabricated shown in Fig. 2.4b and employed for viscosity experiments. It was also observed that square shaped  $\mu$ pillars



displace more in comparison to circular micropillars due to increased fluid structure interaction.

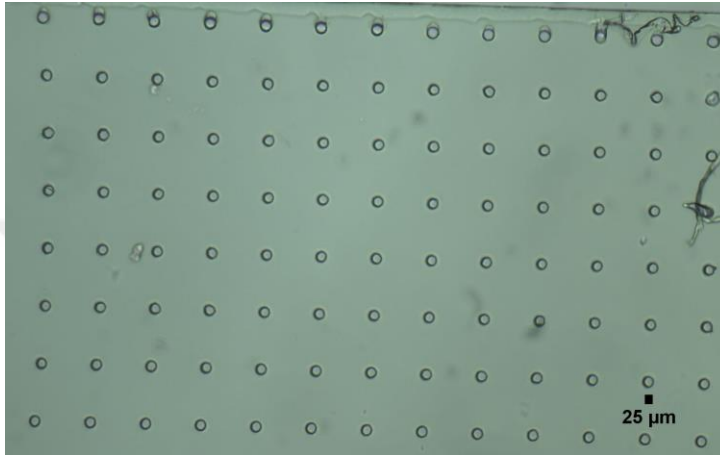


**Fig 2.4a. Microfluidic Channel with circular  $\mu$ pillar diameter of 25  $\mu\text{m}$  using Si mold.**

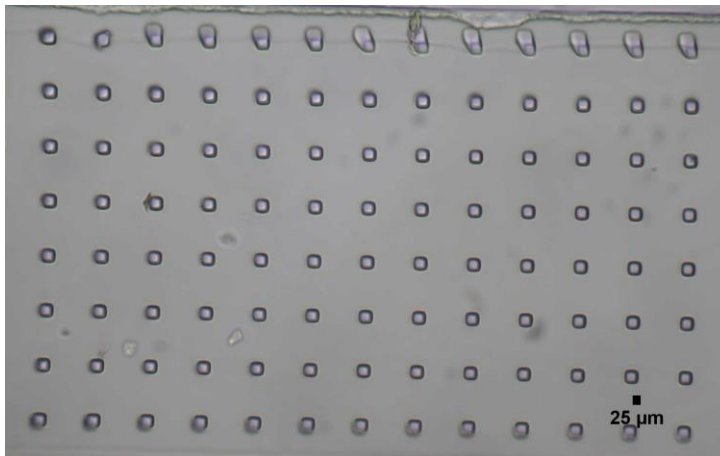


**Fig 2.4b. Microfluidic Channel with square  $\mu$ pillar diameter of 25  $\mu\text{m}$  using Si mold.**

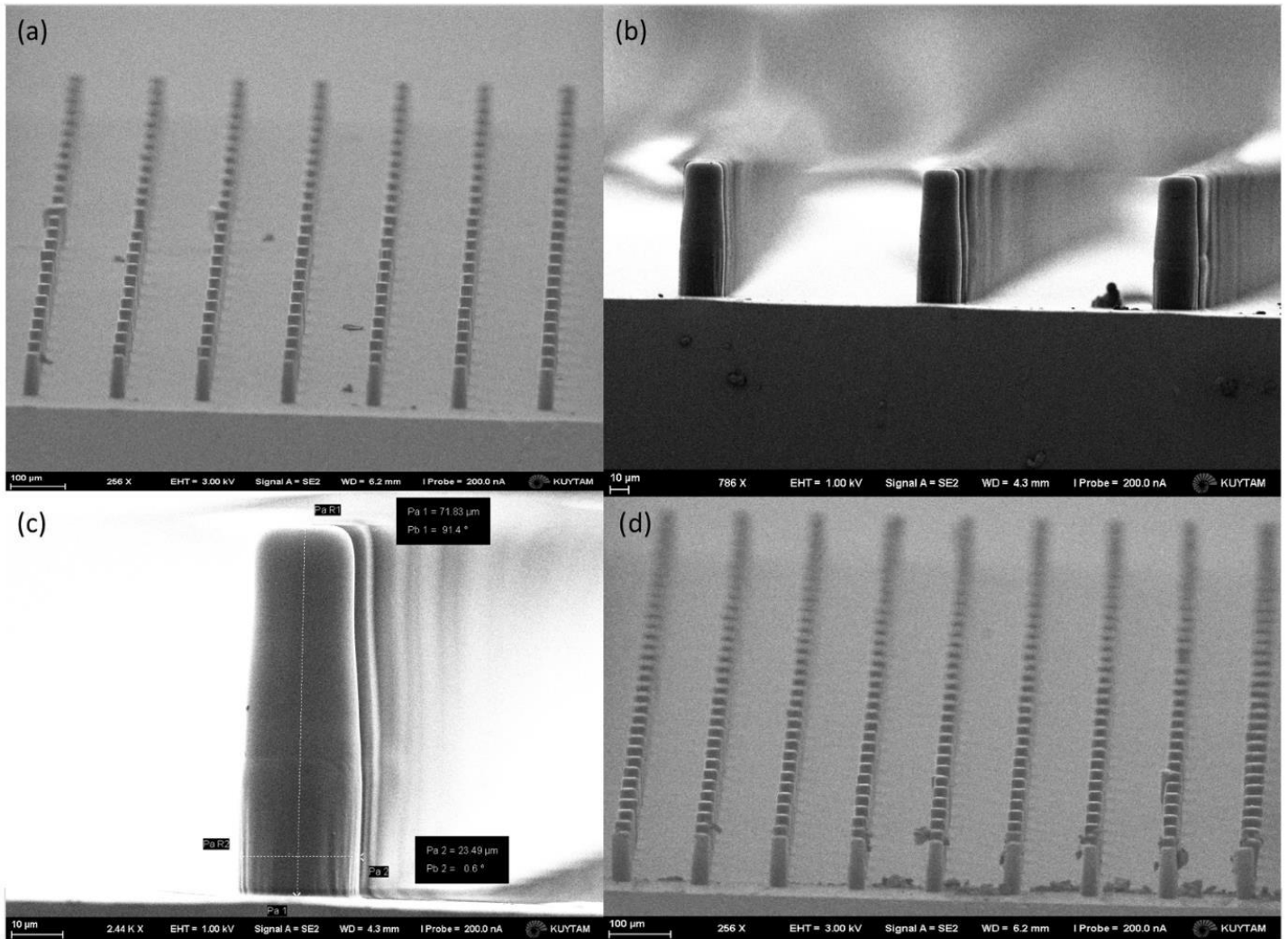


**Fig 2.5. (a), (b), (c) and (d) SEM image circular of micropillar array.**

## **CHAPTER 3.**

### **MICROPILLAR BASED VISCOMETER**

#### **3.1 Introduction**

Viscosity is an important material property of chemical and biological fluids<sup>5</sup>. Many industrial processes require an accurate viscosity measurement of polymers<sup>41</sup>, oils<sup>5</sup>, paints, food, drugs and fermentation products during synthesis and production to achieve maximum efficiency and reduce cost. Similarly, monitoring and analyzing changes in viscosity of biological fluids such as blood<sup>42</sup>, plasma, cerebrospinal fluid and amniotic fluid is essential in medical diagnostics. Therefore, measuring viscosity by facile, rapid and cost-efficient methods using low sample volumes is of great importance in numerous industrial and medical fields. Microfluidic devices provide a natural platform for fast, low-cost viscosity measurements using minute amounts of sample. To this end, researchers have recently developed several miniaturized viscometers using microfabrication and microfluidics technology. In literature most of the microfluidic viscometers reported are based on measuring pressure drop inside a microchannel for given flow rate.<sup>43</sup> Another work reported in literature is where measurement method is based on estimating pressure inside a microfluidic chip by measuring the width ratio between reference and sample fluids using images captured by smartphone camera.<sup>44</sup> Guillot et al.<sup>45</sup> measured viscosity of fluids flowing in a microchannel as a function of shear rate. They calculated the mean shear rates sustained by the sample fluid by optically measuring the shape and position of the interface between two immiscible liquids flowing in parallel to each other at constant flow rates in a microchannel. These methods are based on measuring the position and

curvature of co-flowing streams and then calculating the viscosity numerically from the interface of the geometry. The advent of droplet microfluidics has led researchers to design miniature viscometer devices based on measuring droplet velocity as they pass through a constriction and measuring droplet length.<sup>42,46,47</sup> This method finds its advantages by using sample volume in nano liter range (100 nL). Kang et al.<sup>43</sup> presented a label free method for measuring viscosity of both Newtonian and Non-Newtonian fluids by adopting fluid-switching phenomenon based on hydrodynamic balancing in microfluidic channels. Recent developments in the field of micro and nanofabrication have also led to development of micro cantilever based viscometers. The viscosity measurement in such devices is based on recording and analyzing the response of cantilevers under photo thermal vibrations.<sup>48</sup> Soft cantilevers fabricated from Polydimethylsiloxane (PDMS) have been used before as force sensors to measure cell traction forces<sup>34</sup>, cell derived contractility<sup>35</sup> and clot contractility<sup>36</sup>. Recently, a magnetically actuated viscometer device based soft cantilevers fabricated using PDMS was reported.<sup>37</sup> The viscosity measurement depends not only on the mathematical model derived for the system but also the magnetic properties of the so called micro posts. In this study we present a novel and simple method to measure the viscosity of Newtonian and Non-Newtonian fluids by measuring deflection of PDMS micropillars ( $\mu$ pillar) fabricated by soft lithography using a micromachined aluminum mold. Fluids with different viscosity values were flowed at different flow rates inside the microchannel and micropillar deflection is recorded and analyzed. The analysis is based on estimating the micropillars displacement from static to flow condition. An increase in displacement at constant flow rate is directly correlated to viscosity. To our knowledge this is the first study to measure viscosity of an unknown fluid by measuring displacement of micropillars in

continuous flow. The measurement method presented in this study finds its distinct edge over previous studies by measuring the response of soft PDMS cantilevers under wide range of flow rates. The ease in fabrication and robustness of the mold represent the other two distinct advantages over previous devices. The experiments were conducted at flow rate range between (15ml/hr – 105ml/hr) for Newtonian fluids and for non-Newtonian fluids (blood) the flow rate range used (30ml/hr- 90ml/hr).

### **3.2 Sample fluid preparation**

The sample fluids were prepared by mixing glycerol  $C_3H_8O_3$  100% obtained from (PamReac Applichem, Barcelona, Spain) with distilled water (DI) at different ratios to obtain mixtures with a range of viscosities including 5cP, 10cP, 15cP, 25cP, 50cP, 75cP, 100cP. The viscosities of the prepared solutions are verified by a conventional rotational viscometer (Brookfield, Programmable DV-II +, Middleboro, MA).

### **3.3 Experimental setup**

The experimental setup consists of a microfluidic chip, a microscope (Nikon Eclipse TS100 series), a syringe pump (Harvard Apparatus), a computer and a CMOS camera (Point Grey Grasshopper3) (Fig. 3.1). The sample fluid is injected into the microfluidic chip using a syringe pump. The microfluidic device is initially filled with the sample fluid. The viscosity is determined directly by measuring micropillar deflection. The images of micropillars within the microfluidic device are acquired under no flow condition as well as at different flow rates between 15ml/hr – 105ml/hr. The micropillar deflection is subsequently determined by analyzing images using custom developed image processing tools.

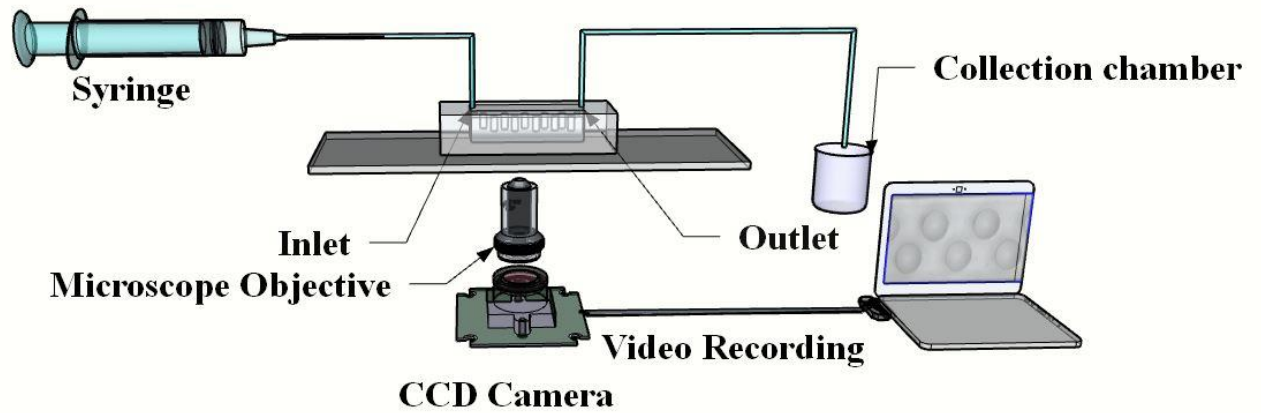


**Fig 3. Sketch of experimental setup. A microscope (Nikon Eclipse TS100 series) for imaging, a syringe pump (Harvard Apparatus) for infusing liquid, a computer and a CMOS camera (Point Grey Grasshopper3) for imaging and recording.**

It was imperative during the experiment that the channel was void of any bubbles as this could affect the measurements.

### **3.4 Experimental methods**

The measurement of viscosity using micropillars is based on determining deflection of these microstructures as fluids of different viscosities were infused through the microfluidic chip. Fluid flowing through the microfluidic device interacts with the

micropillars resulting in their deflection, typically proportional to the viscosity of the fluid (Fig 3.2). We initially determined average micropillar deflection at a given flow rate using standard glycerol/water mixtures for various viscosities. For this purpose, micropillars were imaged continuously as the sample fluid flows inside the device and interacts with the micropillars. These recorded videos were later analyzed using a customized code to determine micropillar deflection. The deflection values were then used to generate a calibration curve relating the viscosity values to micropillar deflection. These calibration curves were then used to determine the viscosity of unknown solutions at a given flow rate. We determined the sensitivity and range of microfluidic viscometer by measuring the viscosity of glycerol/water mixtures ranging from distilled water (DI) 1cP to 100cP glycerol (100% at 25 °C).

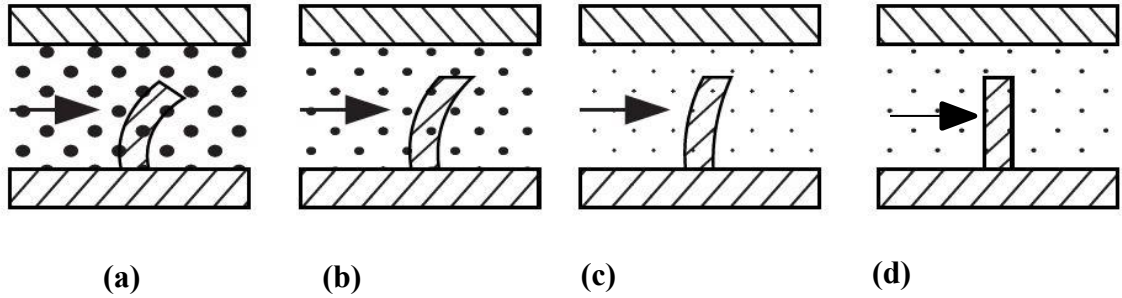


**Fig. 3.2 (a), (b), (c) and (d) Pillar displacement with decreasing viscosity. It can be seen that cantilever displacement decreases from (a) – (d) as the viscosity of the fluid decreases with diameter of the black spots represent viscosity of fluid.**

### 3.5 Image Analysis

Image analysis of the recorded videos was performed with custom build program. The videos were recorded under two conditions static (no flow in channel) and dynamic (fluid flow in channel). The first 25 frames of each recorded video were with no fluid flow in channel and then flow was started using a syringe pump. The micropillar tip is selected as the detection point. The displacement observed for the first static frame is compared with each of the subsequent frames to have correct displacement value at each frame and distance formula is used to calculate the displacement. It was observed that displacement is maximum in direction of flow.

It can be seen from the results shown in Fig. 3.3 that displacement increases rapidly as the fluid starts to flow in the microchannel containing micropillars and then saturates depicting the maximum micro pillar displacement. Brücker et al.<sup>49</sup> also reported such a behavior for displacement of micropillars in laminar flow. The final displacement is value is calculated by taking the average of so called saturation region as it depicts maximum micropillar displacement.

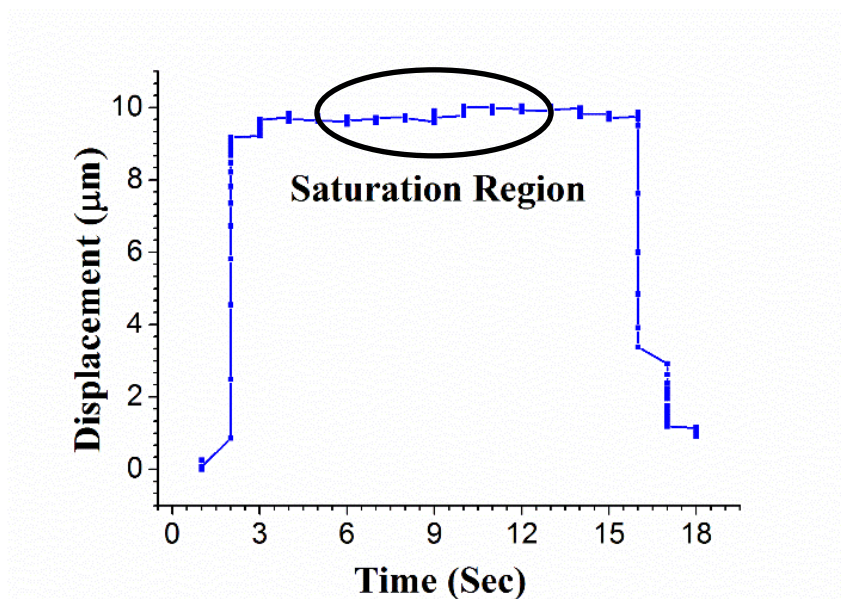




**Fig. 3.3 Displacement Vs Time for a single  $\mu$ Pillar depicting. Displacement increases with time and saturation region represents the maximum micropillar displacement.**

### **3.6 Viscosity Measurements Newtonian Fluids**

#### **3.6.1 Sensitivity and dynamic range:**

The microfluidic viscometers reported in literature vary from capillary viscometers, sliding plate viscometers, co-flowing viscometers and micro mechanical viscometers. These miniaturized microfluidic viscometer devices report dynamic range of sensitivity which will be discussed in this section and compared to sensitivity of our viscometer device. Zou reported sensitivity of 0.69 cP for their PDMS microfluidic viscometer.<sup>50</sup> The measurement principle was based on laminar flow inside a microchip. A viscosity range of 1-600 cP was reported by Srivastava for their capillary based viscometer and shear rate range of 5-1000  $\text{s}^{-1}$ .<sup>10</sup> The sensitivity reported for such a device is 1cP at a shear rate of  $10^4 \text{ s}^{-1}$ . Han and Zheng reported an improved sensitivity and shear range for a modified design of Srivastava's device.<sup>51</sup> Kang performed studies for high shear microfluidics and discussed their application for rheological studies.<sup>11</sup> They reported a shear rate range of  $10^6 \text{ s}^{-1}$  with a sensitivity down to 1 cP. Pan resented a microfluidic viscometer that used in situ sensors to measure the viscosity of fluids flowing in a straight microchannel. The shear rate range for such a viscometer was reported to be in range of  $(10^{-2} - 10^4) \text{ s}^{-1}$  with a viscosity measuring range between  $(10^{-1} - 10^4) \text{ cP}$ .<sup>52</sup> Lan with their co-axial microfluidic viscometer device reported a dynamic range of 0.6-40 cP which renders a sensitivity of 0.6 cP for this type of device.<sup>53</sup> Li reported a viscometer device based on droplet length with sensitivity of device depending upon the ration droplet length to viscosity of the aqueous phase. The

shear rate range is limited to lower flow rates ( $\mu\text{L}/\text{min}$ ) range as it is necessary to generate droplets in flow focusing microfluidic geometry.<sup>46</sup> A hydrodynamic focusing rheometer reported a viscosity measuring range of (1cP-10000cP). They report a shear rate in range of  $(10^1 - 10^3) \text{ s}^{-1}$ .<sup>54</sup> The devices discussed above are mostly based on measuring viscosity by calculating pressure drop or flow rate of the fluid flowing in channel or by co-flowing a sample fluid in a T-shaped microfluidic channel. Most of these viscometers not only require complex fabrication process but also require tedious calculations and measuring techniques to find out the viscosity of an unknown fluid.

To the best of our knowledge Judith et al.<sup>37</sup> presented the only micro pillar/post based microfluidic viscometer. Magnetically actuated micro pillar array was used to measure the viscosity of the fluid. They reported a viscosity measuring range of (5cP–5000cP) with a sensitivity of 1cP. The measuring method explained here requires a complex Opto-magnetic experimental setup and complex mathematical modelling to have an accurate viscosity value. We present here a micropillar based viscometer with one step soft lithography fabrication process with no external actuation required for fluid flow and viscosity is given by measuring displacement of these micropillars as fluid interacts with these pillars while flowing through the channel. We found out that our current microfluidic geometry allows us to determine viscosities between 1-100cP with a sensitivity down to 0.5cP.

The experiments were divided in two parts. In order to have a better understanding of sensitivity of our viscometer glycerol/water solutions (2cP, 2.50cP, and 3cP) were prepared. After performing numerous experiments at various flow rates a range was selected for sensitivity experiments (45ml/hr – 105ml/hr). The results of these experiments

are shown in Fig.3.4. It can be observed from the results shown in Fig.3.4 that displacement increases linearly with flow rate. The results predict a sensitivity of 0.5cP for our device.

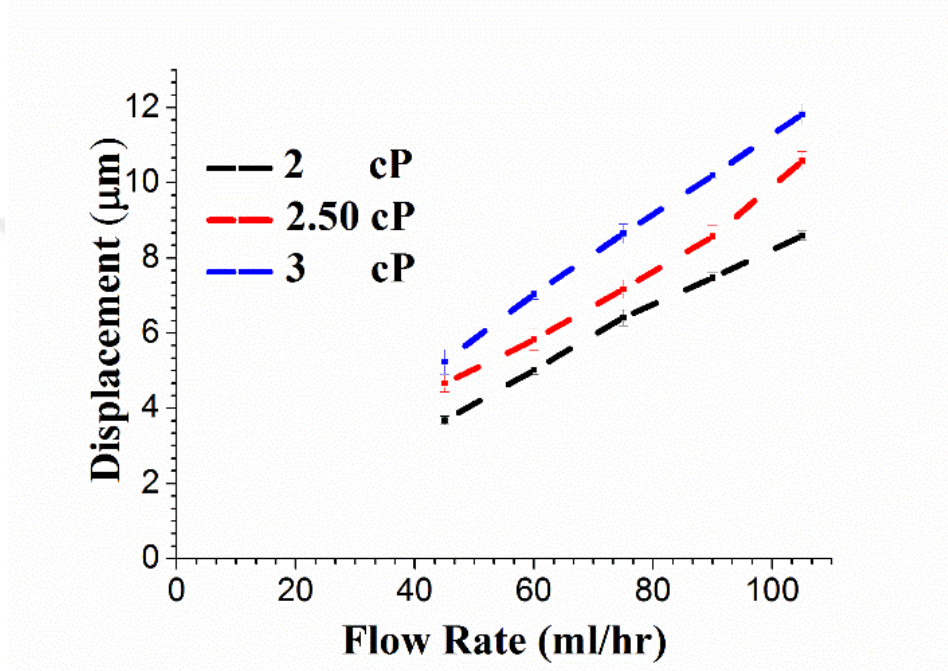


**Fig.3.4. Flow Rate Vs Displacement (2cP - 3cP) sensitivity experiments. A sensitivity of 0.5 cP is observed for our device.**

The sensitivity of our microfluidic viscometer lies within the acceptable range reported in literature<sup>5,55,50</sup>. The results shown in Fig.3.4 were also verified through simulations using a COMSOL Multiphysics and are discussed in Chapter 5. Experiments were also performed to find out the dynamic range of our viscometer. In order to have an in depth understanding of chip to chip variation experiments were performed with 4 different devices. The chips were calibrated before starting the experiment by flowing 1cP (DI) water through the devices at a flow rate range (15ml/hr – 105ml/hr) used in experiments.

The results for the calibration experiments are shown in Fig.3.5. The flow rate range was selected to be (15ml/hr – 105ml/hr) and solutions with viscosities (5cP – 100cP) were tested. The calibration data provided a better understanding of the device to variation and separating non-functional devices from functional devices.

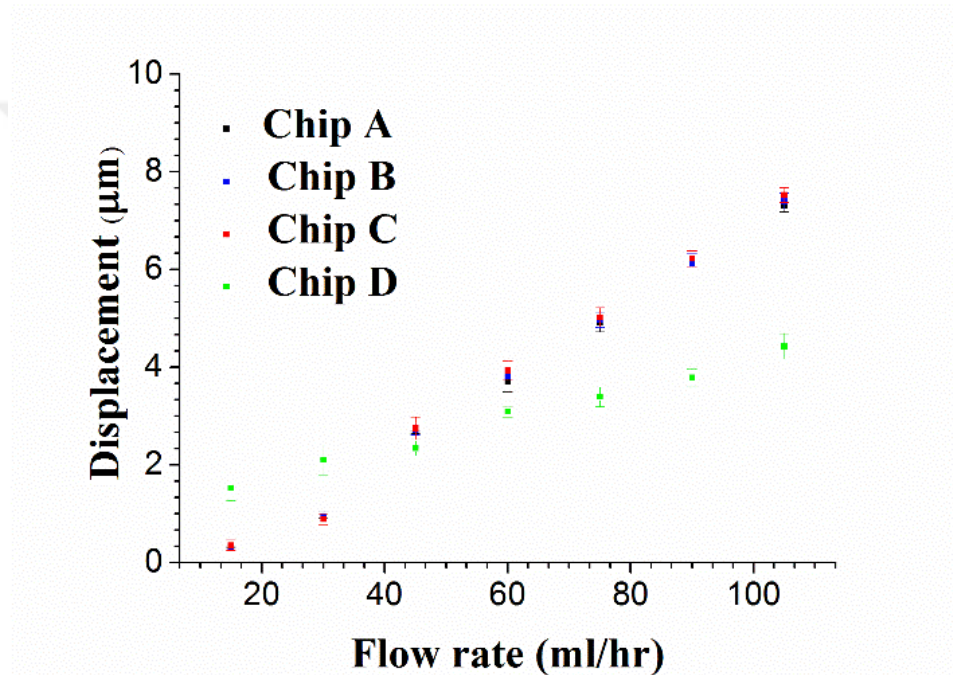
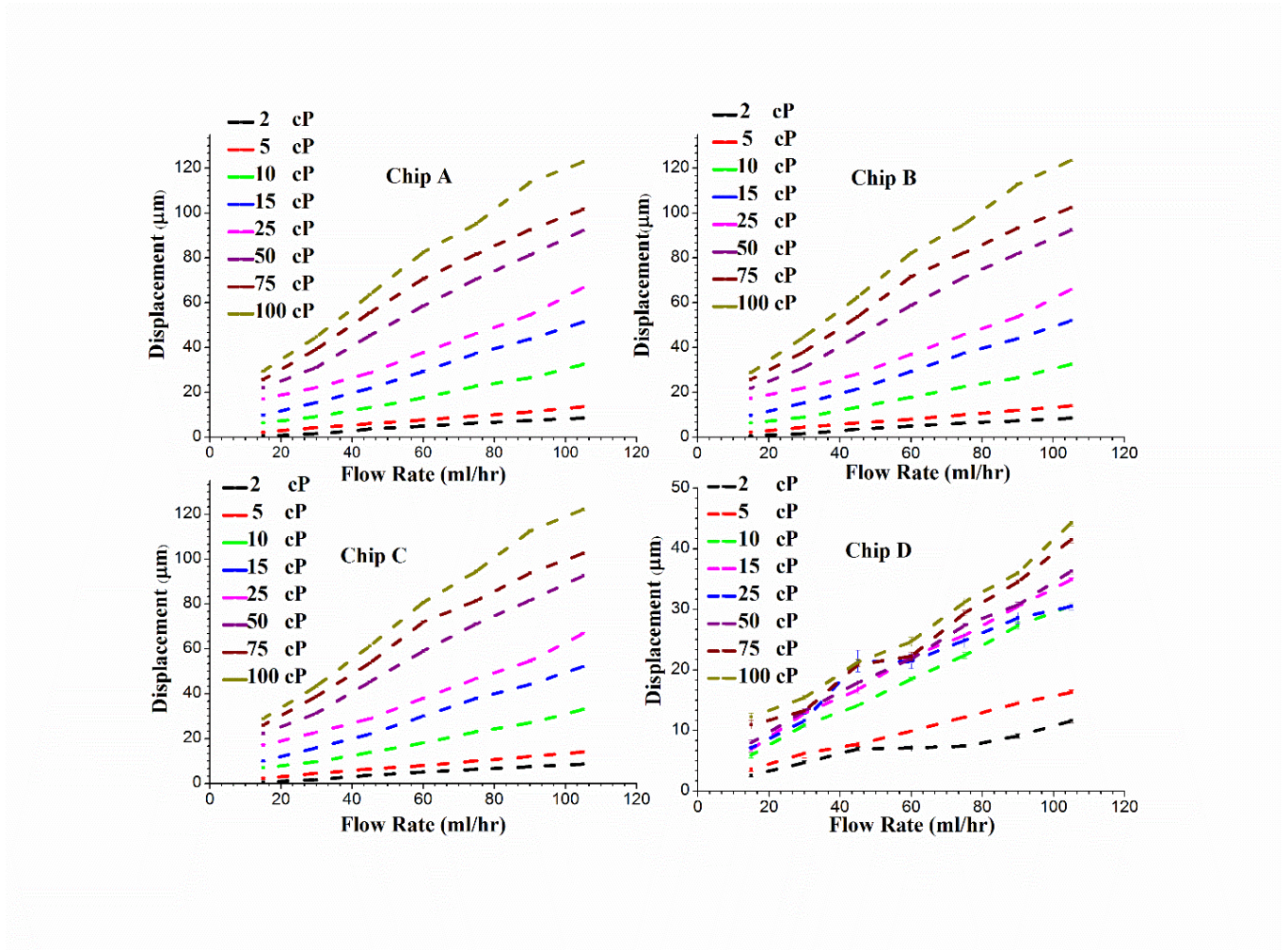


**Fig.3.5 Calibration using 1cP (DI water) Chip A, Chip B, Chip C and Chip D. chip D represents a non-functional chip.**

To find out dynamic range of our viscometer device we designed another set of experiments with flow rate range (15ml/hr – 105ml/hr) and for viscosity range between (2cP – 100cP). The results shown in Fig.3.6 depict the dynamic range of our viscometer device. It can be seen from the results that displacement increases linearly as flow rate is increased from 15ml.hr-105ml/hr for chips A, B and C. The chip D represents a non-functional device as the increase in displacement is not linear as the flow rate is increased.

This observation was further strengthened when viscosity was plotted against displacement and is discussed in next section. We attribute this discrepancy to chip manufacturing process which can render a non-functional device. The above discussion renders a viscosity measuring range of (0.5 cP to 100cP) and a shear rate in range of  $(250 - 10^3) \text{ s}^{-1}$  with sensitivity of 0.5 cP for our viscometer. The shear and viscosity ranges reported for our



device are within the acceptable values reported in literature. We are able to flow liquids under test from very low shear rates to very high shear rates which is a distinctive advantage for our device.

**Fig.3.6. Flow Rate Vs Displacement (dynamic range) Chip A, B, C and D Flow rate (15ml/hr – 105ml/hr). Displacement increases linearly as the flow rate is increased. (No of Experiments N=3) for each chip at each flow rate.**

### **3.6.2 Fixed flow rate experiments:**

In order to test our device as viscometer, experiments were performed at fixed flow rates for solutions of viscosity ranging from 2cP-100cP. The result for these experiments are shown in Fig. 3.7. A 2<sup>nd</sup> order polynomial equation was used to mathematically fit our experimental data as shown in Fig. 3.7.

The experiments were performed at 4 different flow rates. (15ml.hr – 60ml/hr) with three readings taken at each flow rate. This gives an N=3 for each chip at each flow rate. The results clearly vindicate the observation made about non functionality of “Chip D” during dynamic range and calibration experiments.

It can be seen from the results shown in Fig.3.7 that as viscosity is increased beyond 25cP the displacement does not increase linearly. The non-linear behavior above 25 cP can be explained due to the fact that PDMS has nonlinear elastic response. Du et al.<sup>56</sup> discussed the viscoelastic properties of PDMS micropillars and their applications in measuring cellular forces.



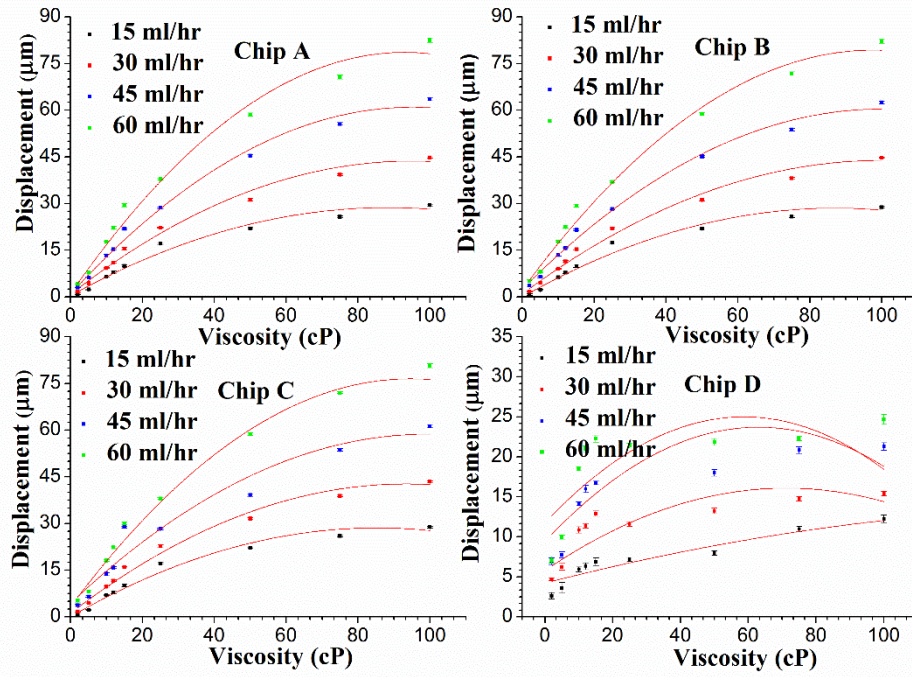


**Fig.3.7 Viscosity Vs Displacement fixed flow rate (15m/hr – 60ml/hr) Chip A, B, C**

**and D with 2<sup>nd</sup> order polynomial fitting. Displacement increases linearly from (2cP – 25cP). A non-linear behavior is observed above 25cP. (No of Experiments N=3) for each chip at each flow rate.**

Similarly, Yu et al.<sup>57</sup> came up with analysis of PDMS micro cantilevers and reported a non-linear behavior of PDMS micro cantilevers. Lin et al.<sup>58</sup> reported that due to smaller size of PDMS micro pillars the slender beam theory renders in applicable and in order to analyze such structures shear deflections must be taken into account. Lin et al.<sup>56</sup> reported that due to viscoelastic behavior of PDMS the Young's modulus changes with loading rate and

elapsed time. Vanlandingham et al.<sup>59</sup> discussed the non-linear responses of PDMS sample for rheometry and indentation measurements.

Fig. 3.8 shows the fitted results for our experiments at fixed flow rates. The resulting fitting equation is a 2<sup>nd</sup> order polynomial equation.

$$Y = \text{Intercept} + b_1x + b_2x^2 \quad [3.1]$$

In this equation Y is displacement of the fluid under test at a fixed flow rate  $b_1$  and  $b_2$  are constants of the quadratic equation and x is viscosity of the fluid under test. By inserting the displacement Y (recorded through experiments) in equation 3.1 for a fluid under test.

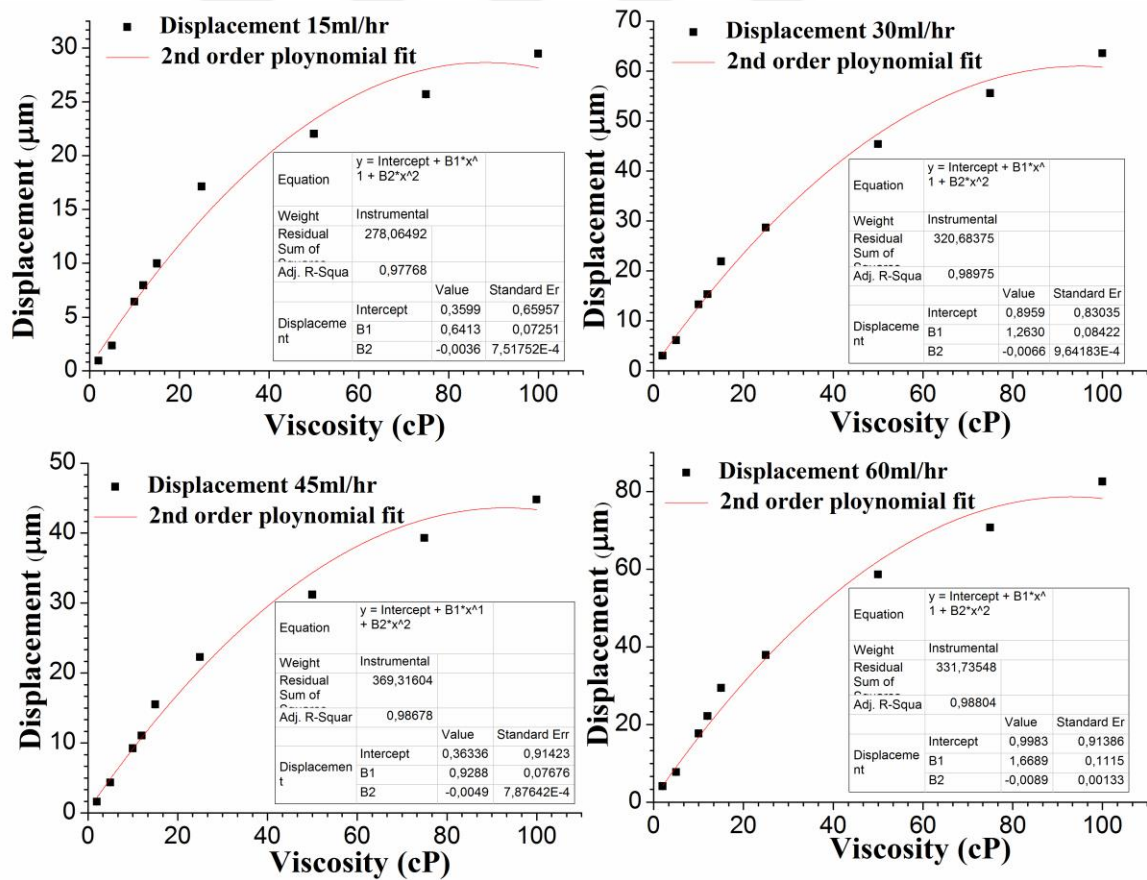




**Fig.3.8 Viscosity Vs Displacement fixed flow rates (15ml/hr – 60ml/hr) for Chip A. A 2<sup>nd</sup> order polynomial equation ( $Y = \text{Intercept} + b_1x + b_2x^2$ ) is used to fit the data.**

By inserting the displacement  $Y$  (recorded through experiments) in equation 3.1 for a fluid under test. By using the fitting parameters “Intercept,  $b_1$  and  $b_2$ ” we were able to calculate the viscosity of an unknown fluid. The results with fitting equation for “Chip A” are shown in Fig.3.8. In order to calculate the viscosity of an unknown fluid using our viscometer device a commercially purchased fluid (Decanol oil = 11.91 cP).<sup>60</sup> was used. Experiments were performed for flow rates (15ml/hr – 60ml/hr). The decanol flow rate vs displacement results are shown in Fig.3.9.

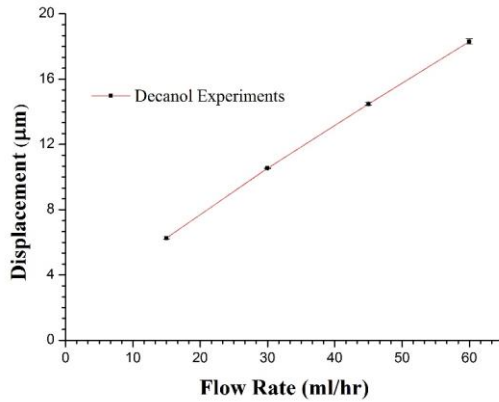


**Fig.3.9 Flow Rate Vs Displacement Decanol (11.91 cP). Flow rate range (15ml/hr – 60ml/hr).**

The displacement at each flow rate was measured. A 2<sup>nd</sup> order polynomial equation ( $Y = \text{Intercept} + b_1x + b_2x^2$ ) that is used to fit our experimental data was then solved to obtain the viscosity of decanol at each flow rate. The calculated results are shown in Table T3.1.

The percent error was calculated for all the devices using Equation2 and is shown in table T3.1

$$\% \text{Error} = \frac{\text{Calculated viscosity value} - \text{theoretical viscosity value}}{\text{theoretical viscosity value}} \times 100\% \quad [3.2]$$

The average percentage error for chip “A”, chip “B” and chip “C” is (2.68%, 7.91% and 7.005%) respectively. This variation in error is an indication of chip to chip variation due to fabrication process. The percentage error reported in literature for various microfluidic viscometers is in a similar range as reported in this particular case. Li reported an error of 5% where they calculate viscosity by measuring droplet length in a microfluidic channel.<sup>46</sup> Lan reported an error of 4-7 % for their co-flowing microfluidic viscometer.<sup>53</sup> Zou et al.<sup>50</sup> reported an error of less than 1% with a PDMS microfluidic viscometer fabricated using micro wire molding technique. Srivastava et al.<sup>10</sup> designed a nanoliter capillary viscometer to measure the viscosities of blood plasma and other non-Newtonian fluids. The error reported for such a device was 10% for water and 3% for plasma. Nguyen.<sup>54</sup> reported an error between 5-24% for their hydrodynamic focusing viscometer device. The percentage error for our device varies not only from chip to chip but also changes with flow rates. It can be seen from the results shown in T3.1 that percentage error of our device lies within the range reported in literature.

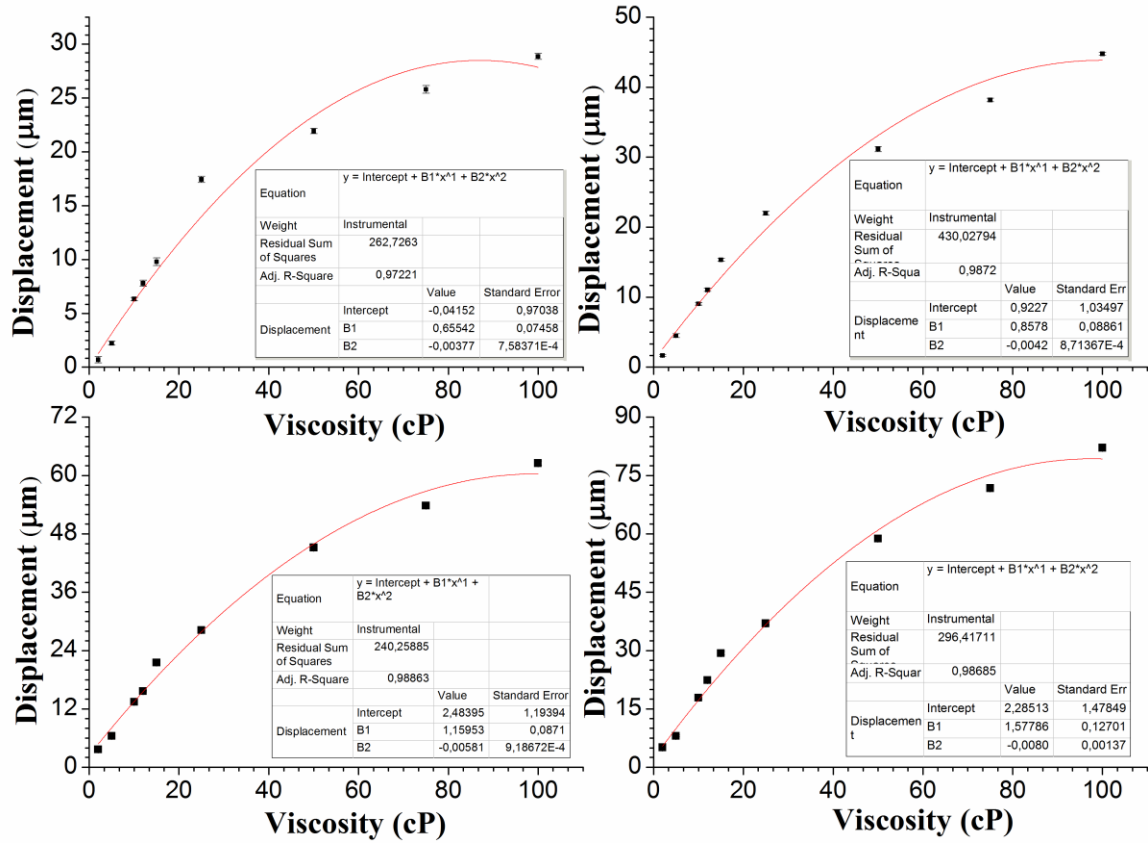


**Fig.3.10 Viscosity Vs Displacement fixed flow rates (15ml/hr – 60ml/hr) for Chip B.**

**A 2<sup>nd</sup> order polynomial equation ( $Y = \text{Intercept} + b_1x + b_2x^2$ ) is used to fit the data.**

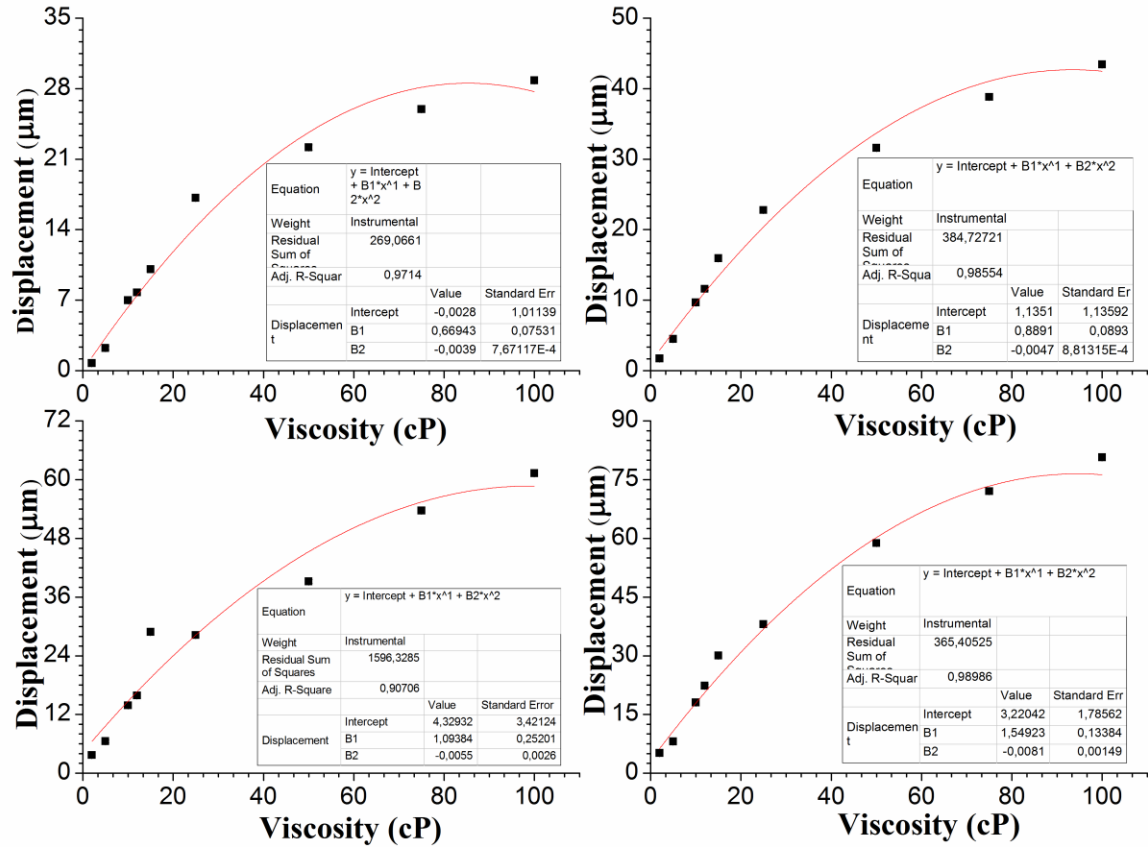


**Fig.3.11 Viscosity Vs Displacement fixed flow rates (15ml/hr – 60ml/hr) for Chip C.**

**A 2<sup>nd</sup> order polynomial equation ( $Y = \text{Intercept} + b_1x + b_2x^2$ ) is used to fit the data.**

The measurement method presented here is an indirect measurement technique. The simplicity of this method where by merely measuring the response of soft PDMS cantilevers under applied force gives the viscosity of fluid under test makes it an excellent alternative for the existing methods for measuring viscosity. These experiments were the basis of blood coagulation studies which will be discussed in detail in next chapter where both the aluminum and micro fabricated devices were used.

<b>Flow Rate (ml/hr)</b>	<b>Calculated Viscosity (cP) Chip A</b>	<b>% Error Chip A</b>	<b>Calculated Viscosity (cP) Chip B</b>	<b>% Error Chip B</b>	<b>Calculated Viscosity (cP) Chip C</b>	<b>% Error Chip C</b>
15	10.88	8.64	12.89	8.22	12.51	5.03
30	11.84	0.58	13.79	15.7	12.58	5.62
45	11.81	0.83	12.06	1.2	11.18	6.12
60	11.83	0.67	12.69	6.54	13.25	11.25

**Table T1. Calculated Viscosity using 2<sup>nd</sup> order polynomial equation**

### **3.7 Viscosity Measurements non-Newtonian Fluids**

In order to analyze the performance of our viscometer device for non-Newtonian fluids we chose “whole blood” as sample fluid. The viscosity of the blood sample was 1<sup>st</sup> tested using commercial viscometer (Brookfield, Programmable DV-II +, Middleboro, MA) at various shear rates and results were plotted as shown in Fig.8. It can be seen that viscosity of whole blood is a function of shear rate so that when the shear rate is increases the viscosity of the blood decreases<sup>61,62</sup>. Mehri et al<sup>63</sup>.also measured the viscosity of blood at different shear

rates in a Y-shaped microfluidic channel by flowing PBS as reference fluid (less viscous) with blood and reported a decrease in viscosity of blood at increasing shear rate. In our device we attribute the change in displacement of micropillars to change in viscosity of the fluid. The experiments were performed using the setup shown in Fig.2 with a slight modification of constantly heating the device to 37°C to have consistent temperature with human body. This again an indirect measurement method to calculate viscosity of non-Newtonian fluids.

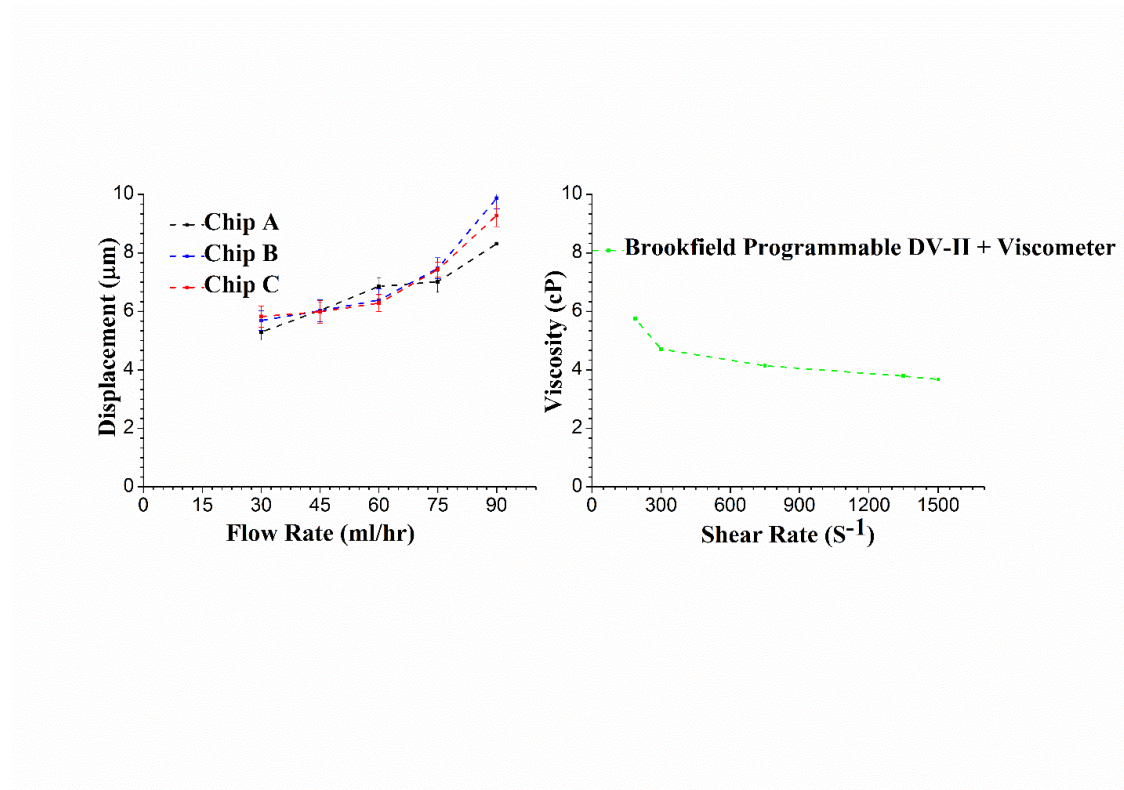


**Fig.3.12 Flow Rate vs Displacement plots for whole blood sample Chip A, B and C in comparison with Viscosity vs Shear Rate using “Brookfield Programmable DV-II + viscometer”. The displacement is increasing as the flow rate is increased.**

The measurement of viscosity using our soft cantilever viscometer depends on recording the response of these structures as flow rate is changed. We know that blood due to its shear thinning properties changes its viscosity as shear rate or flow rate in this case is changed which affects the response of the PDMS micropillars. This change in response translates into change in displacement. Fig.3.12 shows the results of the experiments that were conducted measure the viscosity of the whole blood sample.

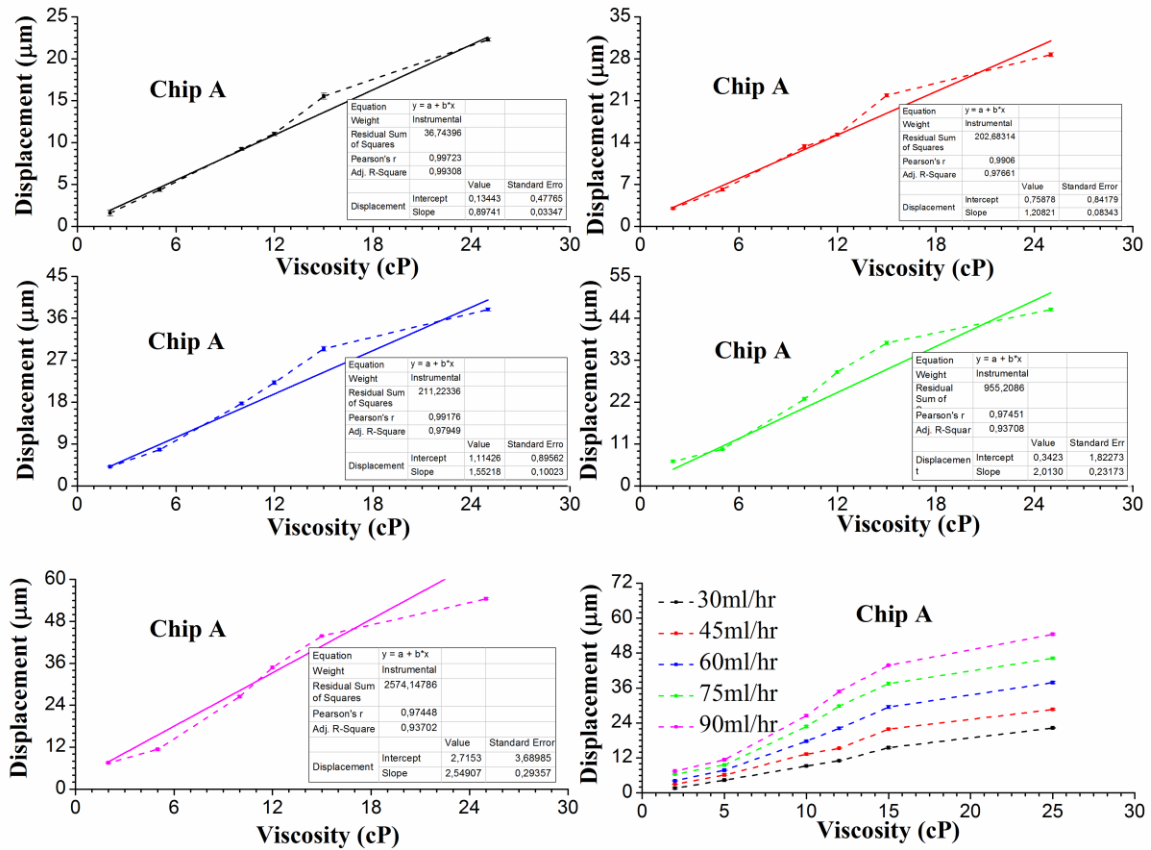


**Fig.3.13. Viscosity vs Displacement Glycerol/water (non-Newtonian) fluid plots between (5cP – 25cP) with linear fit for (30ml/hr - 90ml/hr). The slope equation  $y = a + bx$  is used to calculate the viscosity of blood by inserting the displacement  $y = 5.28 \mu\text{m}$  in the slope equation.**

The displacement values at each flow rate in Fig.3.12 correspond to a certain viscosity. By comparing these displacement values to fixed flow rate vs viscosity plot for Newtonian fluids shown in Fig. 3.13 we found the viscosity of blood at each flow rate. It can be seen from the results depicted in Fig.11 that when blood is infused into viscometer at a flow rate of 30 ml/hr it corresponds to displacement of 5.28  $\mu\text{m}$ . If we compare this with displacement value to viscosity vs displacement graph at 30ml/hr and insert the displacement in the equation  $y = a + bx$  where “y” is displacement, “b” is the slope of the fitting line and “a” is the intercept. The viscosity by putting  $y = 5.28 \mu\text{m}$  turns out to be 5.74 cP. In order to calculate viscosity at each flow rate (30ml/hr -45ml/hr) a linear fit equation was used and the results are shown in table T2.

<b>Flow Rate (ml/hr)</b>	30	45	60	75	90
<b>Displacement Measured (<math>\mu\text{m}</math>)</b>	5.28	6.037	6.8534	7.014	8.317
<b>Viscosity Calculated (cP)</b>	5.74	4.36	3.6974	3.314	2.19

**Table T2. Calculated Blood Viscosity using linear fitting equation**

In order to have an in depth understanding of microfluidic viscometer performance the calculated viscosity was plotted versus shear rate. Each flow rate in the experiment corresponds to a shear rate value. The results of this comparison are shown Fig 3.14. Brookfield commercial viscometer is a rotational viscometer where rotation of a spindle



at a fixed rpm is used to measure the viscosity of the fluid. The measurement depends on calculation of shear rate using the rpm.

The minimum shear rate that can be applied using Brookfield viscometer is  $187 \text{ s}^{-1}$  and the minimum shear rate that can be applied using microfluidic viscometer is  $77 \text{ s}^{-1}$ . It can be seen that microfluidic viscometer predicts a viscosity of  $3.31 \text{ cP}$  at  $191 \text{ s}^{-1}$  in comparison to Brookfield viscometer which predicts a viscosity of  $5.76 \text{ cP}$  at  $187 \text{ s}^{-1}$ . The reason of this discrepancy is attributed to the fact that actual shear rate in our microfluidic viscometer device is not properly calculated and we rely on CFD simulations for these shear rate values.

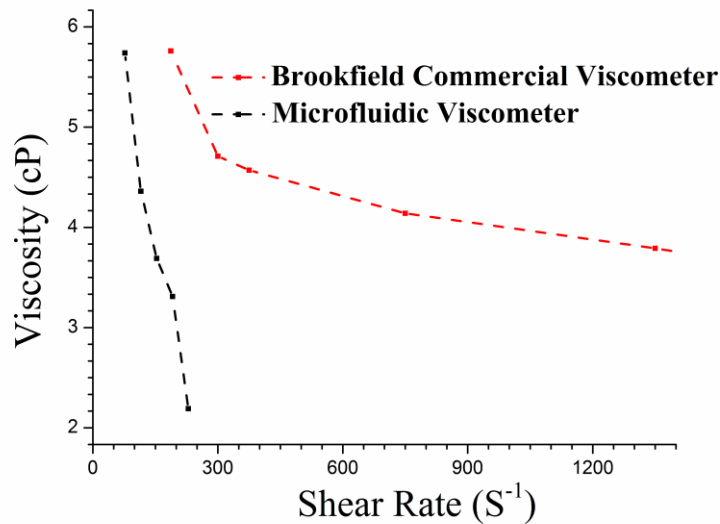


**Fig.3.14 Viscosity Vs Shear rate. Red scatter plot represents Brookfield commercial viscometer result with a minimum shear rate of  $187 \text{ s}^{-1}$  and Black scatter plot shows the microfluidic viscometer measured viscosity with a minimum shear rate of  $77 \text{ s}^{-1}$ .**

### **3.8 Precision of Microfluidic Viscometer**

In order to have better understanding of precision of our microfluidic viscometer viscosity vs average standard deviation plots were generated. These plots also revealed the precision of our device for various viscosity ranges. The results are shown in Fig. 3.15.

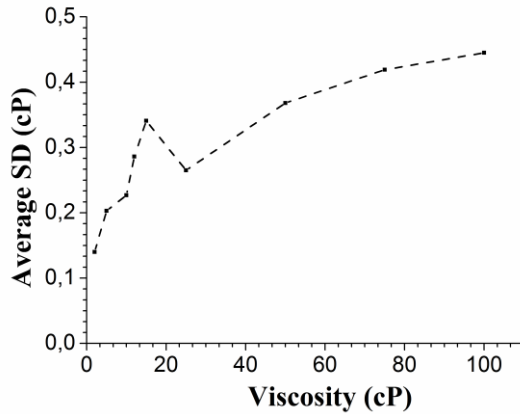


**Fig.3.15 Viscosity Vs Shear rate. The average standard deviation (SD) is calculated for 3 experiments at each viscosity at four different flow rates (15ml/hr, 30ml/hr, 45ml/hr and 60ml/hr).**

It can be seen from the results that SD increases with an increase in viscosity. The SD value for viscosity values between 2cP and 10cP is between 0.1 and 0.2 but for viscosity values between 25cP and 100cP the SD is between 0.3cP and 0.45cP. This shows that microfluidic viscometer has more precision at lower viscosity values and lower precision at higher viscosity values.

# **CHAPTER 4.**

## **BLOOD COAGULATION STUDIES USING MICROPILLAR ARRAY**

### **4.1 Introduction**

Whole blood changes during coagulation from a liquid to a solid gel. This change in blood physiology is reflected by changes in blood viscosity. Ranucci et al.<sup>12</sup>.reported that measuring viscosity during the coagulation process can give useful parameters such as clotting time (CT), maximum clot firmness (MCF) and maximum lysis (ML). They performed their studies using a commercial cone on plate viscometer. Taparia et al.<sup>32</sup> measured platelet dysfunction using microfluidic device containing an array of micro posts. Ting et al.<sup>33</sup> also presented results on platelet aggregation and contractility under shear using micro pillars in a microfluidic channel. In this section we will briefly discuss and report our studies in analyzing blood coagulation process using our micropillar based viscometer. The time dependent changes in viscosity of blood as discussed above can give an interesting insight into to clot formation and overall coagulation pathway. The coagulation pathway studies are of eminent importance for patients with bleeding disorders, Cardiac arrests and trauma surgeries. ROTEM (Rotational thromboelastometry) is currently used commercially for these studies. <sup>64</sup>

We have based our idea on the fact that as blood changes its viscosity over time during the coagulation process the displacement of micropillars will be changed. The blood changes its viscosity from a liquid to a gel like fluid which shows an increase in viscosity. This increase in viscosity can be detected with an increase in displacement of micro pillars.

## 4.2 Calibrating Microfabricated devices

The coagulation studies were performed with devices obtained from both micromachined aluminum mold and micro fabricated processes. In this section we will discuss the calibration experiments that were performed using micro fabricated chips and also compare the results of two different geometrical shapes (circular and square) as shown in Fig. 2.4 (a) and (b) of the fabricated micropillars. Initially the experiments were performed with 1cP (DI water) and 5cP glycerol/water solutions using both the devices to see the difference between the response of both devices. The results are shown Fig. 4.1 and 4.2.

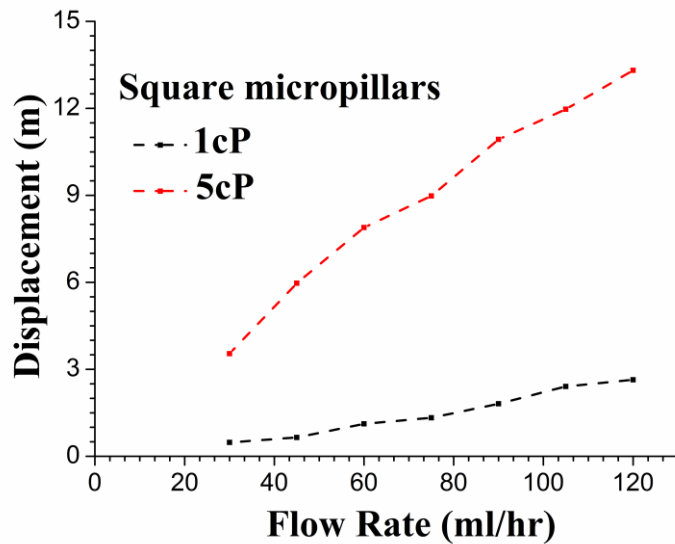


**Fig.4.1. flow rate vs Displacement Glycerol/water (Newtonian) fluid plots for (1cP – 5cP) for square shaped micropillars.**

As discussed above the response of these soft cantilevers depends on the fluid structure interaction. It can be seen from the results shown in Fig.4.1 and Fig.4.2 that square shaped micropillars have more bending for the same viscosity solution and at same flow rate.

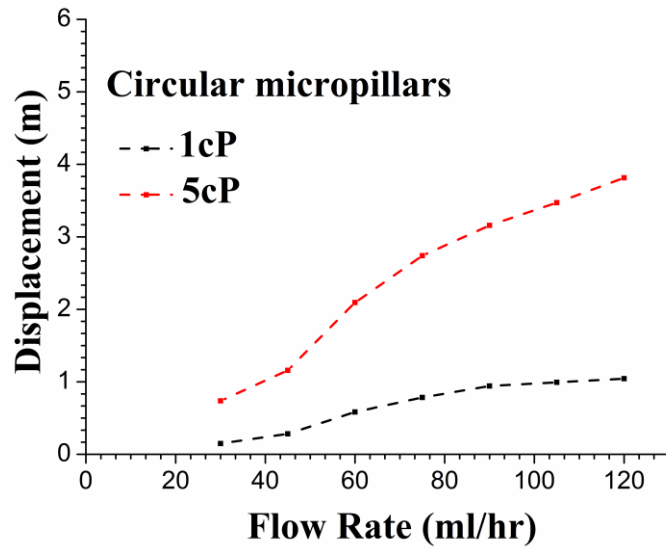


**Fig.4.2. flow rate vs Displacement Glycerol/water (Newtonian) fluid plots for (1cP – 5cP) for circular shaped micropillars.**

This observation that square shaped micropillars due to their shape and structure have more fluid-structure interaction and bend more was further enhanced by CFD analysis of both the geometrical shapes under similar boundary conditions. The results are shown in Fig 4.3 and 4.4.

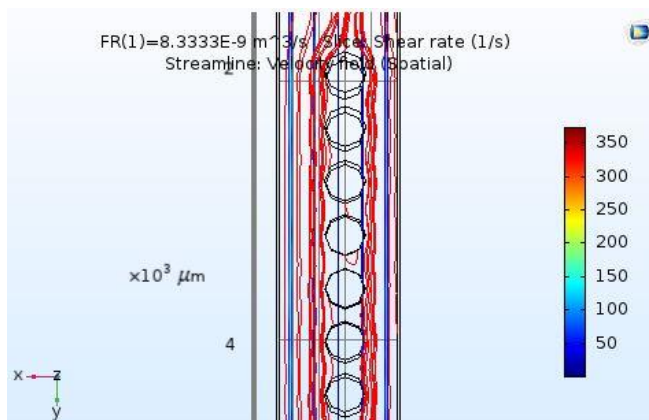


**Fig.4.3. Circular micropillars total shear rate in channel 350 S<sup>-1</sup> at 15ml/hr.**

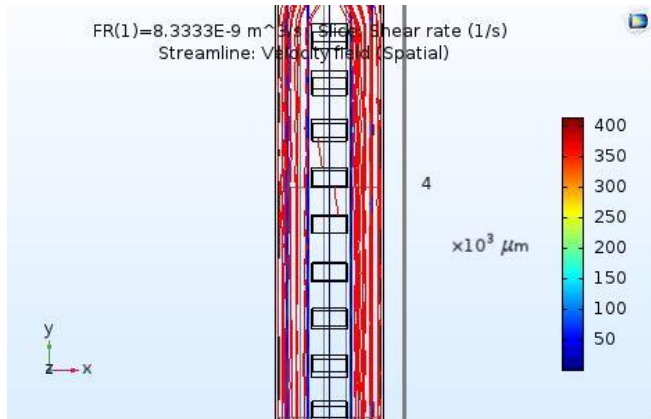


**Fig.4.4. Square micropillars total shear rate in channel 350 S<sup>-1</sup> at 15ml/hr.**

It can be seen that the amount of shear rate in channel with square shaped micropillars is 400 s<sup>-1</sup> when flow rate is 15ml/hr and under same flow conditions the total shear rate in channel with circular microchannels is 350 s<sup>-1</sup>. To have a better understanding of the experimental results flow rate vs displacement CFD studies were performed for the geometries shown in Fig. 4.3 and 4.4.

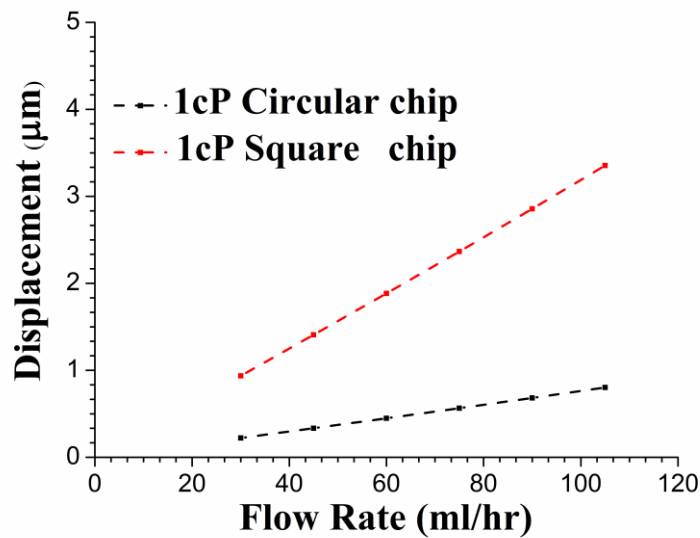


**Fig.4.5. Flow rate Vs Displacement 1cP circular chip vs square chip.**

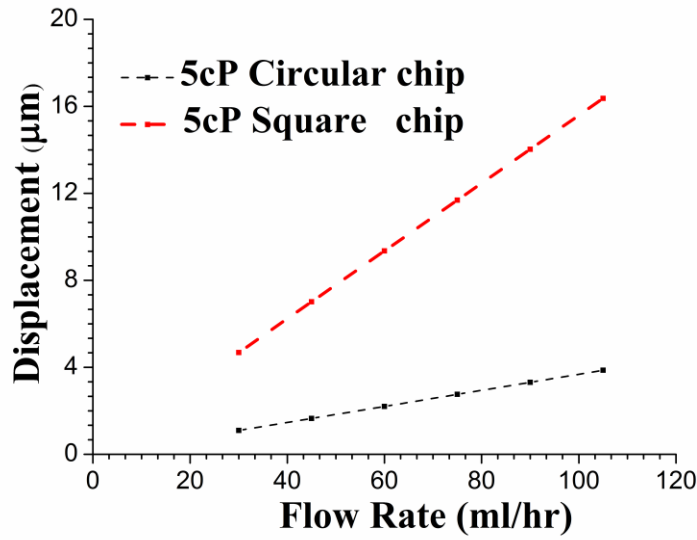


**Fig.4.6. Flow rate Vs Displacement 1cP circular chip vs square chip.**

The results depicted in Fig.4.6 and 4.7 further validate the experimental observation that due to enhanced fluid-structure interaction the device with square shaped micropillars has more bending in comparison to circular pillars under same fluid flow conditions.

### **4.3 Blood coagulation studies**

As discussed in the introductory section of the chapter that we have based our idea on the fact that as blood changes its viscosity over time during the coagulation process the displacement of micropillars will be changed and this change in displacement will be reflected in the displacement of soft cantilevers. The first experiments were performed using micropillar device obtained from micromachined aluminum mold. Whole blood was used and  $\text{CaCl}_2$  was used as coagulation promoter. Blood was infused and withdraw for an interval of 15 seconds at a flow rate of 15nl/hr. The infusion and withdraw cycle at a fixed flow rate of 15ml/hr made sure that change in amplitude of displacement of micropillars

was due to variation of viscosity of blood during coagulation process.<sup>65,66,67</sup> Fig. 4.8 (a), (b), (c) and (d) show different stages of coagulation process.

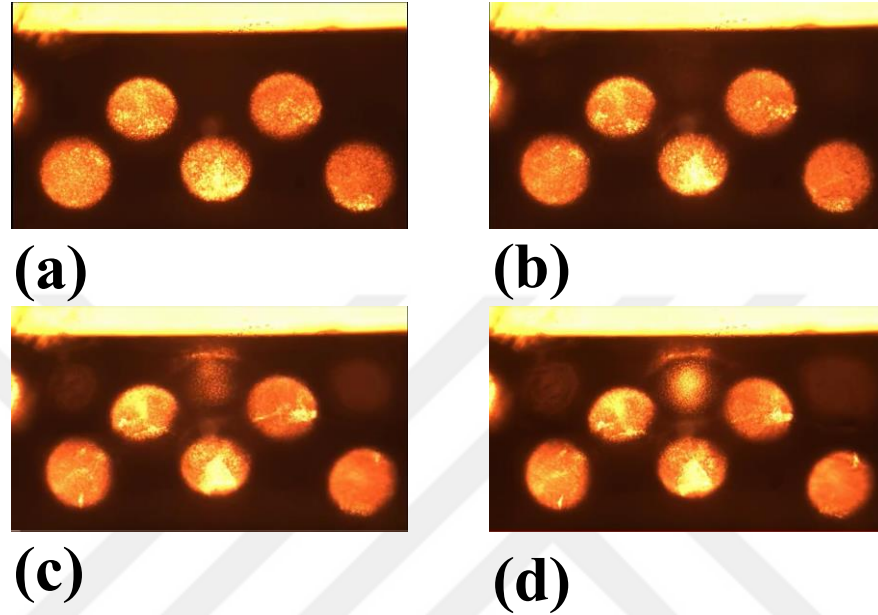


**Fig. 4.7 (a) Infusion of blood into device (b) coagulation initiating (c) clots forming around micropillars (d) fully formed clot around micropillars**

The videos recorded were processed and time vs displacement plot was generated as shown in Fig.4.9. It can be seen that at the start of the experiment when there is no flow (syringe pump) is off the micropillars are at rest hence the displacement is zero. Once the infusion starts the displacement starts to increase.  $\text{CaCl}_2$  induces the coagulation and the viscosity of the blood starts to increase clearly depicted by an increase in displacement.

It was observed that once the blood is fully coagulated that is we have full clot formation around the micropillars the displacement of micropillars practically becomes negligible. This was also depicted by the results shown in Fig. 4.8.



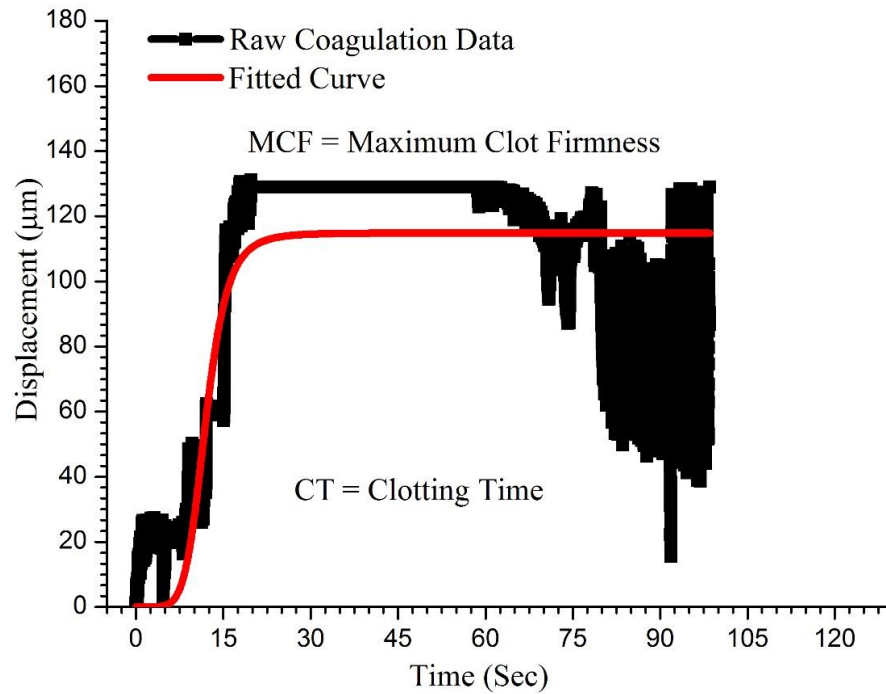


**Fig.4.8. Displacement vs Time plot for coagulation experiment depicting different stages of blood coagulation process.**

Similarly, Microfabricated chips were also employed for blood coagulation studies. In order to compare the performance of our device with the commercially used ROTEM device three of the standard tests namely Intem, Extem and Fibtem were performed. Each of these tests give an important insight into coagulation process.<sup>68</sup> Extem is known as extrinsic screening test and activates the coagulation using tissue thromboplastin which initiates the clot formation in about 70 seconds. This allows to study and assess the clot formation within 10 minutes.<sup>69</sup>. Intem on the other hand is known as intrinsic screening test and coagulation is activated using a contact phase and coagulation is effected by presence of heparin in the tubes. Fibtem has a similar coagulation activation process that

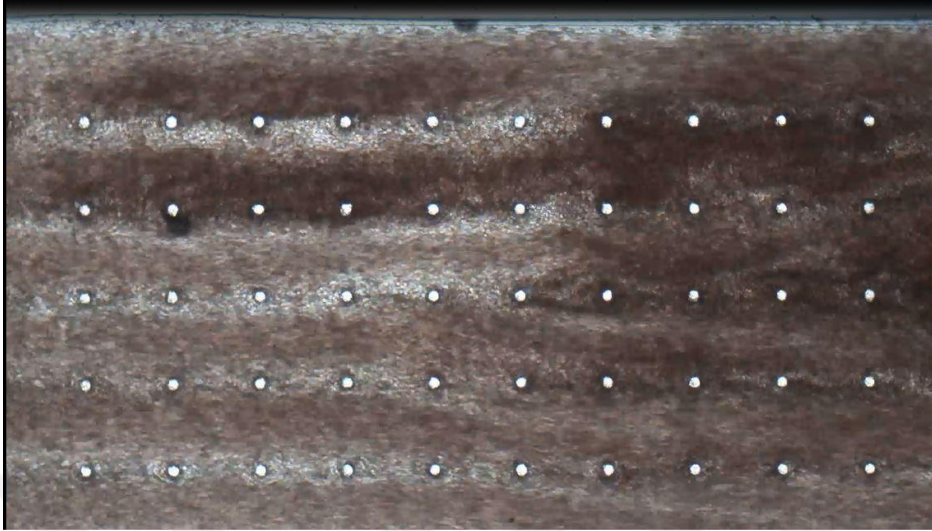
is the coagulation is activated by the addition of cytochalasin D. The clot formation mostly depends on fibrin formation and polymerization.<sup>69</sup>

The experiments were designed in a way that 340  $\mu\text{l}$  of blood was mixed 10  $\mu\text{l}$  of startem and 20  $\mu\text{l}$  of the test solution that is Extem, Intem or Fibtem. 150  $\mu\text{l}$  of the mixed solution was then taken in micropipet tip and inserted at the outlet of the microfluidic device. The inlet of the device was attached to syringe containing Phosphate buffered saline (PBS) which acts as anticoagulant so that there is no blood clot at the tip of the infusion tube. As was the case for viscometry experiments it was imperative to have no bubbles inside the channel during experiments.

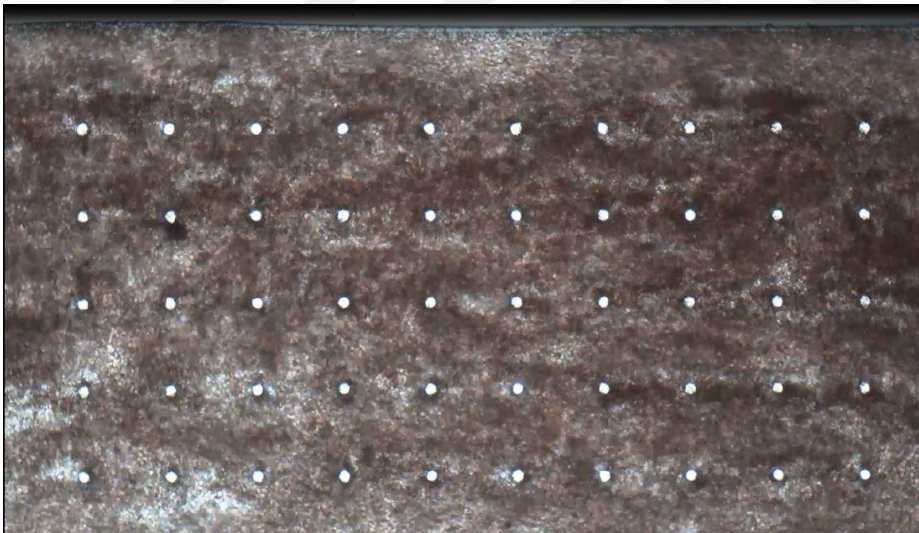
The infusion/withdraw cycle was setup at 15ml/hr with 8  $\mu\text{l}$  solution volume being infused and withdraw. The figures 4.9 (a) and (b) show different stages of coagulation process in microfabricated devices.



**Figures 4.9 (a) Blood infusion/withdraw in channel at 15ml/hr**

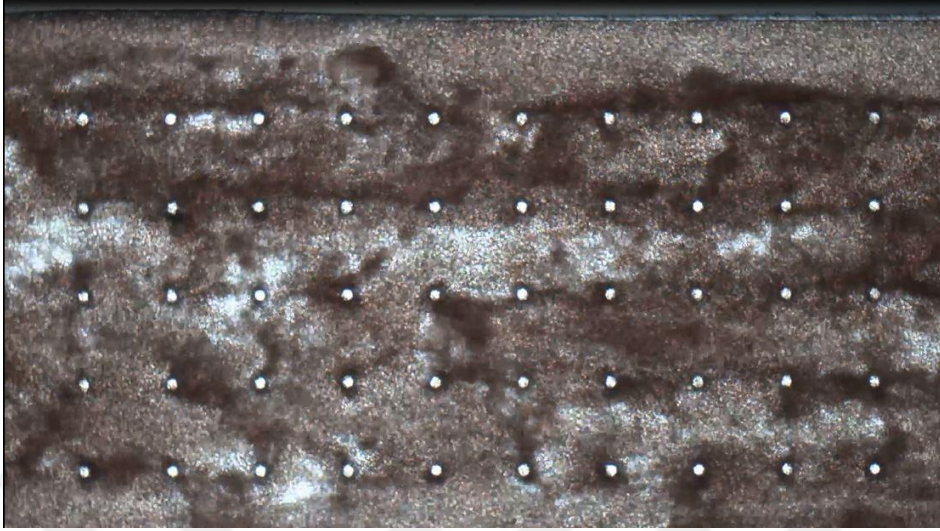


**Figures 4.9 (b) Coagulation/clot formation starts and is visible right side of the channel.**



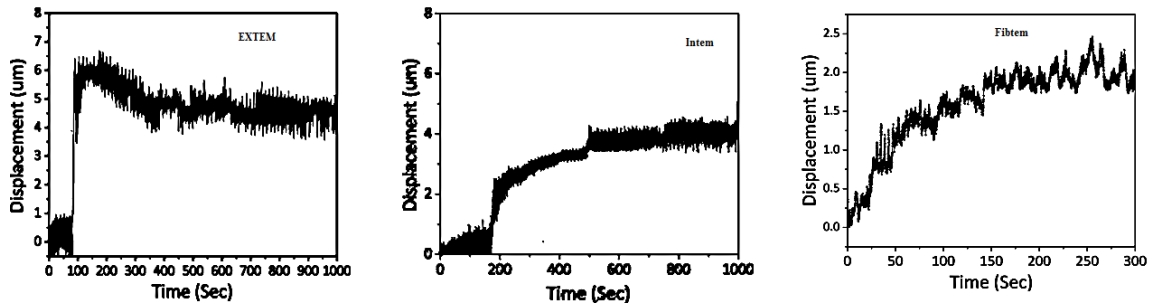
**Figures 4.9 (c) Homogeneous coagulation/clot formation throughout the channel.**





**Figures.4.9 (d) Clots fully formed around the micropillars and it was observed visually during the experiments.**

The recorder videos were analyzed and the Fig. 4.11 depicts results of Extem, Intem and Fibtetm experiments.



**Figures.4.10 Extem, Intem and Fibtetm tests using microfabricated micropillar device.**

It can be seen from the results shown in Fig.4.10 that as the viscosity of the blood changes over time the displacement also changes. The increase in displacement is due to an increase in the viscosity of blood as it changes from water like liquid to gel like liquid. The coagulation pathway parameters such CT, CFT and MCF can be extracted from the results shown above by carefully derivating displacement over time.

## **CHAPTER 5.**

### **COMPUTATIONAL FLUID DYNAMIC STUDIES**

#### **5.1 Introduction**

In recent years CFD studies have proven to be critical in designing microfluidic systems. In order to verify the design and experimental parameters employed for the viscometer device presented in this dissertation “COMSOL” Multiphysics CFD tool was used. Two different viscometer device designs were simulated and the results obtained were compared with the experimental data.

#### **5.2 Simulation design parameters**

The simulation was designed in a way that boundary conditions chosen are a reflection of experimental conditions. Laminar flow and solid mechanics modules were used where “laminar flow” was used to input flow rates values and solid mechanics was used to measure the response of micropillars as fluid interacts with them. The “laminar flow” and “solid mechanics” were coupled with each other by using “Multiphysics module”.

The micropillars are in essence cantilevers with a fixed end so fixed constraint boundary condition was used in solid mechanics module as shown in Fig 5.1. Laminar inflow was used as the inlet boundary condition and flow rate chosen as the input parameter to have the desired similarity with the experiments. Another important parameter in microfluidic channels is the length required by the fluid flow to stabilize known as  $L_{ent}$ . It was calculated to be  $L_{ent} = 0.304$  m.

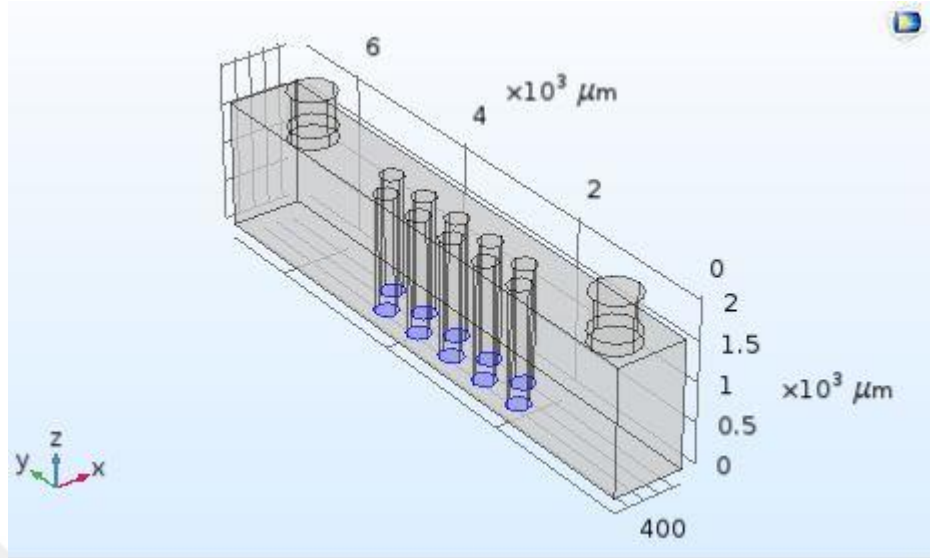


**Fig 5.1 Micropillars with fixed constraint boundary condition.**

### **5.3 Viscometer device with straight micropillar array**

The microfluidic viscometer presented in this dissertation as discussed previously is based on measuring the response soft cantilevers (micropillars). The micropillar response depends upon the interaction of fluid flowing through the channel. Hence, the goal was to maximize the fluid structure interaction. Initially the device was designed to have a straight array of micropillars. The length of microfluidic channel was  $Ch_L = 7000 \mu m$  and channel width  $Ch_w = 900 \mu m$ . The micropillar height was  $H = 1500 \mu m$  and diameter  $= 300 \mu m$  which gives an aspect ratio of 1:5 as shown in Fig 5.2. It has been reported previously in literature that micropillars with higher aspect ratio tend to be more sensitive sensors for the same amount of input force.<sup>70</sup>

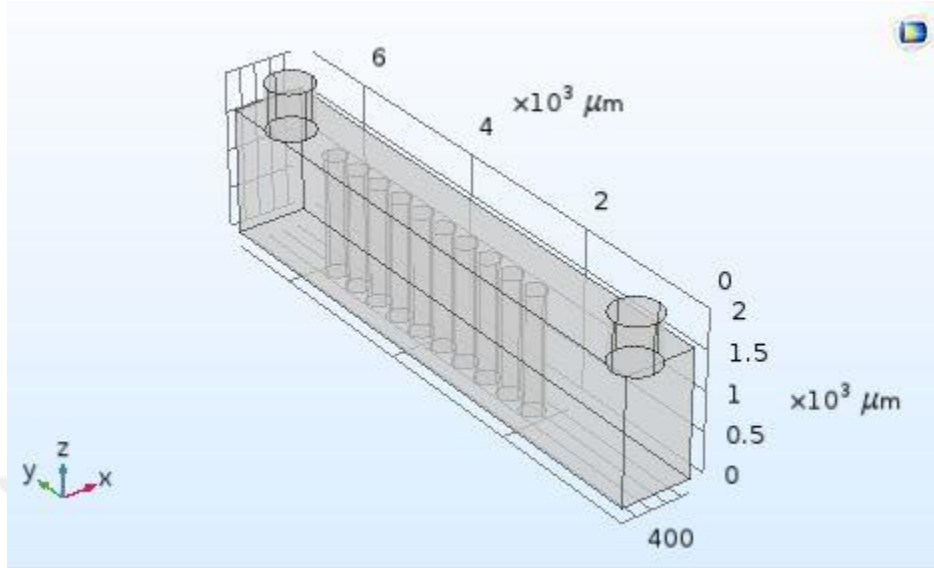


**Fig 5.2 Microfluidic viscometer straight micropillar array with channel height ( $H = 1600 \mu\text{m}$ ) and width ( $W = 900 \mu\text{m}$ ).**

It was noted that in the device shown in Fig 5.2 the fluid structure interaction was minimum and maximum amount of fluid passed along side walls as shown in Fig 5.4 depicting the stream lines as the fluid flows through the channel. This observation was further validated by comparing pressure contour plots for both microfluidic viscometer designs. The pressure contour plot for the device with straight array of micropillars is shown Fig 5.3. The maximum pressure is at the inlet of the channel as fluid enters the device and it is  $156.24 \text{ Pa}$  for the flow rate of  $4.1 \times 10^{-9} \text{ m}^3/\text{s}$  ( $15 \text{ ml/hr}$ ).

In comparison the pressure at the inlet of microfluidic viscometer device with alternating micropillar array which will be discussed in next section two times more than noted for the first design. The reason for this difference is attributed to the fact that alternating micropillar array maximizes the fluid structure interactions.

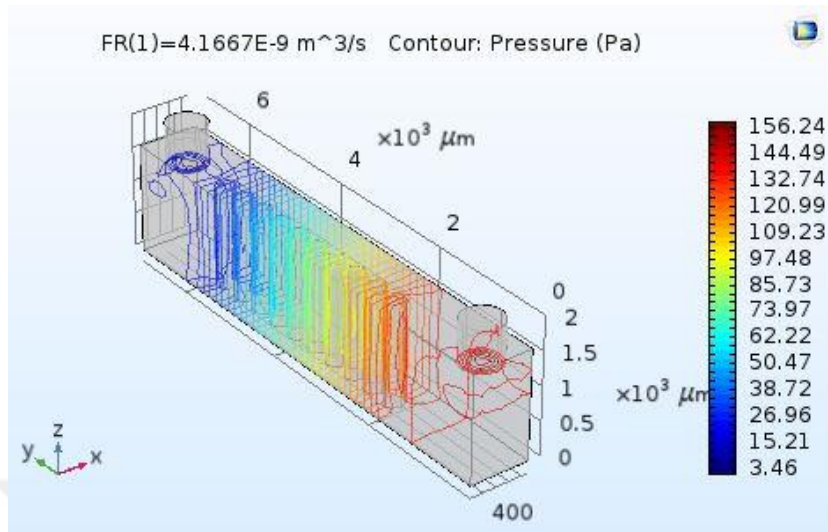


**Fig 5.3 Microfluidic viscometer with straight micropillar array pressure contour plot (flow rate = 15ml/hr).**

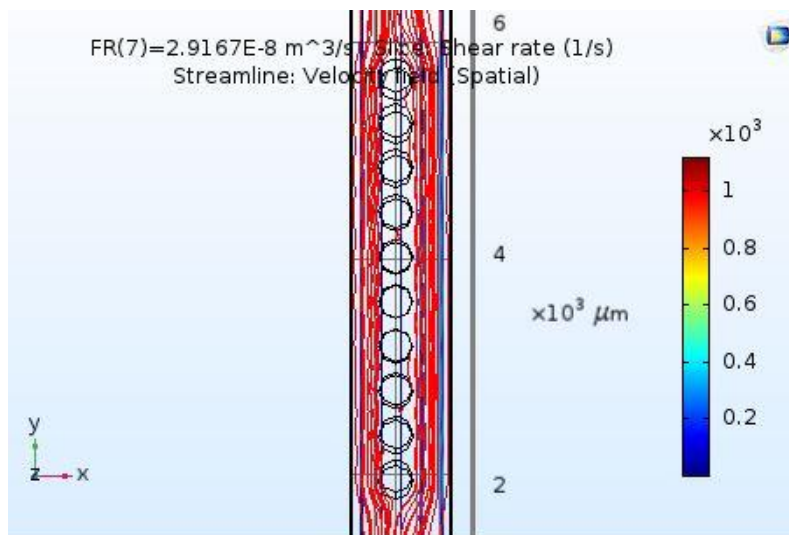


**Fig 5.4 Microfluidic viscometer straight micropillar array streamlines. The streamlines are denser near the side walls depicting that most of the fluid passes along the sidewalls.**



The CFD study was for a flow rate range of (15ml/hr – 105ml/hr) and for viscosity ranging from (5cP – 50cP). The Young's modulus for PDMS was kept to be  $E = 1.8 \text{ Mpa}$  in comparison with modulus of elasticity value of the fabricated devices. Flow rate vs displacement plots were generated as shown in Fig.5.5.

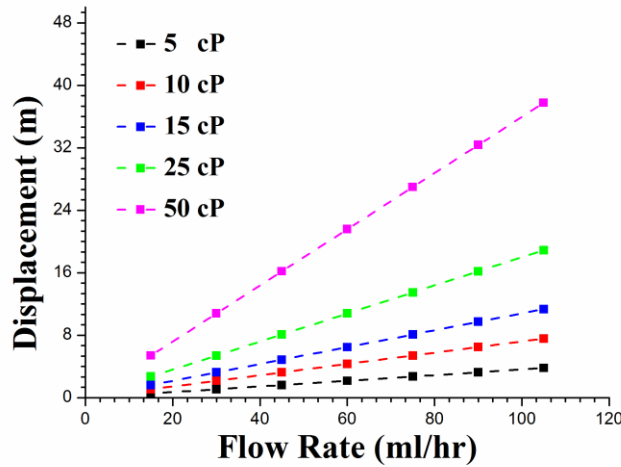


**Fig.5.5 Flow rate vs Displacement plot for microchannel with straight micropillar array. Viscosity range (5cP – 50cP and flow rate range (15ml/hr – 105ml/hr).**

#### 5.4 Viscometer device with alternating micropillar array

It can be seen from the results shown in Fig. 5.4 that in order to maximize the fluid – structure interaction the design of the viscometer device needs to be modified. The design was modified by creating a zig-zag shaped array hence the name alternating micropillar array viscometer. The channel height and channel length remained the same as the straight micropillar array device. The design of the device is shown in Fig 5.6.

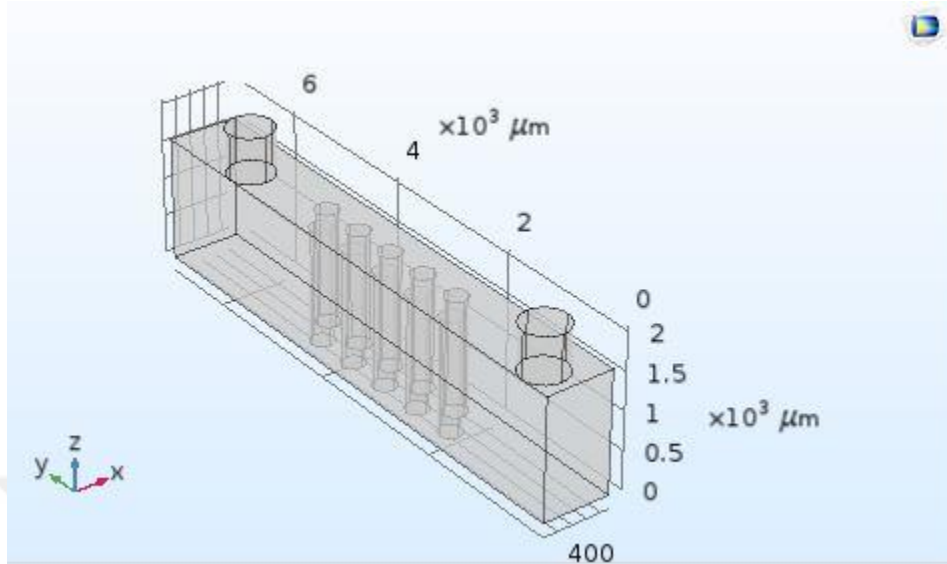


**Fig 5.6. Alternating micropillar array viscometer device with channel height ( $H = 1600 \mu\text{m}$ ) and width ( $W = 900 \mu\text{m}$ ).**

By choosing a zig-zag arrangement of micropillars the distance from micropillar base to side wall from one was reduced to  $150 \mu\text{m}$  in comparison to previous design where the array of pillar was in center of the channel so the distance from the side walls from either side of the channel was  $300 \mu\text{m}$ .

The advantage of choosing such an arrangement was that most of the fluid entering the channel interacted with the micropillars hence a much more sensitive response to the applied force. This hypothesis is vindicated by the results shown in Fig.5.7. It can be seen that streamlines are evenly distributed along the sidewalls and through the center of the micropillar array an indication of the increased micropillar-fluid interaction.

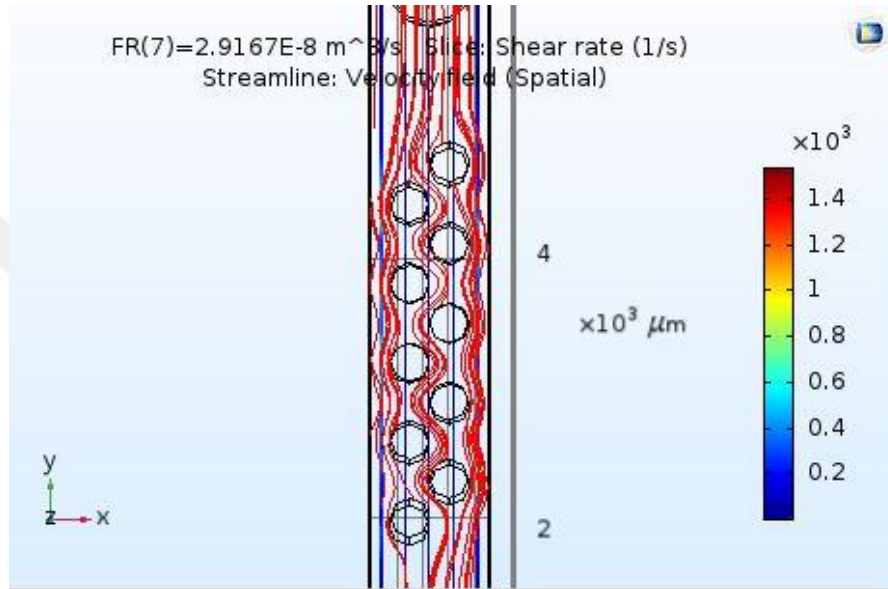


**Fig.5.7. Microfluidic viscometer alternating micropillar array streamlines. The stream lines are evenly distributed along the side walls and through the center of the array depicting increased fluid interaction with micropillar structures.**

The pressure contour plot for the pressure at the inlet at  $4.1 \times 10^{-9} \text{ m}^3/\text{s}$  (15ml/hr) also vindicated this observation. The result is shown in Fig 5.8 and it can be seen that in this case the pressure at the inlet is 384.32 Pa.

A comparison flow rate vs displacement plot was generated to have an in depth understanding of how the change in device design effected the micropillar response. It can be seen from results shown in Fig.5.9 that viscometer device with alternating array design

is more sensitive and has more displacement for the same amount of force (flow rate) applied.

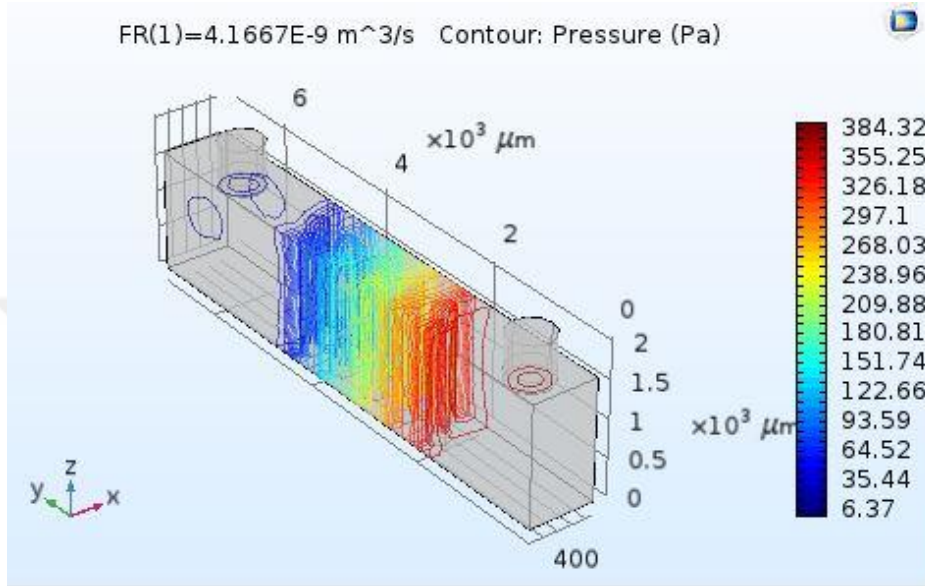


**Fig.5.8. Microfluidic viscometer with alternate channel micropillar array pressure contour plot (flow rate = 15ml/hr).**

In next section the simulation results for alternating micropillar array will be compared to experimental results of the fabricated device. A good fit was observed between the experimental and simulation results at lower viscosities. The Young's modulus commonly known as modulus of elasticity was chosen to be  $E = 1.8 \text{ Mpa}$  for all the simulations to match the modulus of elasticity of fabricated device.

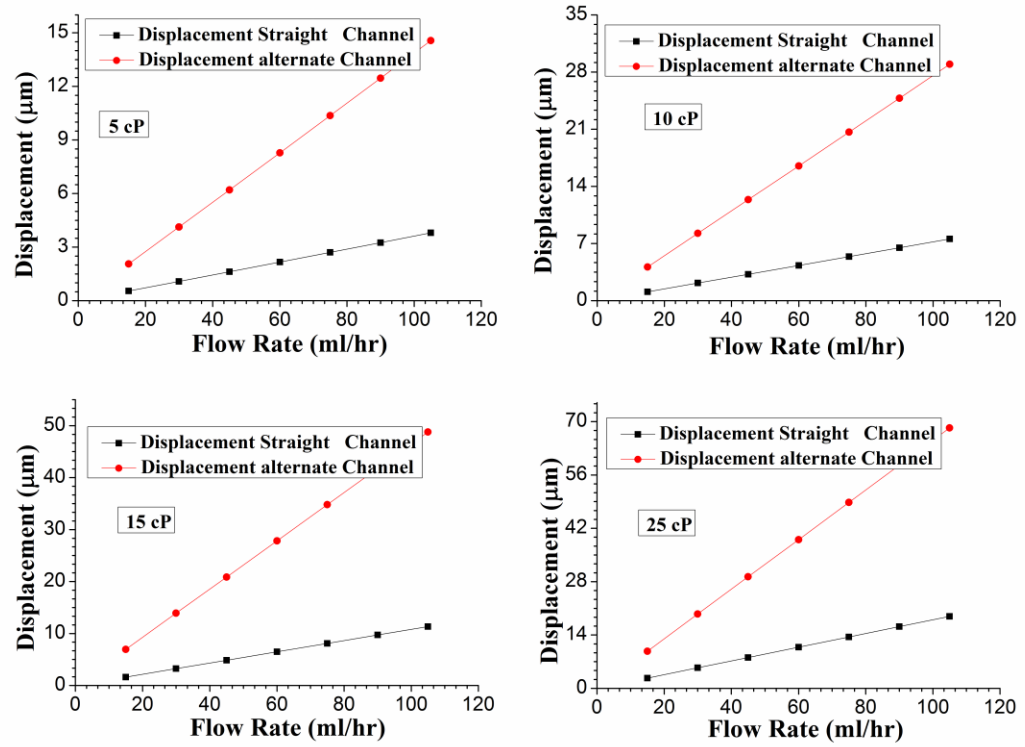


**Fig.5.9. Microfluidic viscometer alternating micropillar array vs straight micropillar array. Flow rate range (15ml/hr – 105 ml/hr).**

### 5.5 Comparison simulation studies vs experimental data

In order to have an understanding of how good simulations predicted the device performance the simulation results were compared to experimental results. As the alternating micropillar device was chosen to be the final device design so the results shown in Fig 5.10 are a comparison between the results of simulation of alternating microchannel and the experiments.

The data fits well for lower viscosities but for higher viscosities the experimental data has a non-linear trend the reason for that is the non-linearity of PDMS Young's modulus explained in detail in chapters 03 and 04.

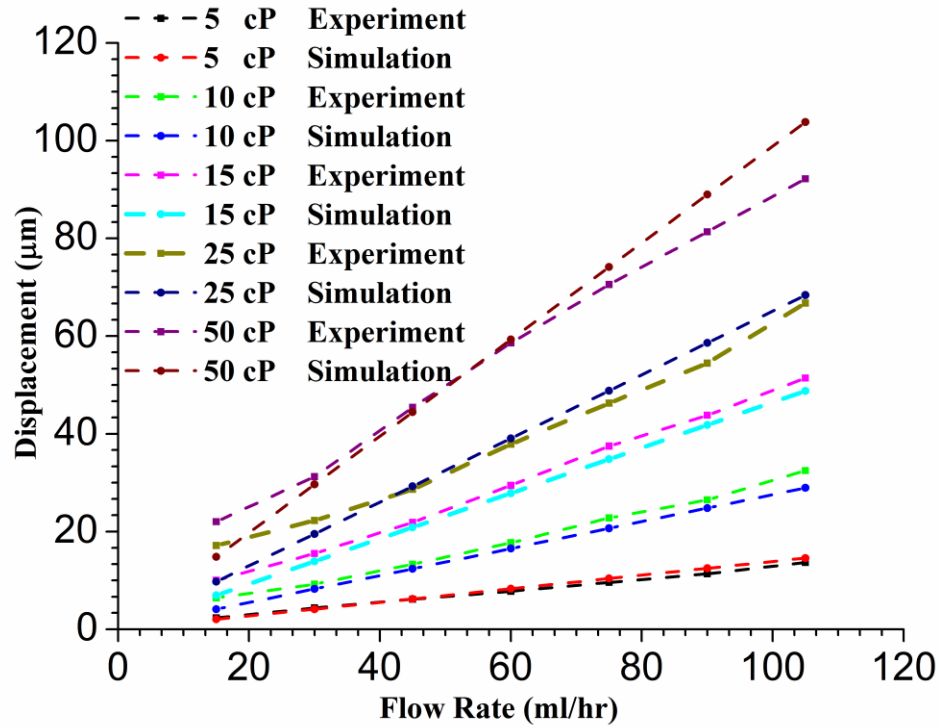


**Fig 5.10 Microfluidic viscometer alternating micropillar array simulation vs experimental data. Flow rate range (15ml/hr – 105 ml/hr).**

## 5.6 Conclusion

In conclusion we can confer that for the microfluidic viscometer device presented in this dissertation it is imperative to maximize the fluid-structure interaction to have an increased sensitivity.

## **CHAPTER 6.**

### **DISSOLUTION OF MICRODROPLETS**

#### **6.1 Introduction**

The dissolution of liquid microdroplets is of great importance in many industrial processes with applications ranging from food industry (separation and dispersion) to pharmaceutical industry (drug delivery/design).<sup>71,72,73</sup>. In particular, dissolution is one of the key quality control tests widely used in pharmaceutical industry.

The dissolution rate depends on solubility of oil in water. Oil microdroplets with low solubilities are considered immiscible in water. The miscibility or solubility of these oil components in water can be enhanced by the introduction of flow. This part of dissertation will be focused on experiments that were designed to verify that dissolution/solubility of so called immiscible oil microdroplets can be enhanced in an immiscible aqueous phase (water) as flow is introduced.

Early work by Epstein and Plesset modeled the diffusion-based dissolution of gas microbubbles in a host liquid.<sup>74</sup>. Using a micropipette manipulation technique, Duncan and Needham experimentally verified Epstein-Plesset (EP) model with single component gas bubbles.<sup>75</sup>. Micropipet manipulation was also used to verify the validity of the EP model for single component aniline oil droplets in water <sup>76</sup> and to study the dissolution of multicomponent protein-water microdroplets in water.<sup>76</sup>. Recently, the same technique, through a modified form of the EP equation, was used to model the dissolution of

microdroplets obtained by a two-component mixture of mutually miscible oils (ethyl acetate, butyl acetate, and amyl acetate) into a second immiscible phase (water).<sup>77</sup>.

For liquid microdroplets with extremely low solubilities in the host liquid, experiments that rely on the diffusion-based EP equation can prove to be impractical because of the extended experimental times. For such cases, it is preferable to speed up microdroplet dissolution by incorporating flow into the experiment.

In this article, we exploit a novel experimental method, where microdroplets experience extensional creeping flow as they are hydrodynamically trapped. Hydrodynamic trapping is a microfluidic trapping technique where particles are trapped at a stagnation point generated at the junction of two perpendicular microchannels. Recently, hydrodynamic trapping has been introduced as a powerful tool for trapping and manipulation of microbeads, DNA molecules, and cells in microfluidic chips.<sup>29,78,30</sup>. The fabrication and trapping mechanism will be discussed in detail in next chapter.

In order to incorporate the effects of convection due to motion of the host liquid in which the droplet is dissolving, the convection-diffusion equation needs to be solved. Kurdyumov and Polyanin studied the effects of convection on drop dissolution in a shear flow.<sup>79</sup>. They used the known analytical solution for the velocity field at small Reynolds number and numerically solved the advection-diffusion equation for the mass transfer for a wide range of Péclet numbers. Péclet number signifies the relative importance of convection compared to diffusion, and is defined as  $Pe = UR/D$  where “U, R, and D” are the free stream velocity,



droplet radius, and diffusion coefficient for the droplet liquid in the host fluid. On the basis of their numerical results and the analytical solutions in the limiting cases of very low and very high  $Pe$ , they derived a correction relating the Sherwood number to  $Pe$ . Sherwood number represents the ratio of the total rate of mass transfer to the rate of purely diffusive mass transport in the absence of convection, and is defined as  $Sh = KR/D$ , where  $K$  is the mass transfer coefficient. This work has been recently extended to the case of extensional creeping flow through extensive numerical simulations by Zhang-Yang-Mao.<sup>80</sup>

In this dissertation, for the first time a novel, noncontact technique based on hydrodynamic trapping is used to study the dissolution of freely suspended benzyl benzoate (BB) and *n*-decanol microdroplets in water. Unlike the micropipette manipulation technique, no mechanical contact is required for trapping of the microdroplets. The studied microdroplets are prepared by vigorous agitation of a solution containing AOT (docusate sodium salt) surfactant at concentrations of 10  $\mu$ M or 10 mM. Experimental results are compared with the numerical study by ZYM, and good agreements are obtained. Experiments also reveal an enhancement in the dissolution rate of microdroplets due to micellar solubilization when surfactant concentration is increased beyond the critical micelle concentration (CMC).<sup>81,82</sup>

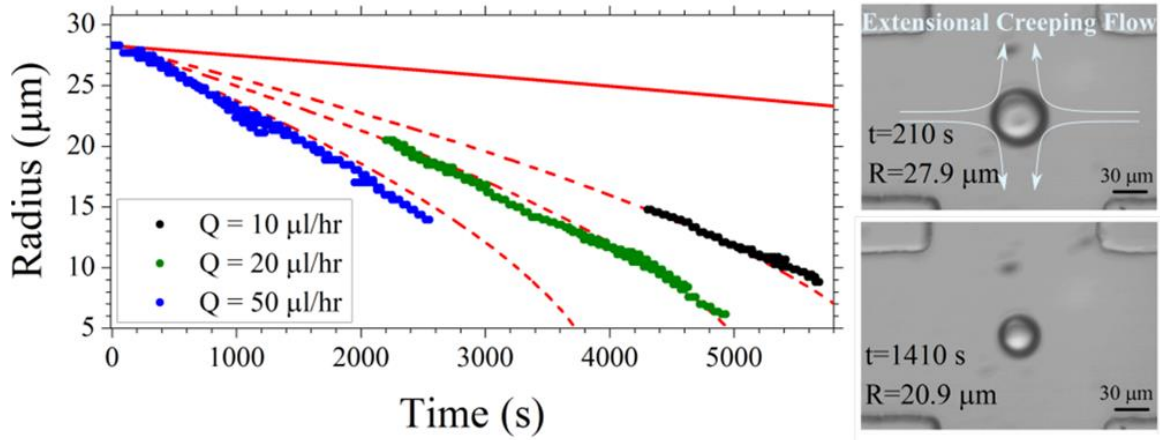


**Fig. 6.1 Dissolution of oil microdroplet at different flow rates  $T=210 \text{ s}$  and  $T=1410 \text{ s}$ .**

## 6.2 Mathematical Modelling

The experimental results are compared to the models developed by EP<sup>74</sup> and by ZYM.<sup>80</sup>. In both models, the droplet is assumed to remain spherical and dissolution does not alter the material properties of the droplet and host fluids. The EP model only considers diffusive fluxes so it is valid only for small Péclet numbers, i.e.,  $Pe \ll 1$ . The ZYM model takes both the convection and diffusion into account. These two models are briefly explained below and then used to interpret the experimental results in the following section.

## 6.3 Epstein-Plesset (EP) Model

EP model was originally derived for dissolution of single gas bubbles in an infinite domain. Recently, Duncan and Needham have shown that the EP model also applies to dissolution of single liquid droplets in the absence of convection in an infinite domain. According to

this model, the dissolution rate of the droplet that can be described as the rate of change in droplet radius ( $R$ ) with respect to time ( $t$ ), and is given as

$$\frac{dR}{dT} = - \frac{D(C_s - C_\infty)}{\rho} \left( \frac{1}{R} + \frac{1}{(\pi D t)^{1/2}} \right) \quad [6.1]$$

where  $\rho$  is the density of the droplet,  $C_s$  is the saturation concentration of the droplet liquid in the host fluid, and  $C_\infty$  is the concentration of the droplet liquid in the host fluid far away from the droplet (at infinity). Host fluid used in all the experiments reported in this paper did not contain any droplet liquid. Hence  $C_\infty$  is assumed to be 0 for all the reported calculations. This model is only valid for diffusion dominated flows, that is,  $Pe \ll 1$ . Equation 6.1 is integrated numerically using a 4th order Runge–Kutta method in the present study although EP provided an analytical solution.

#### 6.4 Zhang-Yang-Mao (ZYM) Model

Gupalo and Riazantsev<sup>83</sup> were the first to study the convective mass transfer from the surface of a solid sphere and a spherical droplet in a uniform shear flow at high Péclet numbers. They came up with analytical expressions for the mass flux in the approximation of the diffusion boundary layer and showed that  $Sh$  is proportional to  $Pe^{1/3}$  for a solid sphere and  $Pe^{1/2}$  for a liquid drop.

Later, Batchelor<sup>84</sup> derived analytical expressions for the mass transfer rate from a solid sphere suspended in a linear ambient flow field for both low and high  $Pe$ . To bridge the

gap between low and high Pe analytical solutions, Kurdyumov and Polyanin<sup>79</sup> presented numerical solutions for the mass transfer from spherical particles, drops, and bubbles in a linear creeping shear flow. They also proposed empirical correlations for Sh that fits their numerical calculations very well for  $Pe \leq 1000$ . ZYM extended this study to a simple extensional creeping flow for a wide range of Péclet numbers ( $Pe = 1$  to  $100\,000$ ). A numerical study performed by ZYM reveals the following approximate relations for Sherwood (Sh) number:

$$Sh = \frac{1}{\beta+1} \left( 0.207 Pe^{\frac{1}{2}} - 0.201 \right) + 0.467 Pe^{1/2} + 1.053 \quad [6.2]$$

$$Sh = \frac{1}{\beta+1} [0.6 + (0.16 + 0.48 Pe)^{\frac{1}{2}}] + \frac{\beta}{\beta+1} [0.5 + (0.125 + 0.745 Pe)^{1/3}] \quad [6.3]$$

Equation 6.2 and Equation 6.3 are valid for  $1 \leq Pe \leq 10$  and  $10 < Pe \leq 1000$ , respectively.  $\beta$  is the ratio of the dynamic viscosity of the droplet to that of the surrounding fluid ( $\beta = \frac{\mu_d}{\mu_s}$ ).

The mass transfer rate from the droplet into the ambient fluid is given by

$$\frac{dm}{dt} = -K(C_s - C_\infty) A_{drop} \quad [6.4]$$

$A_{drop}$  is known as the surface area of the droplet. By Substituting  $m = (4/3) \pi R^3 \rho$ ,  $A_{drop} = 4\pi R^2$ , and  $Sh = KR/D$  into Equation 6.4 we obtain

$$\frac{dR}{dt} = - \frac{D(C_s - C_\infty)}{R\rho} Sh \quad [6.5]$$

Equation 6.5 together with Equation 6.2 and Equation 6.3 model the dissolution of a microdroplet in simple extensional creeping flow for  $1 \leq Pe \leq 1000$ . This range of Péclet numbers covers all the experiments presented in this dissertation. Hence, we will use Equation 6.2, 6.3 and 6.5 to fit to all the data presented in this thesis.  $C_s$  is used as the fitting parameter since it is not a well-documented parameter of the liquids especially those with very low solubilities.

## CHAPTER 7.

### HYDRODYNAMIC CHIP FABRICATION AND EXPERIMENTAL SETUP

#### 7.1 Introduction

Isolation and trapping single particles/cells has been at the core of the microfluidics device fabrication. There have been numerous devices reported in literature for single particle/cell trapping.<sup>85,86</sup> The device used for trapping single oil microdroplets in this thesis is based on creating a stagnation point at the junction of two opposing laminar streams.<sup>30,28</sup> It's a novel non-contact trapping mechanism reported in literature by Tanyeri et al.<sup>29</sup>

The hydrodynamic device is a closed loop feedback system that uses the relative flow rates through the outlet channels as the feedback parameter for stabilizing the position of a target particle at the microchannel junction. Image analysis is used for determining the position of a target particle. The automated feedback control mechanism also enables particle manipulation along the direction of the outlet channels. The adjustment in fluidic resistance is such that equal amount of fluid flows out of both the outlets to achieve a condition ( $R_1=R_2$ ) as shown in Fig.7.1

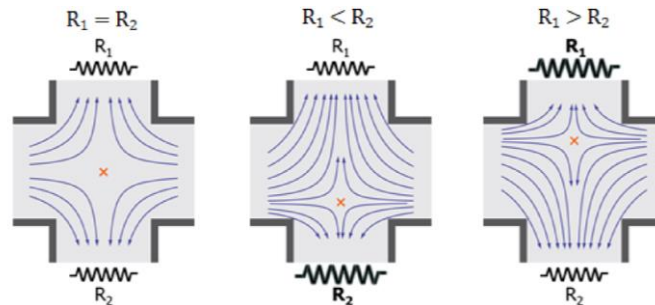


**Fig.7.1 Graphical representation of creating condition ( $R1 = R2$ ) for efficient trapping**

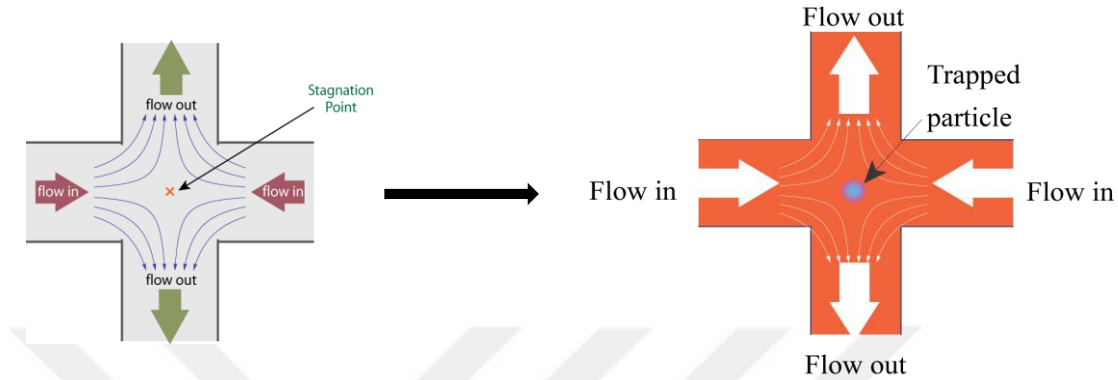


**Fig.7.2 Graphical representation of stagnation point and particle trapped at stagnation point.**

## 7.2 Device Fabrication

Hydrodynamic trapping is performed in conventional polydimethylsiloxane (PDMS) microfluidic chips fabricated by multilayer soft lithography. The two layers are known as “fluidic layer” and “control layer”. The device is fabricated in two steps. In first step a negative photoresist SU-8 2050 was spin coated on 3 inch Si wafer at 4000 RPM for 30 seconds to achieve a thickness of  $35\mu\text{m}$  for fluidic layer. The wafer was soft baked for 5 minutes at  $95^{\circ}\text{C}$ . A contact UV lithography step was performed by exposing the pre baked wafer for 40 seconds. A post exposure baking step was performed again heating 5 minutes at  $95^{\circ}\text{C}$ . The height of the structures was measured using a profiler as shown in Fig. 7.3. A second mold was prepared for control layer by spin coating SU-8 2050 at 1700 RPM on a

3 inch Si wafer for 30 seconds to achieve thickness of 100  $\mu\text{m}$ . The mold was then soft baked for 15 minutes at 95<sup>0</sup>C and exposed to UV using contact printing for 40 seconds.

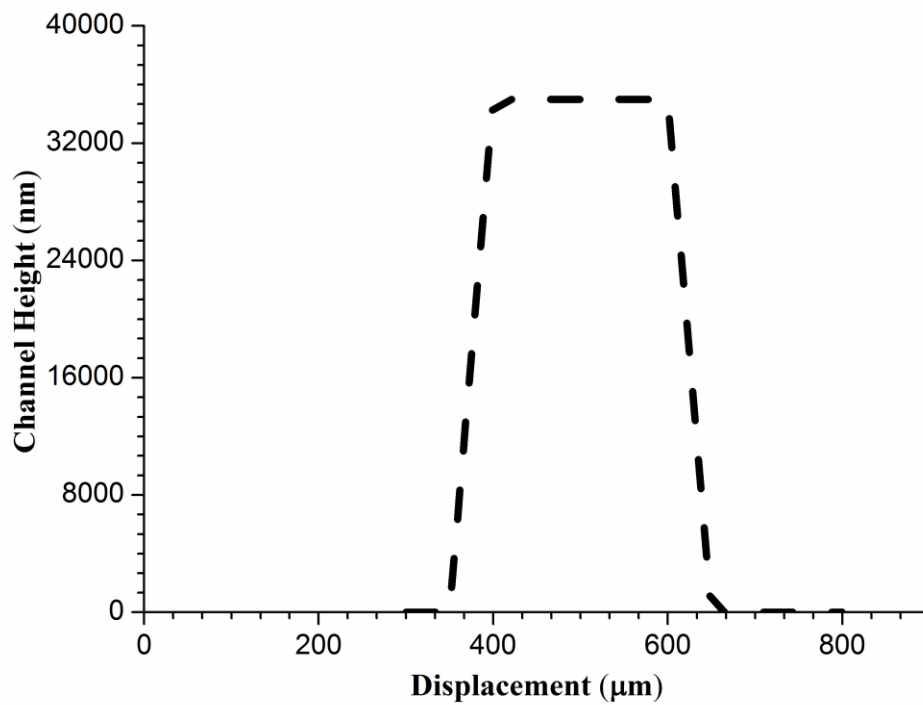


**Fig.7.3 Fluidic channel height measured using a profiler ( $H = 35\mu\text{m}$ ).**

A post exposure baking is performed for 10 minutes at 95<sup>0</sup>C followed by development step to remove residual photresist. For 7 minutes.



The 35  $\mu\text{m}$ -thick fluidic layer is positioned between a microscope slide and a control layer. The elastomeric membrane (100  $\mu\text{m}$  thickness) separating the control and fluidic layers is deflected down onto the fluidic layer by applying pressure to the control layer, thereby acting as a pneumatic valve, enabling flow rate control through the fluidic layer. Controlling relative flow rates through the outlet channels in the fluidic layer enables us to control the position of the stagnation point and to trap single microdroplets at the junction within the fluidic layer.

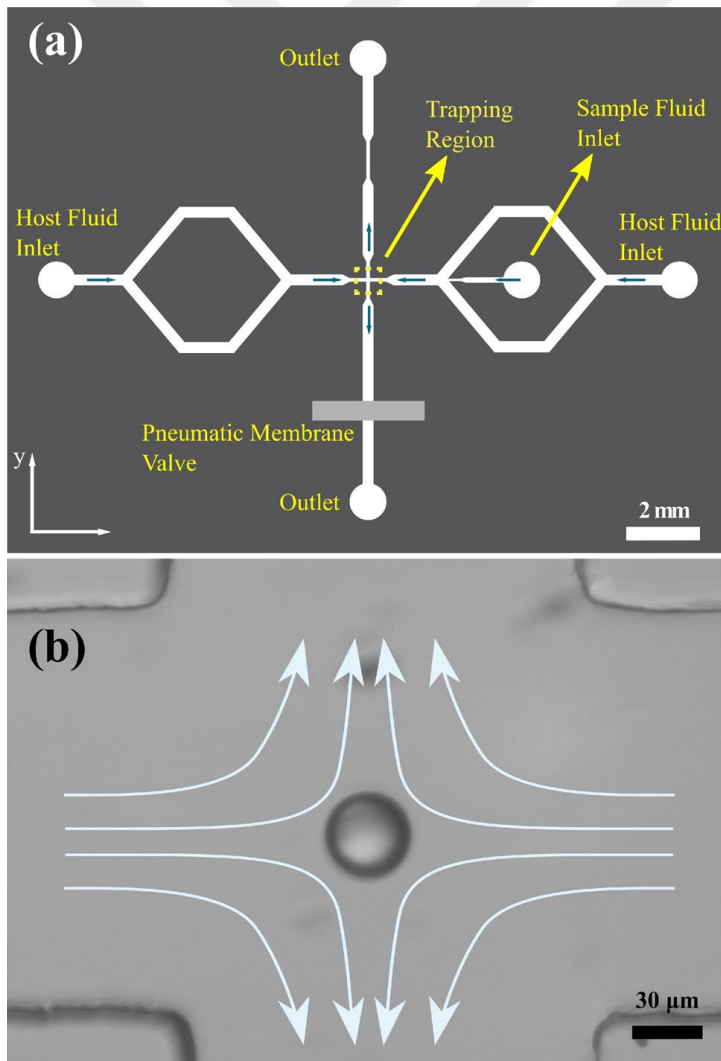


**Fig.7.4 (a) Microfluidic chip layout where inlets, outlets, pneumatic membrane valve and trapping region are indicated. (b) Image of a single microdroplet trapped at the junction of two intersecting microchannels using the hydrodynamic trap. Flow directions in the trapping region are indicated by arrows.**

Fig 7.4 (a) is a graphical representation of the final hydrodynamic trapping device with and (b) shows a droplet trapped at the stagnation point with stream lines represented by arrows.

### **7.3 Soft Lithography**

The microfluidic chips used as explained above were two layer (PDMS) devices. These two layers, called as fluidic and control layers, are prepared on different silicon molds. PDMS (Sylgard 184, Dow Corning) base to curing agent ratios of 15:1 and 5:1 were used for fluidic and control layers, respectively. After thoroughly mixing the curing agent with base and degassing for 20 min in a desiccator, the fluidic layer mixture was poured over a 3 inch silicon wafer used as the fluidic channel mold. The fluidic channels are designed to have around 35  $\mu\text{m}$  thickness and 150  $\mu\text{m}$  width. A twostep spin coating process 500 rpm for 90 seconds followed by 750 rpm for 30 seconds was applied, and an approximate fluidic layer thickness of 150  $\mu\text{m}$  was achieved. The control layer mixture was first degassed for 20 min in a desiccator and poured over another 3 inch silicon wafer patterned as control layer mold. These two wafers were baked for 40 min at 70  $^{\circ}\text{C}$ , and then the control layer was peeled off from the wafer. After a degassing access holes were punched, the PDMS block of the control layer was bonded to the fluidic layer using plasma bonding with a pneumatic pressure membrane carefully placed on the fluidic layer as shown Fig.10a. Thus,

the obtained two-layer PDMS block was left at room temperature for 10 min to improve the bonding. Liquid access holes were then punched in the resulting monolithic PDMS structure that was consecutively bonded to a microscope slide using plasma bonding. The final device was left overnight in an oven at 70°C to improve bonding.

#### 7.4 Microdroplet Generation

Two different droplet materials, n-decanol ( $C_{10}H_{22}O$  and CAS no.112-30-1, 99.0% pure) and benzyl benzoate (BB;  $C_{14}H_{12}O_2$  and CAS no.120-51-4,  $\geq 99.0\%$  pure), with very small solubilities in water were chosen. Table 7.1 summarizes relevant material constants of the droplet liquids used in the experiments. All constants are valid at room temperature, at which experiments were performed. To improve microdroplet stability and prevent microdroplets from sticking on microchannel surfaces, AOT surfactant (Docusate Sodium Salt,  $C_{20}H_{37}NaO_7S$  and CAS No: 577-11-7,  $\geq 99.0\%$  pure) was used.

In our experiments we used deionized (DI) water with 10  $\mu M$  or 10 mM AOT surfactant concentrations as the host fluid. Dynamic viscosity of the host fluid was assumed to be that of water,  $\mu_s = 0.89$  cP at  $\sim 25^\circ C$ . Both of the host fluids were used in the experiments with BB microdroplets while experiments with n-decanol microdroplets only employed DI water with 10 mM AOT surfactant as the host fluid. To generate microdroplets, a small amount of microdroplet liquid was added into a glass vial filled with the host liquid. Microdroplets were obtained by subsequent vigorous shaking. After waiting for a short while for the big microdroplets to settle at the bottom of the vial, the solution was loaded

into a syringe from the middle of the vial. This sample fluid was subsequently injected into the microfluidic chip using a syringe pump.

Droplet Liquid	D	C <sub>s</sub>	ρ	μ <sub>d</sub>
	m <sup>2</sup> /s	Kg/m <sup>3</sup>	Kg/m <sup>3</sup>	cP
n-Decanol	0.568 × 10 <sup>-9</sup>	37 × 10 <sup>-3</sup>	0.829	10.9
Bezyl Benzoate	0.539 × 10 <sup>-9</sup>	15 × 10 <sup>-3</sup>	1.112	8.292

**Table 7.1. Droplet Liquid Material Constants**

## 7.5 Experimental Setup

The experimental setup consisted of a microfluidic chip, a microscope (Nikon TE-2000 series), a camera (Point Grey Grasshopper3 U3 USB 3.0 CMOS camera), and a computer equipped with a data acquisition card (NI USB 6009), and a pressure regulator (Proportion-

Air DQPV1), a gas tank (Nitrogen), two syringe pumps (Harvard Peristaltic series), and a 4-way valve as shown in Fig.7.5. Host and sample fluids were injected into the microfluidic chip with syringe pumps. Sample fluid syringe pump contained one syringe whose outlet was connected to the sample fluid inlet of the microfluidic chip.

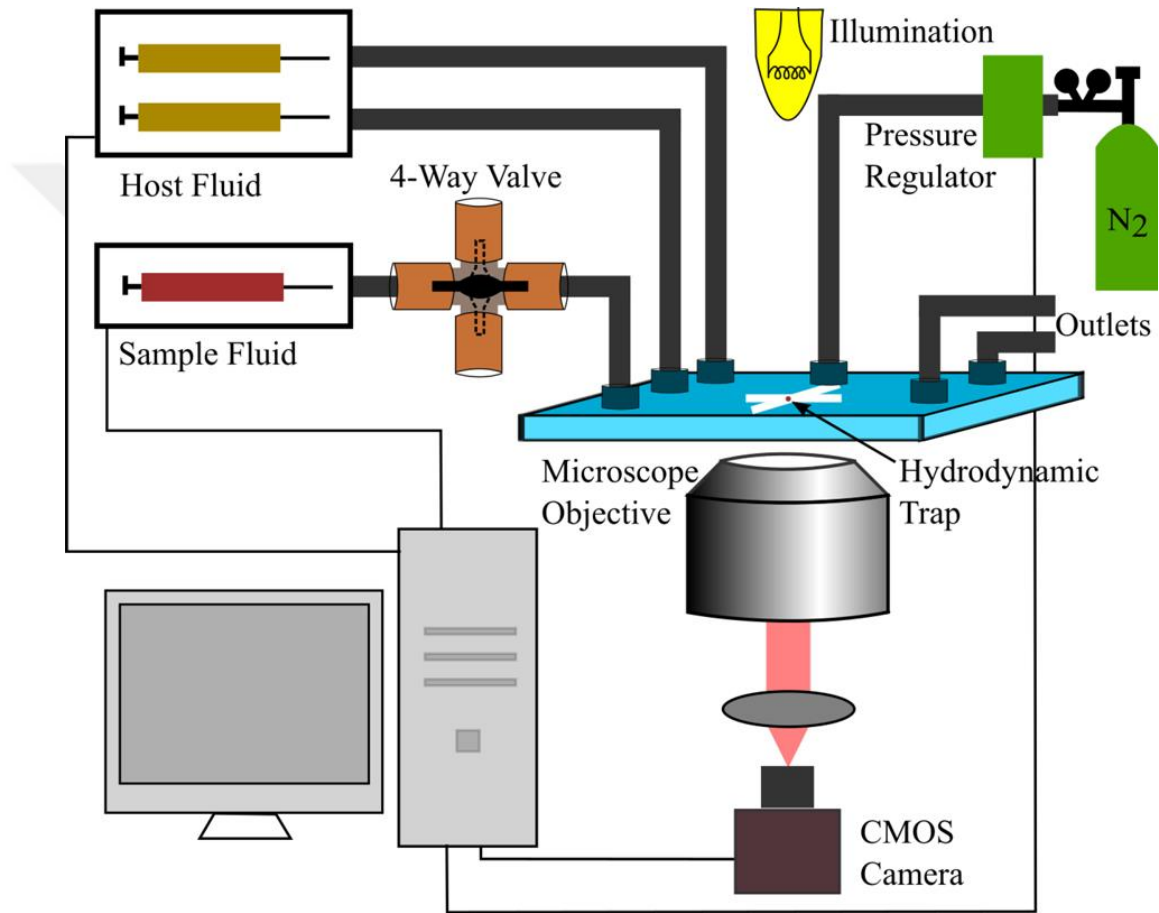


**Figure.7.5 Sketch of the experimental setup used for microdroplet hydrodynamic trapping experiments.**

In contrast, host fluid syringe pump contained two syringes whose outlets are connected to two separate host fluid inlets of the microfluidic chip. A custom developed computer program was used to detect microdroplets and find their positions in the trapping region using an image processing algorithm. The program selected and trapped the microdroplet that was nearest to the stagnation point. The position of the stagnation point is preset in the program. Once a microdroplet was selected, a feedback loop is activated by controlling the pressure regulator in order to keep the microdroplet trapped at the stagnation point. During the experiments, first, host and sample fluids were injected together into the microfluidic chip in order to make sure that microdroplets were available within the trapping region. Once a microdroplet was trapped, sample fluid flow was turned off using the 4-way valve. This ensured that fluid flow rates coming from left and right inlets were identical during the experiments. A series of snapshots was then recorded with the camera at predetermined time intervals. A microdroplet size at each snapshot was determined by post processing the recorded images.

## CHAPTER 8.

### Enhanced Dissolution of Liquid Micro Droplets

#### 8.1 Introduction

In this chapter we will discuss the results and outcomes of the enhanced dissolution experiments. As discussed above the experiments were divided into two parts by choosing two different surfactant concentration for both Benzyl benzoate and n-decanol experiments. We observed dissolution of BB and n-decanol microdroplets into an aqueous solution at various flow rates. BB and n-decanol are reported to be insoluble in water in many references in the literature, and there is very limited information about their saturation concentrations in water. Saturation concentrations of BB and n-decanol in water are reported to be  $15 \times 10^{-3} \text{ kg/m}^3$  and around  $37 \times 10^{-3} \text{ kg/m}^3$ , respectively. In our experiments, the aqueous solution was chosen as DI water with AOT surfactant dissolved at  $10 \text{ }\mu\text{M}$  or  $10 \text{ mM}$  concentrations. The results of the microdroplet dissolution experiments together with predictions from EP and ZYM models will be discussed in this chapter.

The experiments were conducted at different volumetric flow rates. Flow rates reported in these experiments correspond to the infusion rates from the host fluid syringe pump. Since two separate syringes are connected to this syringe pump, these infusion rates correspond to flow rates at each inlet channel. They are converted to free stream velocity  $U$  using  $U = Q/A_{\text{chan}}$  where  $Q$  is the flow rate and  $A_{\text{chan}}$  is the cross-sectional area of the fluidic channel that is assumed to be  $A_{\text{chan}} = 35 \times 150 \text{ }\mu\text{m}^2$ .

## 8.2 Benzyl Benzoate 10mM Experiments

In this section we will discuss the BB dissolution experiments for surfactant concentration of 10mM in the host fluid. The microdroplet dissolution experiments were performed with BB microdroplets in DI water with 10 mM AOT surfactant concentration at three different flow rates,  $Q = 10 \mu\text{L/h}$ ,  $Q = 20 \mu\text{L/h}$ , and  $Q = 50 \mu\text{L/h}$ . For a certain flow rate, data recorded from each microdroplet was time-shifted such that the initial droplet size had a time stamp that was equal to the time another droplet attained during its dissolution when it had the same size as the initial size of the studied microdroplet. This way continuous-looking scatter plots were obtained. Continuous and smooth nature as shown in Fig 8.1 of the scatter plots confirmed the consistent dissolution properties of the microdroplets under examination. Data was recorded from a total number of 4, 5, and 5 microdroplets as shown in Fig 8.1 panels a, b, and c, respectively.

Pe and Sh values corresponding to these data points as well as other data points presented in Fig 8.1 are shown in Fig 8.2 (a) and (b). Solid and dashed lines in Figure 8.1a–c indicate predictions by the EP and ZYM models. Very good were obtained between data and ZYM model predictions if  $c_s$  is assumed as  $c_s = 45 \times 10^{-3} \text{ kg/m}^3$ , while keeping all other material constants the same as those provided in Table 7.1. It was observed that for each case, the EP model prediction is significantly different than the experimental results, showing the importance of convection-based dissolution in our experiments.



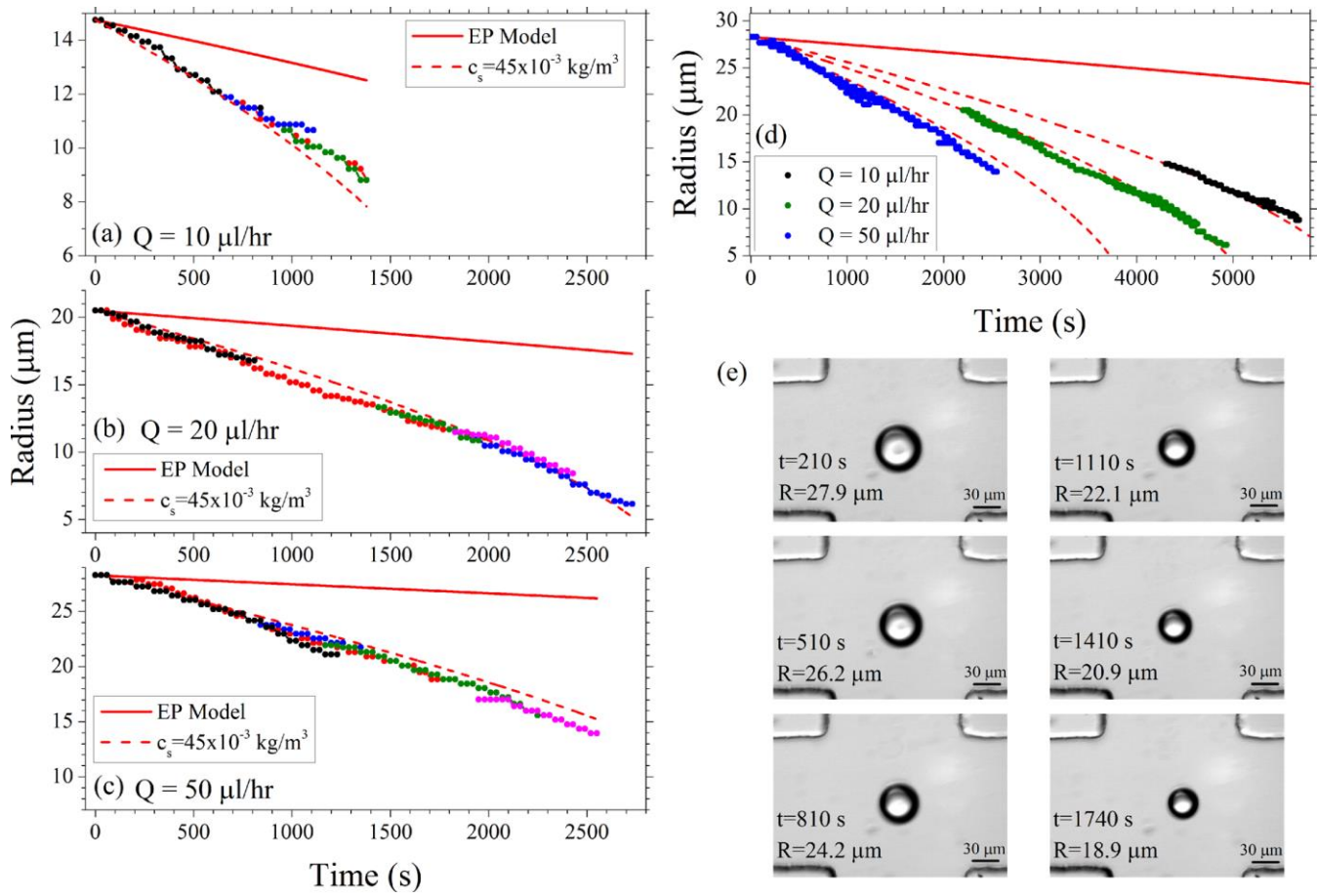


**Figure 8.1.** Scatter plots showing dissolution of multiple BB microdroplets in DI water containing 10 mM AOT surfactant at flow rates (a)  $Q = 10 \mu\text{L/h}$ , (b)  $Q = 20 \mu\text{L/h}$ , and (c)  $Q = 50 \mu\text{L/h}$  along with EP and ZYM model predictions. Measurements from 4, 5, and 5 microdroplets are time-shifted to obtain the scatter plots in panels a, b, and c, respectively. (d) Dissolution curves showing the combined scatter plots at three different flow rates along with EP and ZYM model predictions. In panels a–d, solid red lines show the EP model predictions and dashed red lines show the ZYM model predictions assuming  $c_s = 45 \times 10^{-3} \text{ kg/m}^3$ . (e) Snapshot images recorded from an exemplary BB microdroplet while dissolving at a flow rate of  $Q = 50 \mu\text{L/h}$ .

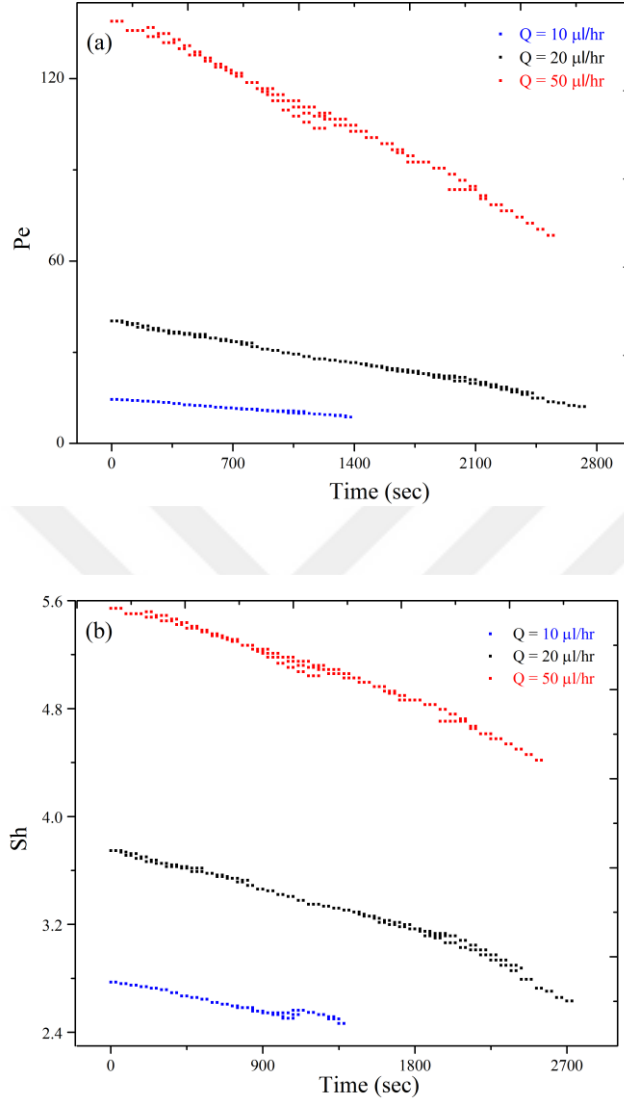


**Figure 8.2: Péclet (a) and Sherwood (b) numbers calculated for data points shown in Figure 3, obtained with benzyl benzoate microdroplets in DI water containing 10 mM AOT surfactant.**

The best fit value of  $c_s$  with the ZYM model,  $c_s = 45 \times 10^{-3} \text{ kg/m}^3$ , is larger than  $15 \times 10^{-3} \text{ kg/m}^3$  reported in the literature. We explain this difference by the enhancement in droplet dissolution rate due to micellar solubilization in the presence of surfactant at a concentration

higher than the CMC.<sup>81,82</sup> Micelles are formed when a surfactant is used above its CMC and the process of micelles incorporating solute molecules is called micellar solubilization. For AOT surfactant, CMC value is reported to be 5 mM in water at room temperature.<sup>87</sup>

It was observed that extensional creeping flow is expected to accumulate higher concentration of surfactant molecules at the top and bottom poles of the droplet. Such an inhomogeneous distribution of the surfactant molecules was not considered by the ZYM model, and can cause error in determination of the  $c_s$  value. The spherical shape of the droplets will be deformed for droplet sizes larger than the finite thickness (35  $\mu\text{m}$ ) of the fluidic channels. This may serve as another source of error in determination of the  $c_s$  value using the ZYM model.

In Figure 8.1d, data collected from different microdroplets is combined and represented by one color for each flow rate. Combined data set for each flow rate is then time-shifted to ensure a good overlap with the ZYM model predictions shown by dashed curves obtained assuming  $c_s = 45 \times 10^{-3} \text{ kg/m}^3$ , while keeping all other material constants the same as those provided in Table 7.1. This figure shows the enhancement in microdroplet dissolution with the flow rate. For instance at  $t = 3000 \text{ s}$ , droplet radius is observed to decrease by 31%, 39%, and 58%, for  $Q = 10 \text{ }\mu\text{L/h}$ ,  $Q = 20 \text{ }\mu\text{L/h}$ , and  $Q = 50 \text{ }\mu\text{L/h}$ , according to the ZYM model. In contrast, the EP model predicts a decrease in droplet radius by only 10% at  $t = 3000 \text{ s}$ .

### 8.3 Benzyl Benzoate 10 $\mu$ M Experiments

In order to study the effect of surfactant concentration on dissolution properties of liquid microdroplets a second experiment was designed with AOT surfactant concentration 10 $\mu$ m. The experiments were performed at three different flow rates ( $Q = 5 \mu\text{L/h}$ ,  $Q = 10 \mu\text{L/h}$  and  $Q = 15 \mu\text{L/h}$ ). Data collected from 5, 7, and 5 microdroplets are shown in Fig.8.3 (a), (b) and (c), respectively. Red dashed lines in Fig. 8.3 (a)-(c) indicate the predictions by the ZYM model assuming  $c_s = 15 \times 10^{-3} \text{ kg/m}^3$ , while keeping all other material constants the same as those provided in Table 7.1. Fig. 8.3 (d) shows the combined

Scatter plots at different flow rates along with the predictions by EP and ZYM models. Very good fits between the experimental data and the ZYM model predictions were obtained in Figure 8.3 a, c for  $Q = 5 \mu\text{L/h}$  and  $Q = 15 \mu\text{L/h}$ . For  $Q = 10 \mu\text{L/h}$ , a slight deviation is observed between the ZYM model prediction and the measurements if  $c_s = 15 \times 10^{-3} \text{ kg/m}^3$  is considered. We attribute this deviation mainly to variations in microfluidic chip fabrication that arise during the peeling off process from the molds. For this case, the ZYM model prediction assuming  $c_s = 18 \times 10^{-3} \text{ kg/m}^3$  shown with the dashed black line curve in Figure 8.3b, reveals the best fit with the measurements.

Hence, our experiments with BB microdroplets in DI water containing 10  $\mu\text{M}$  AOT surfactant reveal  $c_s = (15-18) \times 10^{-3} \text{ kg/m}^3$ . This range of  $c_s$  values is in agreement with the previous literature reporting  $c_s = 15 \times 10^{-3} \text{ kg/m}^3$  in the absence of surfactant.

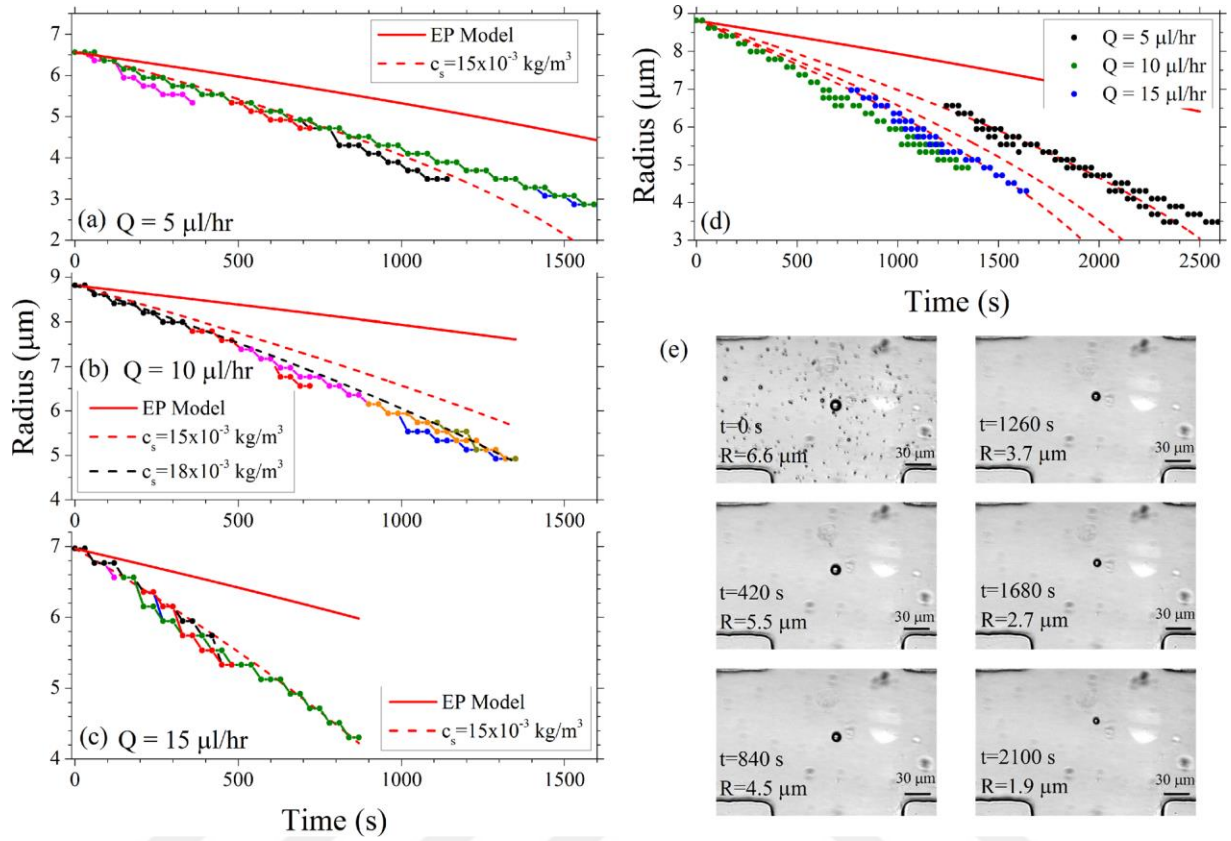


**Figure 8.3.** Scatter plots showing dissolution of multiple BB microdroplets in DI water containing  $10 \mu\text{M}$  AOT surfactant at flow rates (a)  $Q = 5 \mu\text{L/h}$ , (b)  $Q = 10 \mu\text{L/h}$ , and (c)  $Q = 15 \mu\text{L/h}$  along with EP and ZYM model predictions. Measurements from 5, 7, and 5 microdroplets are time-shifted to obtain the scatter plots in panels a, b, and c, respectively. (d) Dissolution curves showing the combined scatter plots at three different flow rates along with EP and ZYM model predictions. In panels a–d solid red lines show the EP model predictions and dashed red lines show the ZYM model predictions assuming  $c_s = 15 \times 10^{-3} \text{ kg/m}^3$ . Dashed black line in panel b shows the ZYM model prediction assuming  $c_s = 18 \times 10^{-3} \text{ kg/m}^3$ . (e) Snapshot images recorded from an exemplary BB microdroplet while at a flow rate of  $Q = 5 \mu\text{L/h}$ .

In addition, in this case, the AOT surfactant concentration of  $10\ \mu\text{M}$  is less than the CMC of  $5\ \text{mM}$  hence, the presence of AOT surfactant at  $10\ \mu\text{M}$  concentration is not expected to significantly change the droplet dissolution, and the observed  $c_s$  value remains around  $15 \times 10^{-3}\ \text{kg/m}^3$  which is identical to the case in which the host liquid does not contain any surfactant. The Sh and Pe number plots were also generated are shown in Fig 8.4 (a) and (b).

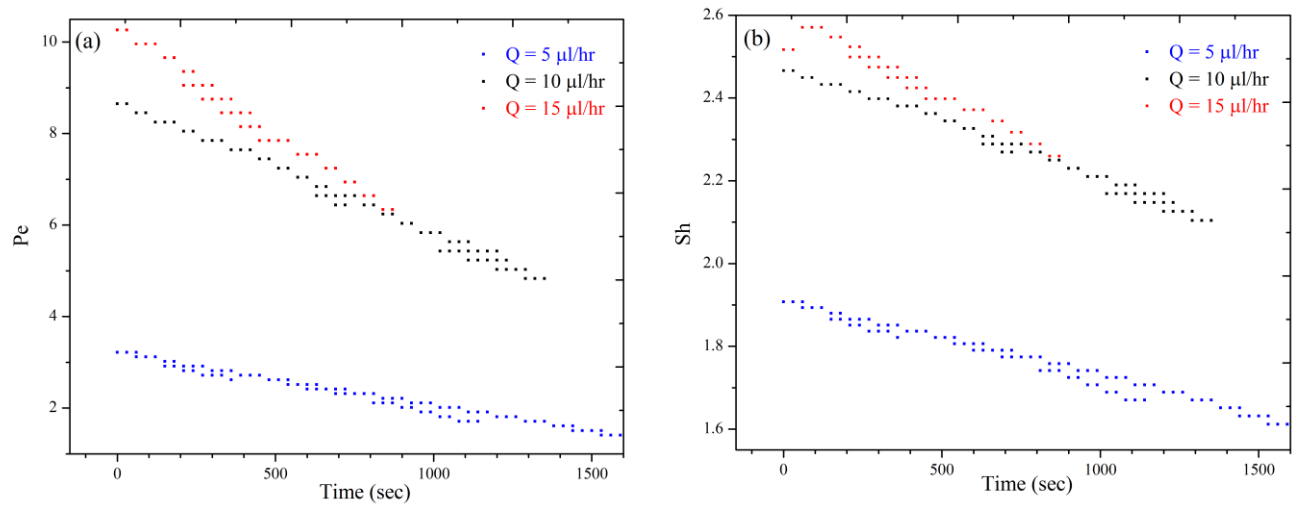


**Figure 8.4: Péclet (a) and Sherwood (b) numbers calculated for data points shown in Figure 8.3, obtained with benzyl benzoate microdroplets in DI water containing  $10\ \mu\text{M}$  AOT surfactant.**

## 8.4 Decanol 10 mM Experiments

In order to have an in depth understanding of dissolution of microdroplets another set of experiments was designed with n-Decanol. The AOT surfactant concentration was set to be 10mM. Three different flow rates ( $Q = 5 \mu\text{L/h}$ ,  $Q = 10 \mu\text{L/h}$ , and  $Q = 15 \mu\text{L/h}$ ) were employed. Results of these experiments are shown in Figure 8.5 along with the predictions by EP and ZYM models. Data collected from 5, 9 and 4 microdroplets are shown in different colors in Figure 8.5 panels a, b, and c, respectively. For all flow rates, good fits were obtained between the experimental data and ZYM model predictions if  $c_s$  was assumed as  $385 \times 10^{-3} \text{ kg/m}^3$ , while keeping all other material constants the same as those provided in Table 7.1. Combined scatter plots at each flow rate are plotted in Figure 8.5d along with the predictions by EP and ZYM models. Similar to the case of BB microdroplets in DI water containing 10 mM AOT surfactant (Figure 8.1), in this case, the best fitting  $c_s$  value is larger than  $37 \times 10^{-3} \text{ kg/m}^3$ ,<sup>88</sup> reported in the literature in the absence of surfactant. We explain the observed increase in the  $c_s$  value by the presence of the AOT surfactant at a concentration higher than the CMC of 5 mM. In the experiments shown in Figure 8.5, “halos” surrounding the microdroplet image were always observed. We attribute this to the accumulation of a gelled phase compound of surfactant molecules, micelles, and semi dilute microdroplets around the trapped microdroplet due to the high surfactant concentration. These halos morphed over time as the microdroplets dissolved. The ZYM model does not take into account the presence of such an additional layer on the microdroplet surface. Hence, the presence of the halo structure could explain the deviation of the dissolution curves from the ZYM model predictions for some microdroplets.

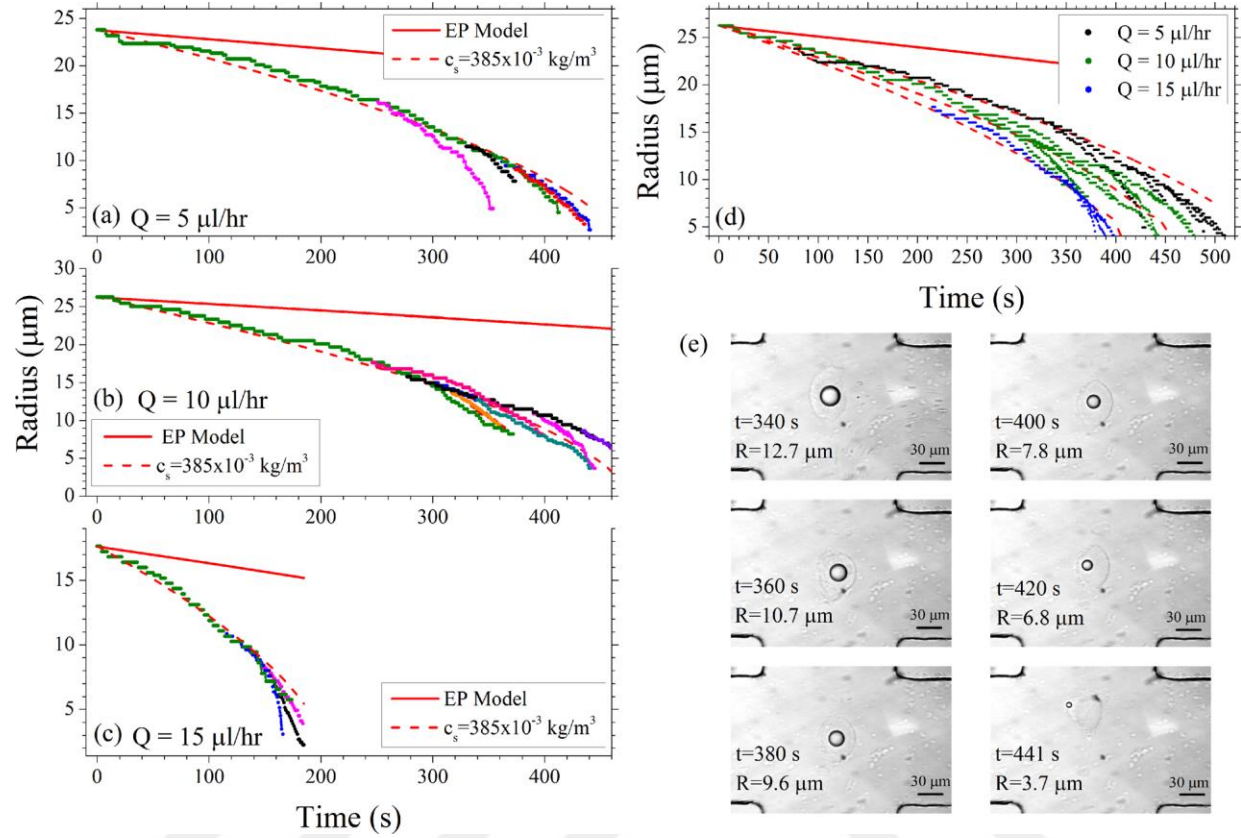


**Figure 8.5.** Scatter plots showing dissolution of multiple n-decanol microdroplets in DI water containing 10 mM AOT surfactant at flow rates (a)  $Q = 5 \mu\text{L/h}$ , (b)  $Q = 10 \mu\text{L/h}$ , and (c)  $Q = 15 \mu\text{L/h}$  along with EP and ZYM model predictions. Measurements from 5, 9, and 4 microdroplets are times shifted to obtain the scatter plots in panels a, b, and c, respectively. (d) Dissolution curve showing the combined scatter plots at three different flow rates along with EP and ZYM model predictions. In panels a–d solid red lines show the EP model predictions and dashed red lines show the ZYM model predictions assuming  $c_s = 385 \times 10^{-3} \text{ kg/m}^3$ . (e) Snapshot images recorded from an exemplary n-decanol microdroplet while dissolving at a flow rate of  $Q = 10 \mu\text{L/h}$ .



The Sh and Pe number plots for 10mM n-decanol experiments were also plotted and are shown Figure 8.6 (a) and (b).

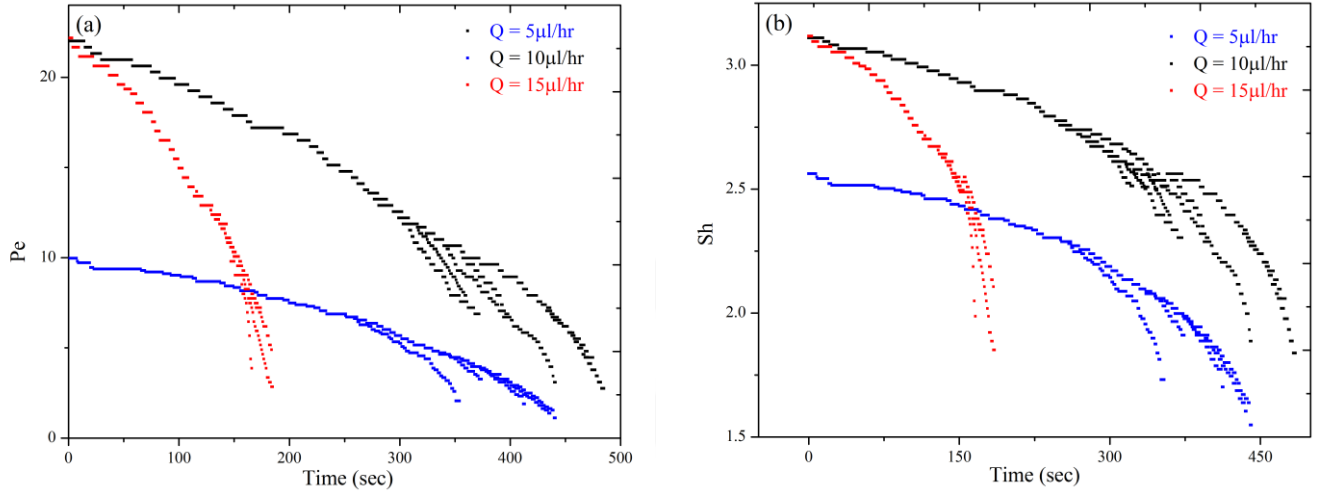


**Figure 8.6: Péclet (a) and Sherwood (b) numbers calculated for data points shown in Fig 8.5, obtained with n-decanol microdroplets in DI water containing 10 mM AOT surfactant.**

## 8.5 Experimental challenges and conclusion

From an experimental perspective, working at lower surfactant concentration proved to be difficult. In particular, working at lower surfactant concentrations limited the stability of microdroplet solution to tens of minutes compared to days at higher surfactant concentrations. Moreover, since droplets have a relatively long distance to travel before reaching the stagnation point, reduced surfactant concentrations increased the adhesion of droplets on channel surfaces. As a result, the dissolution of n-decanol microdroplets in host

liquid containing 10  $\mu\text{M}$  AOT surfactant could not be studied. Similarly, for the case of BB microdroplets, only relatively small microdroplet sizes ( $R < 9 \mu\text{m}$ ) could be studied with 10  $\mu\text{M}$  surfactant concentration in the host fluid.

The demonstrated method has great potential for fundamental studies in modeling droplet dissolution and for industrial applications such as separation processes, food dispersion, and drug development/design. In our experiments, the main limitations on the validity of the ZYM model are posed by the inhomogeneous surfactant distribution on the droplet surface, and droplet deformation perpendicular to the flow direction caused by the finite thickness of the fluidic channels. For the cases studied, no significant droplet deformation was induced along the flow directions by the extensional creeping flow.

## **CHAPTER 9.**

### **Conclusion and Outlook**

In this thesis, the first part focuses on viscosity measurements using a microfluidic device containing PDMS micropillars and the second part is focused on dissolution of hydrodynamically trapped liquid microdroplets. In chapter 1. A general introduction of microfluidic scaling laws and governing equations in reference to dimensionless numbers is presented. In chapter 2 the design and fabrication parameters of the microfluidic viscometer device are discussed with special focus on how the aspect ratio affects the response and sensitivity of the device. In chapter 3 the viscometry experiments for measuring viscosity of Newtonian and non-Newtonian fluids are explained and the non-linearity of the results for viscosity values above 25cP is discussed. Chapter 4 gives an insight into coagulation studies using micropillar based viscometer. CFD simulations and their comparison with the experimental results comprises the chapter 5. Chapter 6 engulfs the liquid microdroplet dissolution and its review as fundamental problem in liquid transport studies. Chapter 7 and 8 discuss the hydrodynamic chip fabrication and liquid dissolution results respectively.

## APPENDIX A

### MATLAB CODE FOR MICROPILLAR TRACKING

```
deoFileReader = vision.VideoFileReader(FileName);

videoPlayer = vision.VideoPlayer('Position', [100, 100, 680, 520]);

objectFrame = step(videoFileReader);

figure; imshow(objectFrame);

if exist('objectRegion')==0
    objectRegion=round(getPosition(imrect));
end

objectImage = insertShape(objectFrame, 'Rectangle', objectRegion,'Color', 'red');
figure; imshow(objectImage); title('Red box shows object region');

points = detectHarrisFeatures(rgb2gray(objectFrame), 'ROI', objectRegion);

pointImage = insertMarker(objectFrame, points.Location, '+','Color', 'white');

figure, imshow(pointImage), title('Detected interest points');

tracker = vision.PointTracker('MaxBidirectionalError', 1);

initialize(tracker, points.Location, objectFrame);

k=1;

while ~isDone(videoFileReader)

    frame = step(videoFileReader);

    [points,validity] = step(tracker, frame);

    coor(k) = struct('points', points , 'validity',validity);

    out = insertMarker(frame, points(validity, :), '+');

    step(videoPlayer, out);
```

```

        k=k+1;

end

release(videoPlayer);

release(videoFileReader);

hesap(coor,name,pathstr);

end

function disp=hesap(coor,figure_name,path_name)
for k = 1:length(coor)
    for y=1:length(coor(k).points)

        if coor(k).validity(y)==1

            if coor(k).points(y,1)>=coor(1).points(y,1)

                pixeldistance(k,y)=sqrt((coor(k).points(y,1)-coor(1).points(y,1))^2 +
(coor(k).points(y,2)-coor(1).points(y,2))^2);

            else

                pixeldistance(k,y)=-sqrt((coor(k).points(y,1)-coor(1).points(y,1))^2 +
(coor(k).points(y,2)-coor(1).points(y,2))^2);

            end

        end

    end

end

end

f=size(pixeldistance);

for l=1:f(1)

```

```

if l==1
    disp(l)=0;
else
    a=pixeldistance(l,:);
    disp(l)=mean(a(a~=0))*(0.819672);
end
end

h(1)=figure;
[Peak, PeakIdx] = max(disp);
time=1:length(disp);
stem(time,disp);
text(time(PeakIdx), Peak, sprintf('Peak = %.2f', Peak))

strValues = strtrim(cellstr(num2str([time(:) disp(:)],'%.2f,%.2f')));
text(time,disp,strValues,'VerticalAlignment','bottom');

hold on;

plot(time,disp)

baseFileName1 = sprintf('%s.xls',figure_name);% {length(figure_name)-1});
fullFileName1 = fullfile(path_name, baseFileName1);

col_header={'Displacement'};

row_header={'Frame'};

xlswrite(fullFileName1,disp,'Sheet1','B2');

xlswrite(fullFileName1,time,'Sheet1','A2');

xlswrite(fullFileName1,col_header,'Sheet1','B1');

```

```

xlswrite(fullFileName1,row_header,'Sheet1','A1');

baseFileName = sprintf('%s.fig',figure_name);%{length(figure_name)-1});

fullFileName = fullfile(path_name, baseFileName);

saveas(h(1),fullFileName);

end

function my_gui()

S.fh = figure('units','pixels',...

    'position',[0 0 1300 700],...

    'menubar','none',...

    'name','Project 1003',...

    'numbertitle','off',...

    'resize','off');

S.ed = uicontrol('style','edit',...

    'units','pix',...

    'position',[20 650 280 30],...

    'string','Enter Video PathName/FileName');

S.pb = uicontrol('style','pushbutton',...

    'units','pix',...

    'position',[350 650 180 30],...

    'string','Select Video',...

    'callback',{ @pb_call});

S.pb1 = uicontrol('style','pushbutton',...

    'units','pix',...

```

```

'position',[550 650 240 30],...

'string','Process Video-Glycerol-Harris-Solo-File',...

'callback',{ @pb_call2});

```

```

uicontrol(S.ed) % Make the editbox active.

```

```

uiwait(S.fh) % Prevent all other processes from starting until closed.

```

```

function [] = pb_call(varargin)

% Callback for the pushbutton.

[FileName,PathName] = uigetfile({'*.avi'},'Select video');

set(S.ed,'string',[PathName,FileName]);

end

function [] = pb_call2(varargin)

% Callback for the pushbutton.

filename=get(S.ed,'string');

[pathstr,name,ext] = fileparts(filename);

k=strsplit(name,'-');

Harris_Glycerol(filename,name,pathstr);

end

end

```



## REFERENCES

1. Eric, M. *Droplet- and Bead-Based Microfluidic Technologies for Rheological and Biochemical Analysis*. (2013).
2. Berthier, J. *Digital Microfluidics Micro-Drops and Digital Microfluidics Second Edition*.
3. Editor, S. & Potyrailo, R. A. *Integrated Analytical Systems*.
4. Reynolds Number & Pipe Flow. 4000
5. Gupta, S., Wang, W. S. & Vanapalli, S. A. Microfluidic viscometers for shear rheology of complex fluids and biofluids. *Cit. Biomicrofluidics* **10**, 43402 (2016).
6. Lee, J. & Tripathi, A. Intrinsic viscosity of polymers and biopolymers measured by microchip. *Anal. Chem.* **77**, 7137–7147 (2005).
7. Lindner, A. & Rousselet, A. Non-Newtonian Viscosity of Escherichia coli Suspensions. **268103**, 1–5 (2013).
8. Rodd, L. E., Scott, T. P., Boger, D. V, Cooper-white, J. J. & Mckinley, G. H. The inertio-elastic planar entry flow of low-viscosity elastic fluids in micro-fabricated geometries. **129**, 1–22 (2005).
9. Jibuti, L. & Peyla, P. Effective Viscosity of Microswimmer Suspensions. **098102**, 1–4 (2010).
10. Srivastava, N. & Burns, M. A. Analysis of non-Newtonian liquids using a microfluidic capillary viscometer. *Anal. Chem.* **78**, 1690–1696 (2006).
11. Kang, K., Lee, L. J. & Koelling, K. W. High shear microfluidics and its application in rheological measurement. **38**, 222–232 (2005).
12. Ranucci, M., Laddomada, T., Ranucci, M. & Baryshnikova, E. Blood viscosity during coagulation at different shear rates. *Physiol. Rep.* **2**, 1–7 (2014).

13. Fabrication, C. H. I. P. Deterministic trapping , encapsulation and retrieval of single cells. **7500**, 2–7 (2017).
14. Lieu, V. H., House, T. A. & Schwartz, D. T. Hydrodynamic Tweezers: Impact of Design Geometry on Flow and Microparticle Trapping. (2012).
15. Kobel, S., Valero, A., Latt, J. & Lutolf, M. Optimization of microfluidic single cell trapping for long-term on-chip culture †. 857–863 (2010). doi:10.1039/b918055a
16. Kumano, I., Hosoda, K., Suzuki, H. & Yomo, T. Lab on a Chip Hydrodynamic trapping of *Tetrahymena thermophila* for the long-term monitoring of cell behaviors { . 3451–3457 (2012). doi:10.1039/c2lc40367f
17. Banaeiyan, A. A., Ahmadpour, D. & Adiels, C. B. Hydrodynamic Cell Trapping for High Throughput Single-Cell Applications. 414–430 (2013). doi:10.3390/mi4040414
18. Espulgar, W. *et al.* Sensors and Actuators B : Chemical Single cell trapping and cell – cell interaction monitoring of cardiomyocytes in a designed microfluidic chip. *Sensors Actuators B. Chem.* **207**, 43–50 (2015).
19. Zhou, Y. *et al.* Sensors and Actuators B : Chemical A microfluidic platform for trapping , releasing and super-resolution imaging of single cells. *Sensors Actuators B. Chem.* **232**, 680–691 (2016).
20. Khalili, A. A., Ahmad, M. R., Takeuchi, M. & Nakajima, M. applied sciences A Microfluidic Device for Hydrodynamic Trapping and Manipulation Platform of a Single Biological Cell. 12–14 doi:10.3390/app6020040
21. Note, S. *Introduction to Optical Trapping*. (2012). doi:10.1007/978-3-642-29323-8
22. Manuscript, A. Optical trapping. **75**, 2787–2809 (2006).
23. Ampmann, R. K. & Inzinger, S. S. Optical tweezers for trapping in a microfluidic environment. **57**, 5733–5742 (2018).
24. Kotnala, A., Zheng, Y., Fu, J. & Cheng, W. Lab on a Chip. 2125–2134 (2017). doi:10.1039/c7lc00286f

25. Anand, S. Trapped Microdroplets Authors : Event Name : Optical Trapping Applications Year : Title : Whispering Gallery Modes Observed in Elastic Scattering from Optically Trapped Emulsion Microdroplets. (2017).
26. McGloin, D., Burnham, D. R., Summers, M. D., Rudd, D. & Anand, S. Optical manipulation of airborne particles : techniques and applications w. 335–350 (2008). doi:10.1039/b702153d
27. Magome, N., Kohira, M. I., Hayata, E., Mukai, S. & Yoshikawa, K. Optical Trapping of a Growing Water Droplet in Air. 3988–3990 (2003). doi:10.1021/jp034336h
28. Tanyeri, M., Johnson-chavarria, E. M. & Schroeder, C. M. Hydrodynamic trap for single particles and cells. 22–24 (2010). doi:10.1063/1.3431664
29. Tanyeri, M. & Schroeder, C. M. Manipulation and Con fi nement of Single Particles Using Fluid Flow. (2013). doi:10.1021/nl4008437
30. Tanyeri, M., Ranka, M. & Schroeder, C. M. Lab on a Chip PAPER A microfluidic-based hydrodynamic trap : design and implementation †. 1786–1794 (2011). doi:10.1039/c0lc00709a
31. Tanyeri, M., Ranka, M. & Schroeder, C. M. SUPPLEMENTARY MATERIAL A microfluidic-based hydrodynamic trap : Design and implementation †. 1–7 (2011).
32. Taparia, N., Ting, L. H., Smith, A. O. & Sniadecki, N. J. BENCH TOP OPTICAL DETECTION OF CLOT CONTRACTILITY FOR DIAGNOSTICS. 2241–2243 (2014).
33. Ting, L., Fegghi, S., Karchin, A., Tooley, W. & White, N. J. Clot-On-A-Chip: A Microfluidic Device To Study Platelet Aggregation and Contractility Under Shear. *Blood* **122**, 2363 LP-2363 (2013).
34. Sniadecki, N. J. & Chen, C. S. Microfabricated Silicone Elastomeric Post Arrays for Measuring Traction Forces of Adherent Cells. *Methods Cell Biol.* **83**, 313–328 (2007).
35. Beussman, K. M. *et al.* Micropost arrays for measuring stem cell-derived cardiomyocyte contractility. *Methods* **94**, 43–50 (2016).

36. Judith, R. M. *et al.* Micro-elastometry on whole blood clots using actuated surface-attached posts (ASAPs). *Lab Chip* **15**, 1385–1393 (2015).
37. Judith, R. M., Lanham, B., Falvo, M. R. & Superfine, R. Microfluidic viscometry using magnetically actuated micropost arrays. 1–17 (2018).
38. Kim, Y. Micropillar Arrays for High Sensitivity Sensors by. (2016).
39. Chandra, D. & Yang, S. H. U. Stability of High-Aspect-Ratio Micropillar Arrays against Adhesive and Capillary Forces. **43**, (2010).
40. Ishiyama, C., Shibata, A., Sone, M. & Higo, Y. Effects of Aspect Ratio of Photoresist Patterns on Adhesive Strength between Microsized SU-8 Columns and Silicon Substrate under Bend Loading Condition. **49**, 1–5 (2010).
41. Pipe, C. J., Kim, N. J. & Mckinley, G. H. Microfluidic rheometry on a chip.
42. Livak-dahl, E. & Burns, M. A. Lab on a Chip. 297–301 (2013). doi:10.1039/c2lc41130j
43. Jun Kang, Y., Ryu, J. & Lee, S. J. Label-free viscosity measurement of complex fluids using reversal flow switching manipulation in a microfluidic channel. *Biomicrofluidics* **7**, 19–21 (2013).
44. Kim, S., Kim, K. C. & Yeom, E. Microfluidic method for measuring viscosity using images from smartphone. *Opt. Lasers Eng.* **104**, 237–243 (2018).
45. Guillot, P. *et al.* Viscosimeter on a microfluidic chip. *Langmuir* **22**, 6438–6445 (2006).
46. Li, Y., Ward, K. R. & Burns, M. A. Viscosity Measurements Using Microfluidic Droplet Length. *Anal. Chem.* **89**, 3996–4006 (2017).
47. Delamarre, M. F., Keyzer, A. & Shippy, S. A. Development of a Simple Droplet-Based Microfluidic Capillary Viscometer for Low-Viscosity Newtonian Fluids. (2015). doi:10.1021/acs.analchem.5b00677
48. Bircher, B. A., Krenger, R. & Braun, T. Automated high-throughput viscosity and

- density sensor using nanomechanical resonators. *Sensors Actuators, B Chem.* **223**, 784–790 (2016).
49. Spatz, J. Wall shear stress imaging using micro-structured surfaces with flexible micro-pillars. 1–10
  50. Zou, M. *et al.* A novel polydimethylsiloxane microfluidic viscometer fabricated using microwire-molding. *Rev. Sci. Instrum.* **86**, (2015).
  51. Han, Z., Tang, X. & Zheng, B. A PDMS viscometer for microliter Newtonian fluid. (2016). doi:10.1088/0960-1317/17/9/011
  52. Pan, L. & Arratia, P. E. RESEARCH PAPER A high-shear , low Reynolds number microfluidic rheometer. 885–894 (2013). doi:10.1007/s10404-012-1124-2
  53. Li, W. J. L. S. W. & Luo, J. H. X. G. S. Rapid measurement of fluid viscosity using co-flowing in a co-axial microfluidic device. 687–693 (2010). doi:10.1007/s10404-009-0540-4
  54. Nguyen, N., Yap, Y. & Sumargo, A. Microfluidic rheometer based on hydrodynamic focusing. (2008). doi:10.1088/0957-0233/19/8/085405
  55. Hudson, S. D., Sarangapani, P., Pathak, J. A. I. A. & Migler, K. B. A Microliter Capillary Rheometer for Characterization of Protein Solutions. 678–685 (2015). doi:10.1002/jps.24201
  56. Lin, I. K. *et al.* Viscoelastic characterization and modeling of polymer transducers for biological applications. *J. Microelectromechanical Syst.* **18**, 1087–1099 (2009).
  57. Xiang, Y. & LaVan, D. A. Analysis of soft cantilevers as force transducers. *Appl. Phys. Lett.* **90**, 1–4 (2007).
  58. Lin, I. K. *et al.* Viscoelastic mechanical behavior of soft microcantilever-based force sensors. *Appl. Phys. Lett.* **93**, 1–4 (2008).
  59. White, C. C., Vanlandingham, M. R., Drzal, P. L., Chang, N. K. & Chang, S. H. Viscoelastic characterization of polymers using instrumented indentation. II. Dynamic testing. *J. Polym. Sci. Part B Polym. Phys.* **43**, 1812–1824 (2005).

60. Ethanol, M. Table S1 Properties of Pure Components : densities  $\rho$  ( g cm <sup>-3</sup> ), viscosities  $\eta$  ( mPa s ) and refractive indices  $n_D$  at 298 . 15 K  $\rho$ . 1–4
61. Cho, Y., Cho, D. J. & Rosenson, R. S. Endothelial Shear Stress and Blood Viscosity in Peripheral Arterial Disease Endothelial Shear Stress and Blood Viscosity in Peripheral Arterial Disease. (2014). doi:10.1007/s11883-014-0404-6
62. Cherry, E. M., Eaton, J. K., Cherry, E. M. & Eaton, J. K. Shear thinning effects on blood flow in straight and curved tubes Shear thinning effects on blood flow in straight. **073104**, (2016).
63. Mehri, R., Mavriplis, C. & Fenech, M. Red blood cell aggregates and their effect on non-Newtonian blood viscosity at low hematocrit in a two-fluid low shear rate microfluidic system. (2018).
64. Haas, T. *et al.* Comparison of thromboelastometry ( ROTEM w ) with standard plasmatic coagulation testing in paediatric surgery. *Br. J. Anaesth.* **108**, 36–41 (2012).
65. In, Z. & Blood, O. N. Computation Takes On Blood Behavior. **2139**, 5–7 (2012).
66. Diamond, S. L. New Microfluidic Paths to Test for Bleeding or Clotting. *Cell. Mol. Bioeng.* **10**, 1–2 (2017).
67. Desk, R. & Williams, L. Blood viscosity, fibrinogen, and activation of coagulation and leukocytes in peripheral arterial disease and the normal population in the Edinburgh Artery Study GD Lowe, FG Fowkes, J Dawes, PT Donnan, SE Lennie and E Housley *Circulation* 1993;87;1915-1920. *Circulation* (1993).
68. Srivastava, A., Fficm, F., Kelleher, A. & Bs, M. B. Point-of-care coagulation testing. **13**, 12–16 (2013).
69. Andreas, Klaus, Michael, M. *Rotem parameters*.
70. Dissertation VISCOELASTIC CHARACTERIZATION AND MODELING OF PDMS MICROPILLARS FOR CELLULAR FORCE MEASUREMENT APPLICATIONS by M . S ., Tsinghua University , China , 2006 Submitted in partial fulfillment of the requirements for the degree of Doctor of Philos. (2013).

71. Duncan, P. B. & Needham, D. Microdroplet Dissolution into a Second-Phase Solvent Using a Micropipet Technique : Test of the Epstein - Plesset Model for an Aniline - Water System. 4190–4197 (2006). doi:10.1021/la053314e
72. Li, H. & Gu, X. Correlation between drug dissolution and polymer hydration : A study using texture analysis. **342**, 18–25 (2007).
73. Kim, K. K. & Pack, D. W. Microspheres for Drug Delivery. (2006).
74. Epstien. No Title.
75. Duncan, P. B., Needham, D. & Carolina, N. Test of the Epstein - Plesset Model for Gas Microparticle Dissolution in Aqueous Media : Effect of Surface Tension and Gas Undersaturation in Solution. **15**, 2567–2578 (2004).
76. Rickard, D. L., Duncan, P. B. & Needham, D. Hydration Potential of Lysozyme : Protein Dehydration Using a Single Microparticle Technique. *Biophysj* **98**, 1075–1084 (2010).
77. Su, J. T. & Needham, D. Mass Transfer in the Dissolution of a Multicomponent Liquid Droplet in an Immiscible Liquid Environment. 13339–13345 (2013). doi:10.1021/la402533j
78. Shenoy, A., Tanyeri, M. & Schroeder, C. M. Characterizing the performance of the hydrodynamic trap using a control-based approach. (2014). doi:10.1007/s10404-014-1495-7
79. Kurdyumov, V. N. & Polyanin, A. D.  $\pm \text{sign} E(+ - 5 + 2 + t)$ . 137–141 (1991).
80. Zhang, J., Yang, C. & Mao, Z. Mass and Heat Transfer from or to a Single Sphere in Simple Extensional Creeping Flow. **58**, 20–25 (2012).
81. Introduction, A., Geoffrey, B. & Gentle, I. R. Interfacial Science. 2006 (2006). doi:10.1002/cphc.200500684
82. Rangel-yagui, C. O., Pessoa-jr, A. & Tavares, L. C. *Micellar solubilization of drugs* . **8**, (2005).

83. Polyanin, A. D., Polyanin, A. D. & Zaitsev, V. F. Mass and heat transfer between drops , bubbles and a flow. **2017**, (2018).
84. Batchelor, G. K. Mass transfer from a particle suspended in fluid with a steady linear ambient velocity distribution. **95**, 2–7 (2018).
85. Karimi, A., Yazdi, S. & Ardekani, A. M. Hydrodynamic mechanisms of cell and particle trapping in microfluidics. **021501**, 1–23 (2013).
86. Nilsson, J., Evander, M., Hammarström, B. & Laurell, T. *Analytica Chimica Acta* Review of cell and particle trapping in microfluidic systems. **649**, 141–157 (2009).
87. Remington, J. P.; Troy, D. B.; Beringer, P. R. *Remington An Introduction to Pharmacy*.
88. Union, I., Pure, O. F. & Chemistry, A. *Solubility data series*. **15**,